DEVELOPMENT OF DUAL PHASE MAGNESIA-ZIRCONIA CERAMICS FOR LIGHT WATER REACTOR INERT MATRIX FUEL

A Dissertation

by

PAVEL MEDVEDEV

Submitted to the Office of Graduate Studies of
Texas A&M University
in partial fulfillment of the requirements for the degree of

DOCTOR OF PHILOSOPHY

December 2004

Major Subject: Nuclear Engineering

DEVELOPMENT OF DUAL PHASE MAGNESIA-ZIRCONIA CERAMICS

FOR LIGHT WATER REACTOR INERT MATRIX FUEL

A Dissertation

by

PAVEL MEDVEDEV

Submitted to Texas A&M University
in partial fulfillment of the requirements
for the degree of

DOCTOR OF PHILOSOPHY

Approved as to style and content by:

Kenneth L. Peddicord (Chair of Committee)	
Yassin A. Hassan (Member)	Karl T. Hartwig (Member)
William H. Marlow (Member)	William E. Burchill (Head of Department)

December 2004

Major Subject: Nuclear Engineering

ABSTRACT

Development of Dual Phase Magnesia-Zirconia Ceramics

for Light Water Reactor Inert Matrix Fuel. (December 2004)

Pavel Medvedev, M.S., Idaho State University

Chair of Advisory Committee: Dr. Kenneth L. Peddicord

Dual phase magnesia-zirconia ceramics were developed, characterized, and evaluated as a potential matrix material for use in light water reactor inert matrix fuel intended for the disposition of plutonium and minor actinides. Ceramics were fabricated from the oxide mixture using conventional pressing and sintering techniques. Characterization of the final product was performed using optical microscopy, scanning electron microscopy, x-ray diffraction analysis, and energy-dispersive x-ray analysis. The final product was found to consist of two phases: cubic zirconia-based solid solution and cubic magnesia.

Evaluation of key feasibility issues was limited to investigation of long-term stability in hydrothermal conditions and assessment of the thermal conductivity. With respect to hydrothermal stability, it was determined that limited degradation of these ceramics at 300^{o}C occurred due to the hydration of the magnesia phase. Normalized mass loss rate, used as a quantitative indicator of degradation, was found to decrease exponentially with the zirconia content in the ceramics. The normalized mass loss rates measured in static 300^{o}C de-ionized water for the magnesia-zirconia ceramics containing 40, 50, 60, and 70 weight percent of zirconia are 0.00688, 0.00256, 0.000595, 0.000131

g/cm^2/hr respectively. Presence of boron in the water had a dramatic positive effect on the hydration resistance. At 300^{o}C the normalized mass loss rates for the composition containing 50 weight percent of zirconia was 0.00005667 g/cm2/hr in the 13000 ppm aqueous solution of the boric acid. With respect to thermal conductivity, the final product exhibits values of 5.5-9.5 W/(m deg) at 500^{o}C, and 4-6 W/(m deg) at 1200^{o}C depending on the composition. This claim is based on the assessment of thermal conductivity derived from thermal diffusivity measured by laser flash method in the temperature range from 200 to 1200^{o}C, measured density, and heat capacity calculated using rule of mixtures. Analytical estimates of the anticipated maximum temperature during normal reactor operation in a hypothetical inert matrix fuel rod based on the magnesia-zirconia ceramics yielded the values well below the melting temperature and well below current maximum temperatures authorized in light water reactors.

ACKNOWLEDGEMENTS

The author hereby acknowledges the Argonne National Laboratory (ANL) for hosting him as a guest graduate student in 2002-2004 and granting access to its facilities and staff resources. The funding for the guest graduate student appointment at ANL was provided by the Advanced Fuel Cycle Initiative of the United States Department of Energy. The author gratefully acknowledges these agencies.

Drs. Meyer and Hayes are acknowledged for their roles in instigation of this project, recruiting the author to carry it out, and their continuous guidance during this work. Drs. Frank, Lambregts, O'Holleran, and Mr. Maddison are acknowledged for operating the analytical instruments used for characterization and evaluation of the ceramics. Dr. Jue is gratefully acknowledged for helpful discussions on the subject of ceramic development and characterization. Sincere thanks to Mr. Knighton, Mr. DeGiuli, and Mr. Simpson for manufacturing and troubleshooting the ceramic fabrication and testing equipment, and to Mr. Hahn and Mr. Olsen for photography services.

The author expresses deepest gratitude to the Chair of the Advisory Committee, Dr. Peddicord, for continuous support throughout his studies at Texas A&M University.

TABLE OF CONTENTS

Page

LIST OF FIGURES

FIGURE Page

FIGURE Page

FIGURE Page

LIST OF TABLES

CHAPTER I

INTRODUCTION

1.1 DEFINITION OF THE INERT MATRIX FUEL

Inert Matrix Fuel (IMF) is a type of nuclear reactor fuel that consists of a neutron-transparent matrix and a fissile phase that is either dissolved in the matrix or incorporated as macroscopic inclusions. The matrix plays a crucial role of diluting the fissile phase to the volumetric concentrations required by reactor control considerations, the same role U-238 plays in conventional low enriched uranium (LEU) or mixed uranium-plutonium oxide (MOX) fuel. The key difference is that replacing U-238 with a neutron-transparent matrix eliminates plutonium breeding as a result of neutron capture.

IMF technology is believed to have a great potential to improve the efficiency of in-reactor disposal of plutonium, and provide opportunities for disposal of neptunium, americium and curium. The latter group of elements is also known as minor actinides. Estimates [1] have shown that if plutonium is used as a fissile phase, at least 90% of it will be destroyed. Therefore, IMF irradiation campaign intakes proliferation-prone nuclear material with very high radiotoxicity (half-life of several thousands of years) and yields a valuable commodity such as energy and short-lived radioactive waste that can be managed considerably more easily than the original stream of plutonium and actinides.

This dissertation follows the style and format of the Journal of Nuclear Materials.

No other technology is currently available to target at the same time the radiotoxicity and proliferation risks of the surplus nuclear material. The mixed oxide fuel path currently accepted for in-reactor plutonium disposition does make surplus plutonium unattractive for weapons. However the issue of nuclear waste from MOX irradiations remains unresolved. At the present time the IMF burning combined with nuclear waste transmutation are the industry's only prospects for a waste-free nuclear cycle.

Technical feasibility of the IMF technology relies heavily on material properties of the matrix. The matrix must meet the following criteria:

- high thermal conductivity,
- compatibility with reactor materials,
- high radiation resistance,
- low neutron absorption cross section,
- meet acceptance criteria for either direct disposal or reprocessing.

1.2 HISTORICAL PERSPECTIVE

The possibility to recycle plutonium using inert matrix fuels was first examined in the late fifties and early sixties. Freshley [2] provides a detailed overview of the fabrication and irradiation studies performed at that time. Several types of plutonium-containing fuels were investigated: alloys, refractory compounds, cermets and glasses. The feasibility of plutonium recycling was successfully demonstrated.

The escalation of the nuclear arms race in the second half of the twentieth century made plutonium recycling a lesser priority than plutonium generation. Furthermore, fast reactor programs rapidly maturing in USSR, USA, France and Japan were viewed as an efficient plutonium management tool. Therefore, the interest in new plutonium-bearing fuels was low.

The end of the last century marked the end of nuclear arms race. Coincidently, once flourishing fast reactor programs lost public and governmental support and were no longer viable for plutonium management. In addition, political fallout from Chernobyl disaster caused a general decline in the nuclear industry. Very few nuclear power plants were being built, and several nations declared intentions to become nuclear-free, thus diminishing the opportunities for in-reactor plutonium disposition. At the same time it was estimated that the world's inventory of plutonium, both military and reactor grade, may have reached 1700 tons in the year 2000 and was growing by approximately by 70 tons per year due to increasing stockpiles of spent nuclear fuel [3].

The possibility of burning MOX to dispose of weapons grade plutonium in existing reactors provided only limited comfort to former Cold War adversaries. In addition, the nuclear industry, ever unpopular among general public, realized that it would only survive if the issue of spent nuclear fuel is resolved. Recognition that IMF would burn plutonium more efficiently than MOX and simultaneously transmute nuclear waste sparked new interest in this technology.

Since the mid-nineties scientists and engineers in several European countries, USA, Russia and Japan began examining the possibility of use of IMF in existing water-

cooled reactors. The knowledge gained in the sixties was reevaluated in the light of current regulatory framework. Because notable progress has been made since the sixties in metallurgy, refractories, and materials behavior, the search for new matrices that can be spiked with plutonium and inserted in a reactor was resumed.

In the United States the Advanced Fuel Cycle Initiative (AFCI) was launched in 2003 to develop nuclear technologies for reducing long-term hazards of nuclear waste and generating a substantial amount of energy for the power grid. Recognizing that the United States economic well-being and national security would be strengthened by implementation of such technologies, the U.S. Congress authorized $66.7 million for the AFCI program in 2004 alone. Organizationally, research and development of IMF and targets for transmutation of nuclear waste is currently performed under the umbrella of the AFCI program.

1.3 CURRENT STATUS

An array of materials is being presently considered for the development of IMF by the reactor fuels community. Selection usually begins by evaluating the published literature to address issues outlined above. Then materials compatibility issues are investigated experimentally. After materials compatibility criteria are satisfied, lab-scale manufacturing efforts take place first using non-radioactive surrogates to simulate the Pu and actinides. Once the manufacture method is perfected, irradiation experiments follow. The experimental work is conducted in parallel with the neutronic, thermo-hydraulic and fuel performance modeling efforts with an ultimate goal being the

licensing a successful IMF candidate with a nuclear regulatory authority. The key to successful licensing is to demonstrate that the new fuel does not exceed the safety limits that exist for conventional LEU or MOX fuel.

None of the IMFs has yet been licensed for use in a commercial LWR. However, extensive experimental irradiation studies are underway or completed.

Table 1.1 provides a list of the recent large-scale international programs dealing with IMF irradiation in experimental reactors. Included in Table 1.1 are the following programs: Once Through Then Out (OTTO), Rock-like Oxide (ROX), Yttria Stabilized Zirconia (YSZ), Experimental Feasibility of Targets for Transmutation (EFTTRA), Thermal Behavior of Heterogeneous Fuel (THERMHET), Matrices for Incineration of Actinides (MATINA), and Accelerator Transmutation of Waste (ATW).

YSZ appears to be the most evolved IMF candidate for use in LWRs. Both steady-state [4] and transient [5] irradiations of YSZ-based IMF have been performed. Material properties of YSZ have been closely examined [6], [7]. Out-of pile irradiation studies designed to understand the mechanism of radiation damage have been completed [8]. Neutronic feasibility of YSZ-based IMF has been also assessed [9] complemented by core burnup calculations and accident analyses [10]. In fact, majority of the publications at the 8th Inert Matrix Fuel Workshop held in Tokai, Japan, 16 - 18 October 2002 were dedicated to YSZ-based IMF. Despite its excellent radiation resistance, compatibility with reactor materials and good neutronic properties, very low thermal conductivity is the main disadvantage of YSZ. According to recent analysis [9] fuel centerline temperature of the YSZ-based IMF may be 100^{o}C higher than the limit

specified for LWRs. Licensing of such fuel is unlikely. Safe use of YSZ as a matrix in LWR fuel is only possible if a reactor is operated at a lower power or if fuel pellets feature central voids. Both measures increase the cost and decrease the feasibility of plutonium disposition. Furthermore, even if licensed, YSZ-based IMF would not meet the reprocessing criteria since it was developed with a direct disposal concept in mind.

MgO and Mg_2AlO_4 have also attracted significant attention in studies listed in Table 1.1. However, inability of MgO to withstand attack by LWR coolant bars it from use in water-cooled environments. Mg_2AlO_4 exhibited poor radiation resistance with swelling in some cases as high as 27% [11].

1.4 RESEARCH NEEDS

Materials research, development and evaluation are currently a top priority in strengthening a case for burning plutonium and minor actinides using IMF. The research in the field is expected to continue until a product that meets general criteria outlined in section 1.1 is developed and licensed for use in LWR by a nuclear regulatory body.

Table 1.1. Recent large-scale international programs dealing with IMF irradiation.

Program	Reactor	Location	Inert matrix	Reference
OTTO	HFR	Petten, Netherlands	Y_2O_3-ZrO_2, $MgAl_2O_4$	Schram et al. [12]
ROX irradiation	JRR-3	Tokai, Japan	Y_2O_3-ZrO_2, $MgAl_2O_4$, Al_2O_3	Nitani et al. [13]
YSZ irradiation	MTR	Halden, Norway	Y_2O_3-ZrO_2	Hellwig et al. [4]
EFTTRA T3	HFR	Petten, Netherlands	MgO, $MgAl_2O_4$, Y_2O_3, $Y_3Al_5O_{12}$, CeO_2	Neeft et al. [14]
EFTTRA T4	HFR	Petten, Netherlands	$MgAl_2O_4$	Wiss et al. [15]
THERMHET	SILOE	Grenoble, France	$MgAl_2O_4$	Noirot et al. [16]
ECRIX, CAMIX–COCHIX	PHENIX	Marcoule, France	MgO, Y_2O_3-ZrO_2	Croixmarie et al. [17]
MATINA	PHENIX	Marcoule, France	MgO, $MgAl_2O_4$	Chauvin et al. [18]
ATW	ATR	Idaho Falls,USA	Zr, ZrN	Hayes et al. [19]

1.5 OBJECTIVES AND SCOPE OF WORK

The present study is supported by the DOE's AFCI program and is contracted by Nuclear Technology Division of Argonne National Laboratory (ANL). Inspired by positive results obtained during recent irradiations of MgO-based fuels [14, 17, 18] ANL decided to further investigate the possibility of use of this material in light water reactors. ANL has requested the author to perform a review of MgO material properties relevant to LWR fuel safety. Recognizing that inability of MgO to withstand hydration attack by LWR coolant is the factor limiting use of MgO in LWR, the experimental part of this work is dedicated to development, characterization and assessment of an MgO-based material compatible with LWR coolant.

CHAPTER II

MAGNESIUM OXIDE AS A CANDIDATE INERT MATRIX FOR USE IN LWR FUELS: REVIEW OF MATERIAL PROPERTIES AND IRRADIATION EXPERIENCE

This chapter provides a review of MgO material properties as a potential LWR IMF matrix. Section 2.1 contains general information on MgO including the crystal structure, chemical reactions, manufacture and common uses of MgO ceramics. Section 2.2 gives an insight on thermal and mechanical properties, with Section 2.3 discussing the latter after neutron irradiation. Effects of fission fragment irradiation are discussed in Section 2.4. The issues of compatibility of MgO with reactor materials are addressed in Section 2.5. Section 2.6 outlines the prior and on-going efforts to utilize MgO in water reactors. Summary and recommendations are included in Section 2.7.

2.1 GENERAL INFORMATION

2.1.1 Crystal structure

Magnesium oxide is an ionic crystal, and can be viewed as an arrangement of hard spheres bound together by electrostatic forces. In an MgO unit cell 14 oxygen ions are close-packed into a face-centered cubic structure, while 12 magnesium ions are located at the center of the cube edges and 1 magnesium ion located at the cube center as shown in Figure 2.1. This structure can be considered as consisting of two

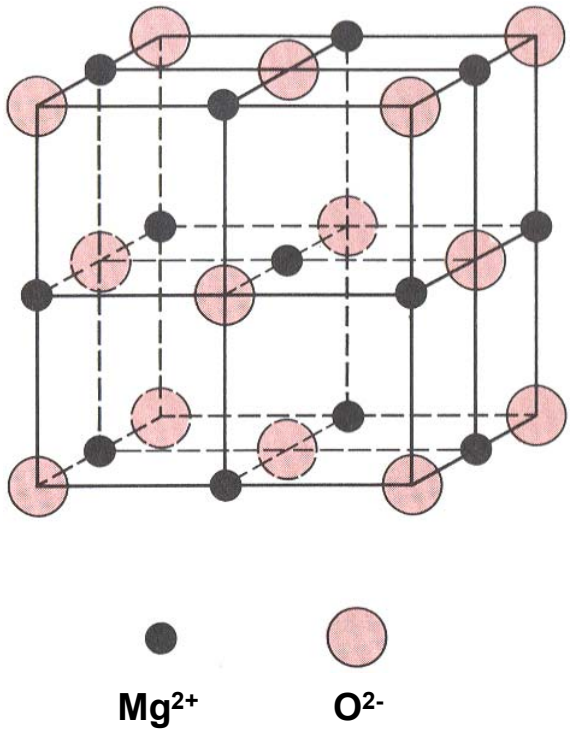

Figure 2.1. A unit cell for MgO crystal structure. Reprinted from the Materials Science and Engineering: an Introduction, William D. Callister, Copyright © (1991, John Wiley and Sons), p. 397, with permission of John Wiley and Sons, Inc.

interpenetrating FCC lattices, one of Mg^{2+} ions and on of O^{2-} ions. This type of crystal structure is called "rock salt structure" and is formed by ceramic materials with an equal numbers of cations and anions such as NaCl, MnS, LiF, and FeO.

Crystals of the rock salt structure deform by slip most easily on {110} planes. At high temperatures slip occurs on {100} planes. It should be noted the slip on {110} planes is more favorable than on {100}, although the {100} planes are the more densely packed. The reason that the {100} planes are not the primary glide planes is due to the strong repulsive forces arising between cations being moved closer to each other when the glide on {100} planes occurs. Further details of mechanical behavior of single-crystal and polycrystalline MgO are provided in Langdon and Pask [20].

MgO occurs in nature as a rare mineral periclase, which can be found as groups of crystals in marble. Single-crystal and non-porous polycrystalline MgO is transparent, and porous MgO has a white color.

The density of MgO is 3.58 g/cm^3 and the melting temperature is 2827 ± 30°C.

2.1.2 Chemical reactions

MgO is a typical alkali-earth metal oxide. It reacts even with weak acids forming salts, and reacts with water forming magnesium hydroxide $Mg(OH)_2$. The aqueous solubility of MgO in water is 0.00062 g /100ml at 20^{o}C [21], and solubility product of $Mg(OH)_2$ is 5.61 x 10^{-11} at 25^{o}C.

MgO is available in several grades: pure-fused, dead-burned, hard-burned, and light burned. The difference between the grades is in the calcination time and

temperature. The production conditions and resultant magnesia properties are presented in Table 2.1 [21].

Light-burned magnesia reacts with dilute acids, hydrates upon exposure to moisture or water. Hard-burned magnesia has low chemical reactivity, and is soluble in concentrated acids. Dead-burned magnesia reacts very slowly with strong acids, and does not hydrate readily. Out of four grades, fused magnesia exhibits superior chemical stability, strength and abrasion resistance.

2.1.3 Common uses

Dead burned magnesia is used extensively for refractory applications in the form of granular refractories and brick. Refractory crucibles made out of pure MgO are highly resistant to molten metal and slag. Refractory grade MgO is used extensively in steel production to serve as both protective and replaceable linings for equipment used to handle molten steel, according to Martin Marietta Magnesia Specialties. Volatility above 1500^{o}C in reducing atmospheres or vacuum, and low thermal shock resistance are the disadvantages that limit industrial use of MgO ceramics according to Boles [22].

Due to high chemical reactivity, the hard-burned and light-burned magnesia are not used as structural materials, but they are used in large amounts as raw materials in a number of chemical processes.

Table 2.1. Production conditions and resultant magnesia properties. Reprinted from the Encyclopedia of Chemical Technology, 4th edition, Vol. 15, R.E. Kirk, D.F. Othmer, J.I. Kroschwitz, M. Howe-Grant, Copyright © (1995, John Wiley and Sons), p. 704, with permission of John Wiley and Sons, Inc.

Magnesia grade	Calcination temperature, ^{o}C	Surface area, m^2/g	Crystallite size, μm	Porosity, %
Light-burned	<950	1-200	<0.5	70-80
Hard-burned	1090-1650	0.1-1	1-20	40-50
Dead-burned	>1800	<0.1	>40	0-5
Pure-fused	>2750		single crystal	

2.2 THERMAL AND MECHANICAL PROPERTIES

2.2.1 Heat capacity

The heat capacity of MgO increases slightly with temperature as shown in Figure 2.2**.** Figure 2.2 shows that the heat capacity of MgO is greater than that of UO_2. The MgO heat capacity data experimental data used in Figure 2.2 are from Victor and Douglas [23], Miyayama [24], Schlesinger [25], and Kirk et al. [21]. The UO_2 heat capacity data is from the work of Popov et al. [26]

Greater heat capacity of the fuel is beneficial for the fuel performance, particularly during Reactivity Initiated Accidents (RIA). At the same amount of energy deposited per unit mass of fuel during such an accident, the fuel with a greater heat capacity would operate at a lower temperature than the fuel with a lower heat capacity.

2.2.2 Thermal conductivity

Published [27, 28, 29, 30] values of MgO thermal conductivity as a function of temperature are presented in Figure 2.3. The data by Chavrat and Kingery [28] reflects the thermal conductivity of one single crystal sample and two polycrystalline samples with the grain size of 8μm and 12μm. As shown in Figure 2.3, the single crystal sample has the highest thermal conductivity, followed by the sample with 8μm grains, with the 12μm – grained sample having the lowest thermal conductivity. According to Chavrat and Kingery, this trend is due to the effect of impurities found in analyzed samples, and

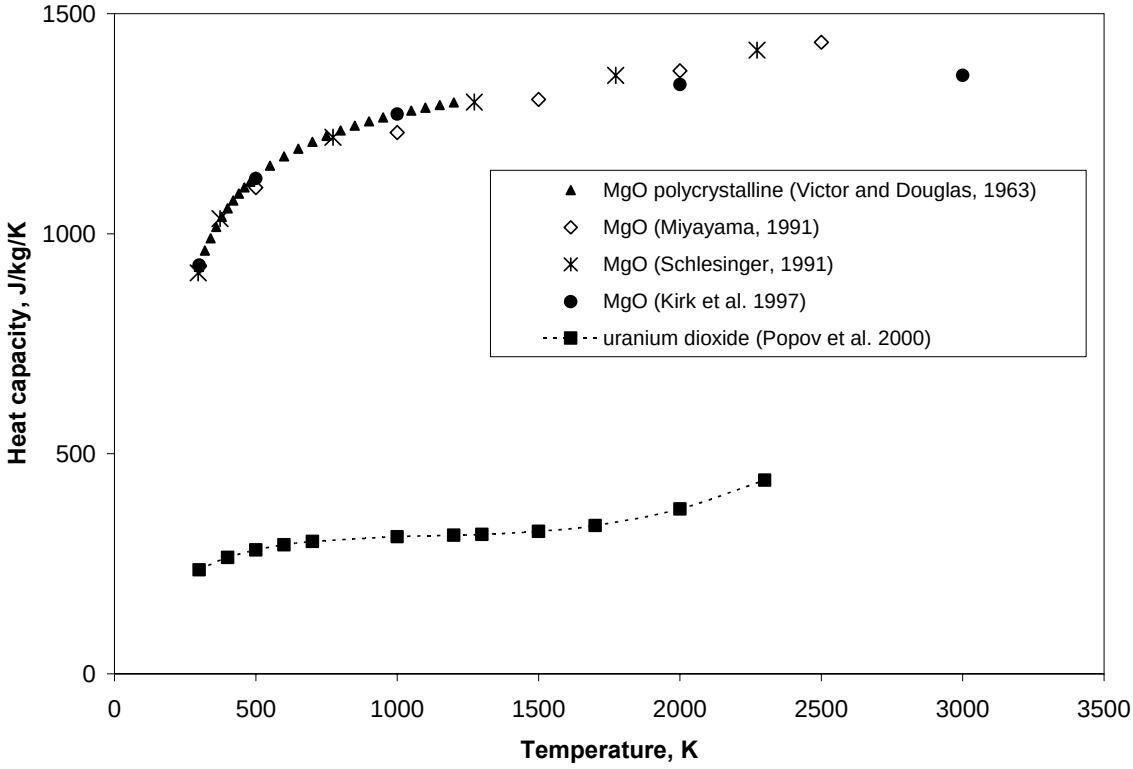

Figure 2.2. Heat capacity of MgO shown in comparison with that of UO_2.

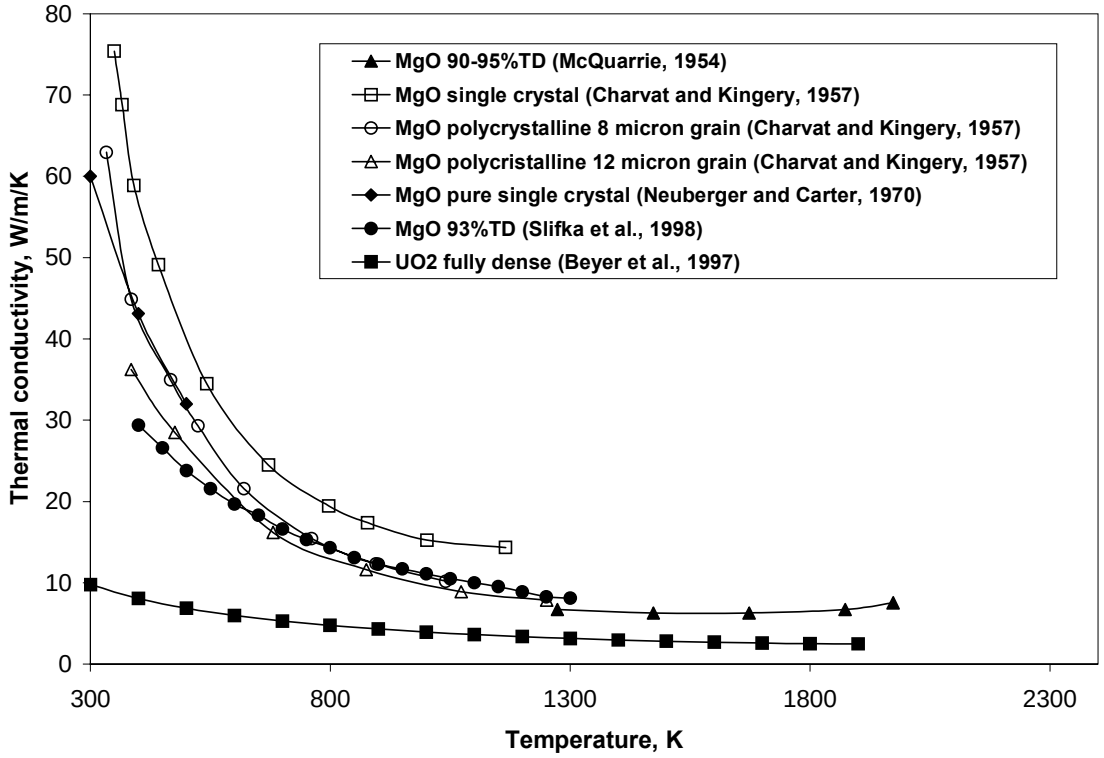

Figure 2.3. Thermal conductivity of MgO shown in comparison with that of UO_2.

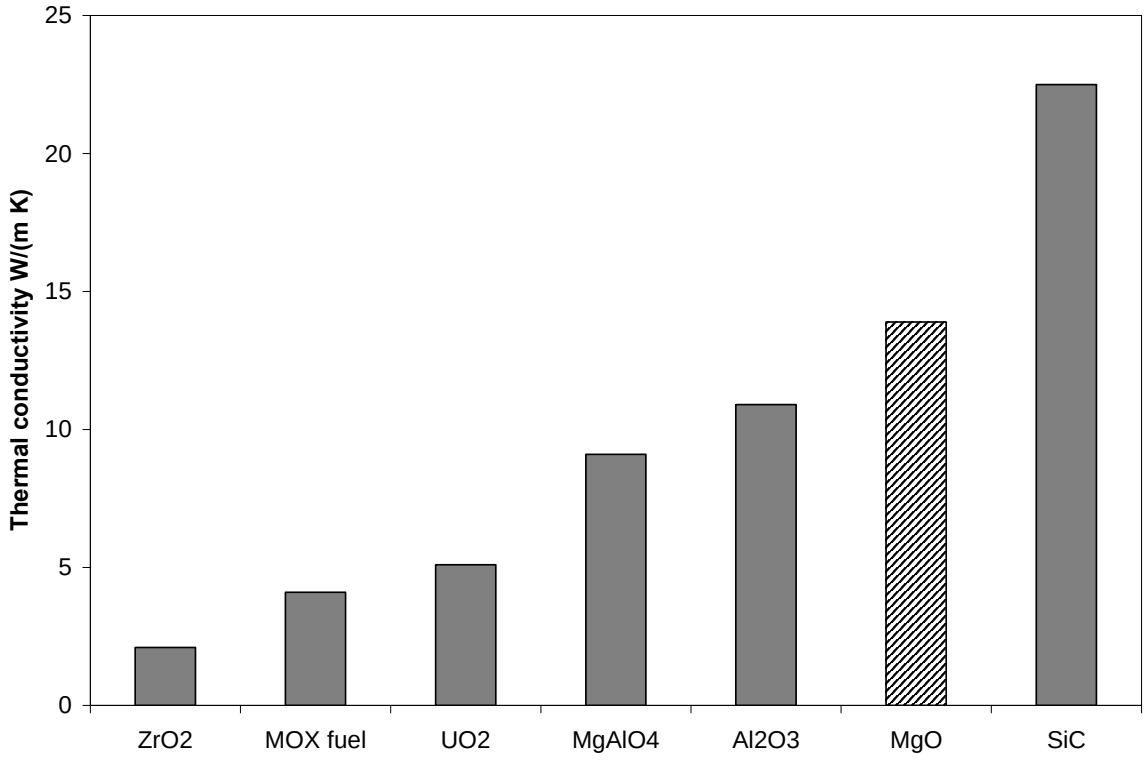

Figure 2.4. Thermal conductivity of MgO compared to selected refractory materials at 500^{o}C.

not due to the grain size effect. Thermal conductivity of UO_2 [31] is included for comparison.

Thermal conductivity of MgO is shown in comparison with selected refractory materials in Figure 2.4. All thermal conductivity data is from Kirk et al. [21]. Ceramic materials included in Figure 2.4 are either currently used as fuels in LWRs (UO_2, MOX), or proposed as matrices in IMF (ZrO_2, $MgAlO_4$, Al_2O_3, MgO, SiC). As evident from Figure 2.4, MgO is surpassed only by SiC, and has a thermal conductivity 2.7 times greater than UO_2. The high thermal conductivity of MgO makes it particularly attractive for use as a matrix material in IMF.

2.2.3 Thermal expansion

Published [32, 33, 34, 35] experimental values of thermal expansion coefficients for MgO and UO_2 [26] are shown in Figure 2.5. As shown in Figure 2.5, the thermal expansion is greater for MgO. Thermal expansion mismatch between MgO and fissile material may have a negative effect on the performance of the proposed MgO-based IMF, particularly if dispersed fuel is chosen. If the thermal expansion of the matrix is greater than the thermal expansion of the fissile particulate, a separation of the fissile particulate from the matrix may occur in case of a rapid fuel temperature rise, resulting in poor heat transport from the particulate to the matrix. The latter would lead to an increase of temperature within a fissile particle and enhanced fission gas release. In addition, the greater thermal expansion of MgO gives rise to tensile stresses in the matrix upon cooling from the sintering temperatures during the manufacture process.

Greater thermal expansion of the fuel results in an increased load on the cladding during a rapid fuel temperature rise common during Reactivity Initiated Accidents. On the other hand, higher thermal conductivity of MgO would lead to lower operating temperatures of the MgO-based IMF, which would result in somewhat lower thermally-induced strains.

Thermal expansion of MgO is isotropic due to its cubic crystal structure.

2.2.4 Young's modulus

Young's modulus of MgO [29, 32, 36, 37, 38] as a function of temperature is shown in Figure 2.6. White and Anderson (1966) and Anderson et al. (1991) reported the experimental values of bulk modulus. The values of bulk modulus were converted to the values of Young's modulus using expression $K = E/3(1-2\nu)$ with $\nu = 0.18$. According to Nishida et al. [39] Young's modulus of high-purity polycrystalline magnesia is unaffected by the grain size. The Young's modulus for UO_2 [40] is included in Figure 2.6 for comparison.

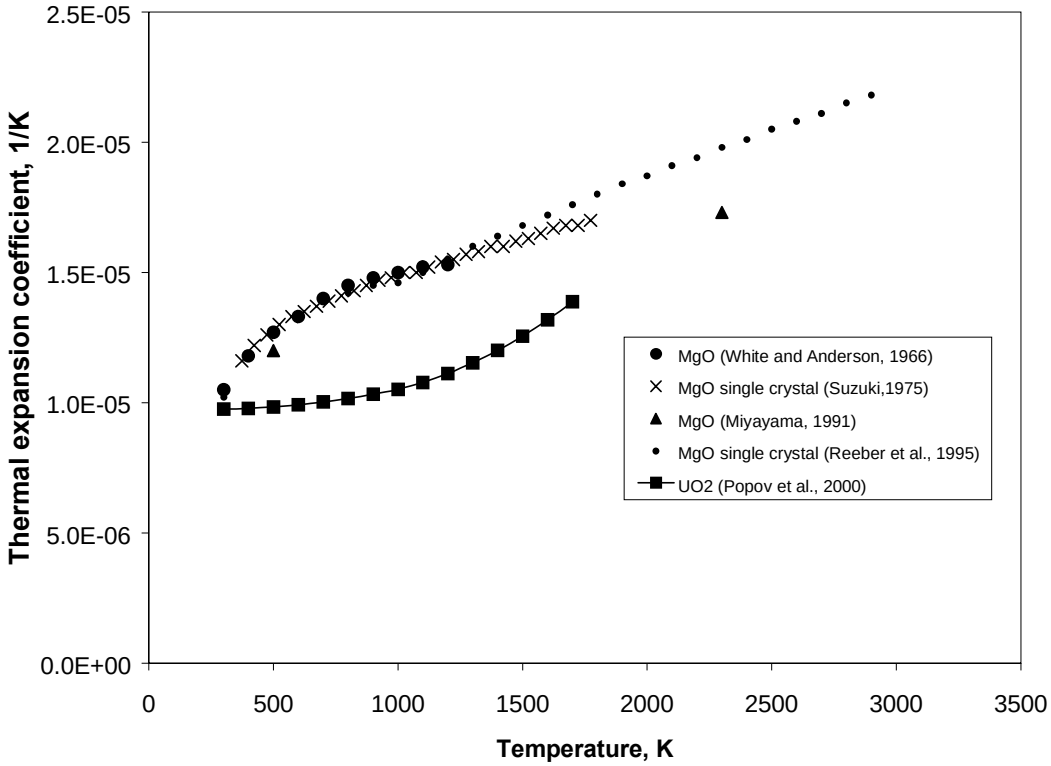

Figure 2.5. Thermal expansion coefficient as a function of temperature.

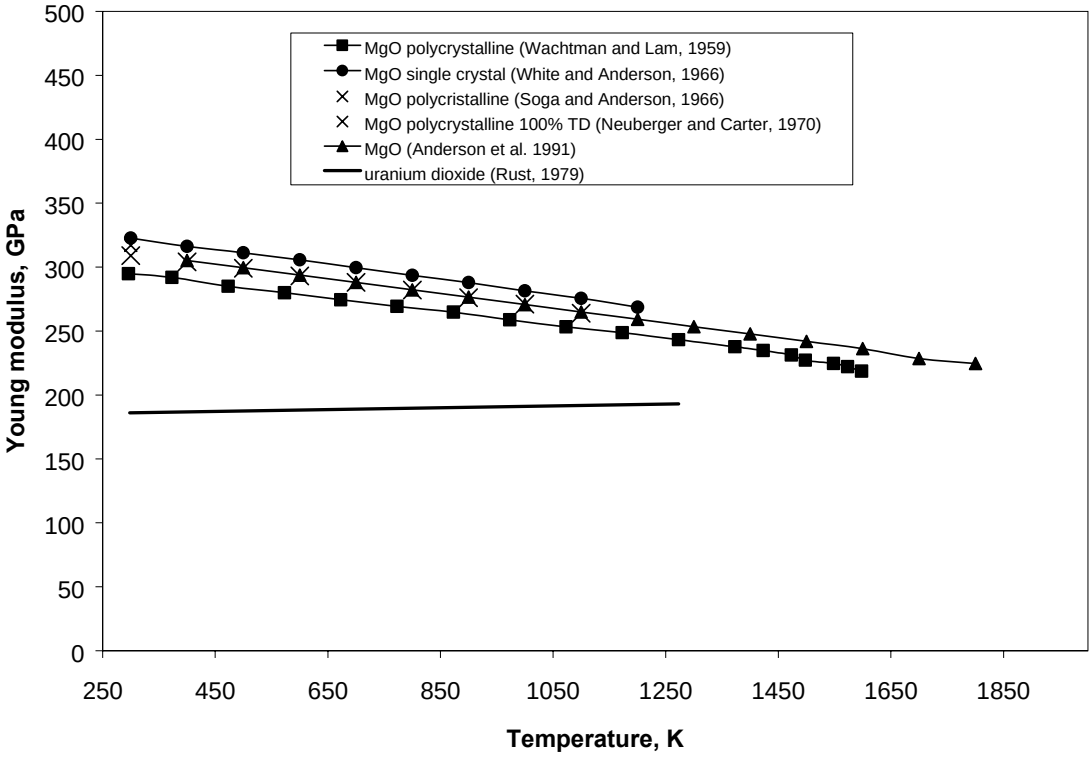

Figure 2.6. Young's modulus of MgO and UO_2 as a function of temperature.

2.2.5 Thermal creep

Thermal creep of polycrystalline MgO appears to be slightly higher than that of UO_2 as shown in Figure 2.7. The UO_2 data was published by Kingery et al. [41]. The solid line in Figure 2.7 represents the MgO secondary creep rate calculated using the model by Wilshire [42]. In this model the steady-state creep rate is determined as follows:

$$\dot{\varepsilon} = \theta_1\theta_2\exp(-\theta_2 t) + \theta_3\theta_4, \text{ where} \tag{2.1}$$

$$\ln \theta_1 = -19.57 + 0.8902 \times 10^{-2}\,\sigma + 0.08768\,T - 0.4091\times10^{-4}\,\sigma\,T \tag{2.2}$$

$$\ln \theta_2 = -29.87 + 0.1347 \times 10^{-1}\,\sigma + 0.02152\,T - 0.2023\times10^{-4}\,\sigma\,T \tag{2.3}$$

$$\ln \theta_3 = -43.11 + 0.1473 \times 10^{-1}\,\sigma + 0.16510\,T - 0.1464\times10^{-3}\,\sigma\,T \tag{2.4}$$

with time (t) in seconds, temperature (T) in Kelvins, and stress (σ) in megapascals.

Evans et al. [43] offer a creep deformation mechanism map for MgO, suggesting that Coble, Nabarro-Herring, Dislocation Climb, and Dislocation Glide creep mechanisms are possible in MgO.

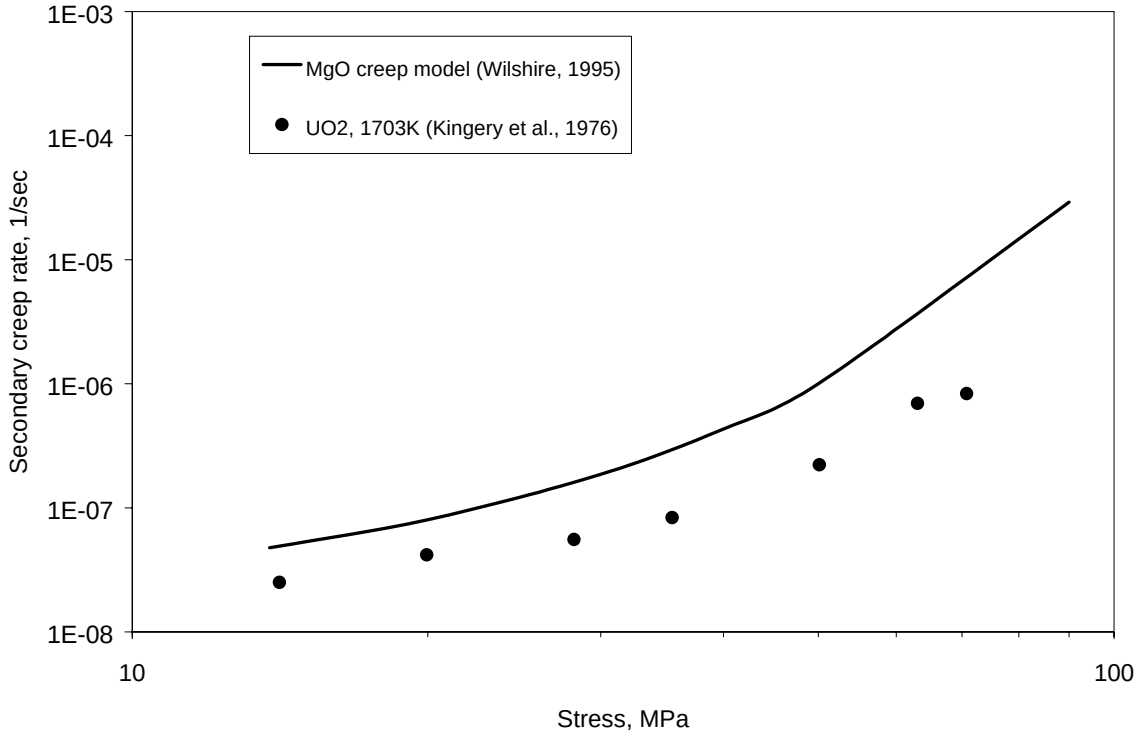

Figure 2.7. Secondary creep rate of MgO and UO_2.

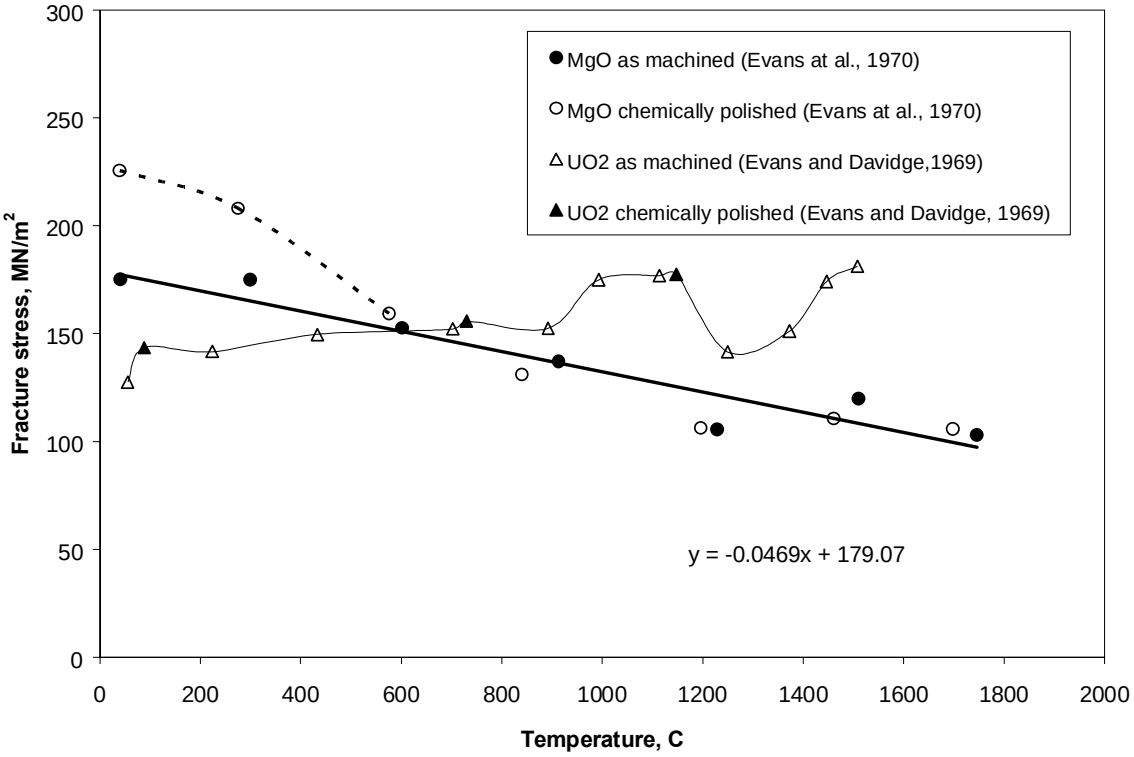

Figure 2.8. Fracture strength of MgO and UO_2 at three point bending.

2.2.6 Fracture strength

Results of three-point bend tests for MgO [44] and UO_2 [45] are shown in Figure 2.8. Both MgO and UO_2 had a grain size of 25 μm. MgO was fully dense, while was UO_2 had a density equal 97% of the theoretical density.

According to the investigators, in both instances the fracture occurred by the extension of inherent flaws at low temperatures, or was initiated by plastic flow at high temperatures. The fracture strength was found to increase with the decrease of the grain size.

As evident from Figure 2.8, fully dense MgO has greater fracture strength at temperatures below 600°C. At temperatures above 600°C UO_2 (97% TD) surpasses MgO in fracture strength.

2.2.7 Thermal shock resistance

Thermal shock resistance is the ability of a material to withstand fracture from thermally induced stress. The thermal shock resistance is the best for materials that have high fracture strength (σ_f), high thermal conductivity (k), but low elastic modulus (E) and low coefficient of thermal expansion (α_l). One way to quantify thermal shock resistance is by a simplified thermal shock resistance parameter TSR [46]:

$$TSR = \frac{\sigma_f k}{E \alpha_l} \tag{2.5}$$

The thermal shock resistance parameter for MgO and UO_2 calculated using the data from the previous sections is shown in Figure 2.9 as a function of temperature. MgO exhibits better thermal shock resistance at the temperatures below 1000 ^oC. This implies that MgO based IMF is likely to experience less thermally induced cracking during the steady-state reactor operation. This is consistent with findings of Freshley and Carroll [47] suggesting that MgO-PuO_2 fuel does not crack as extensively as UO_2 and is capable of operating at higher heat ratings.

2.2.8 Volatilization of MgO at high temperatures in different atmospheres

Livey and Murray [48] examined published experimental data to estimate the rates of loss in weight of MgO samples expected under equilibrium conditions for the various atmospheres such as oxidizing atmosphere containing water vapor, reducing atmosphere, inert atmosphere, and vacuum. According to Livey and Murray magnesia volatilizes readily in vacuum and reducing atmosphere. Volatilization is rather moderate in inert atmosphere, and insignificant in oxidizing atmosphere containing water vapor**.** The following was predicted by Livey and Murray:

- Reducing atmosphere: complete loss of a 10x4.5x4 inch crucible after firing at 1600^{o}C for 106 min. At 1700^{o}C complete loss of an identical crucible occurs after 6 minutes.

$$MgO\ (s) + CO\ (g) \leftrightarrow Mg\ (g) + CO_2\ (g) \qquad (2.6)$$

- Vacuum: rapid vaporization.

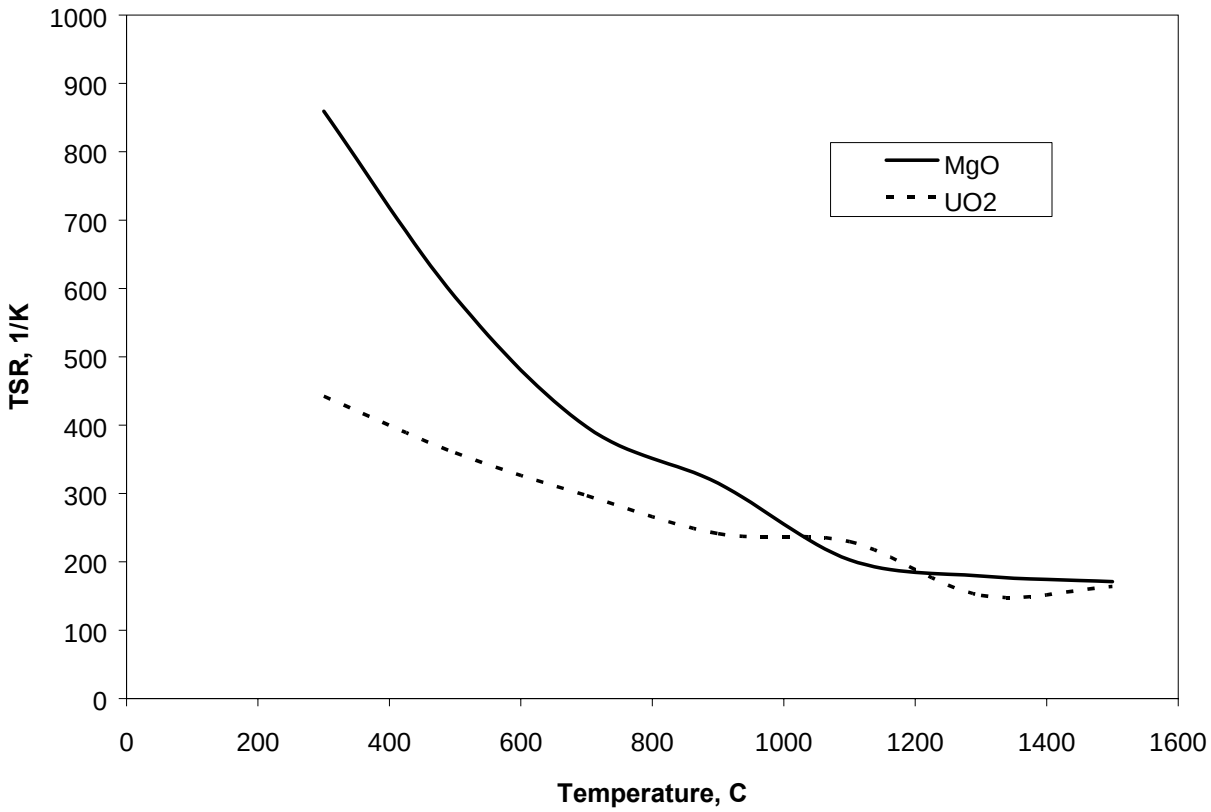

Figure 2.9. Thermal shock resistance parameter for MgO and UO_2.

$MgO\ (s) \leftrightarrow Mg\ (g) + ½\ O_2\ (g)$ (2.7)

- Inert atmosphere: 1.25% weight loss for the crucible of the above dimensions after firing for 2 hours at 1600°C.

$MgO\ (s) \leftrightarrow Mg\ (g) + ½\ O_2\ (g)$ (2.8)

- Oxidizing atmosphere containing water vapor: 0.1% weight loss in weight for the crucible of the above dimensions after firing for 2 hours at 1600°C.

  $MgO\ (s) + H_2O\ (g) + ½\ O_2\ (g) \leftrightarrow Mg\ (OH)_2\ (g)$ (2.9)

2.3 THERMO-MECHANICAL PERFORMANCE OF NEUTRON-IRRADIATED MAGNESIUM OXIDE

2.3.1 Anticipated irradiation conditions

If used as the inert matrix material for IMF in a LWR, MgO will be subject to fast neutron fluence of up to 1.2×10^{22} n/cm^2 (E>1 MeV). An estimate [2] based on the results of irradiation of MgO-PuO_2 fuels suggested that at a linear power of 590 W/cm the fuel centerline temperature is about 700 $\pm$140 °C.

2.3.2 Neutron irradiation induced defects in MgO

A number of studies focusing on assessing the damage caused to MgO by fast neutrons have been carried out (listed in chronological order in Table 2.2). Most of the investigations included in Table 2.2 were performed at the temperatures and fluences lower than that expected in an LWR.

The nature of neutron-induced damage to MgO depends on fast neutron fluence and irradiation temperature. At low fluences irradiation of MgO results in formation of isolated point defects: interstitials and vacancies. Upon further irradiation or upon annealing, interstitials coalesce to form loops. According to Groves and Kelly [49] these are unfaulted interstitial dislocation loops formed with Burgers vectors b=1/2<110> on {110} planes. The size of loops increases and their number density decreases with the increase of fluence or temperature. For example, the loops of <5nm diameter were identified in MgO irradiated to the fast neutron fluence of $4x10^{21}n/cm^2$ at 473K, while 5-30 nm loops were found in MgO irradiated to $6x10^{21}n/cm^2$ at ~923K [55]. Further irradiation ($3x10^{22}n/cm^2$, 430K, Clinard et al., [61]) results in loop growth anisotropy leading to loops elongated along <110>, and intersection of loop to form dense dislocation networks.

Table 2.2. MgO fast neutron irradiation experiments.

Reference	T, ^{o}C	Fluence, n/cm^2	Material
Groves and Kelly [49]	<200^{o}C 600^{o}C	4x10^{19} 5.4x10^{19}	single crystal
Sambell and Bradley [50]	150	2.4x10^{19}-1.7x10^{20}	single crystal
Bowen and Clarke [51]	150	3x10^{19}- 4x10^{20}	single crystal
Desport and Smith [52]	150 and 1000	1.1x10^{20}-6.0x10^{20}	single crystal
Walker and Hickman [53]	75-100	4.2x10^{19}-4.5x10^{20}	single crystal
Hickman and Walker [54]	75-100	1.4x10^{19}-6.5x10^{20}	single crystal and polycrystalline
Stevanovic and Elston [55]	60-80	10^{20}	single crystal and polycrystalline
Kingery [56]	-196	4.6x10^{18}-5.6x10^{18}	single crystal and polycrystalline
Morgan and Bowen [57]	150, 600, 1000	6x10^{19}-8.8x10^{20}	single crystal
Davidge [58]	70	<10^{18}	single crystal
Henderson and Bowen [59]		10^{17}-8x10^{20}	single crystal
Howard and Sabine [60]	75-100	3x10^{19}-4.9x10^{20}	single crystal
Clinard and Hurley [61]	157	2-3x10^{22}	polycrystalline
Chauvin et al. [18]		2x10^{22}	polycrystalline
Schram et al. [62]	353-368	7.6x10^{21}	polycrystalline
Caceres et al. [63]		6.9x10^{18}	single crystal

In addition to the crystal structure damage described above, the nuclei of Mg and O are subjects to transmutation by fast neutron fluence. The neutron-induced transmutations produce gas atoms of He and Ne in MgO due to the following reactions:

$$^{24}Mg + n \rightarrow {}^{4}He + {}^{21}Ne \quad (2.10)$$

$$^{25}Mg + n \rightarrow {}^{4}He + {}^{22}Ne \quad (2.11)$$

$$^{26}Mg + n \rightarrow {}^{4}He + {}^{23}Ne \quad (2.12)$$

$$^{23}Ne + n \rightarrow {}^{23}Na + \beta \quad (2.13)$$

$$^{16}O + n \rightarrow {}^{4}He + {}^{13}C \quad (2.14)$$

According to the calculation of Wilks et al. [64], the gas consists of 58 vol. % of ^{4}He, and 42 vol. % of Ne. Gas generation rate is 0.00106 cm^3 (STP) per $1x10^{20}$ n/cm^2 (E>1MeV) per 1 cm^3 of target material. This implies that in a typical fuel pin having a fuel column length of 366 cm and the pellet diameter of 0.819 cm, the EOL (fast neutron fluence $1.2x10^{22}$ n/cm^2) amount of gaseous products from Mg and O transmutations may reach 23.7 cm^3 (STP). For comparison, 197.6 cm^3 (STP) of gaseous fission products is expected to be generated in the same fuel pin irradiated to the burnup of 1.02×10^{20}

fissions/cm^3, assuming roughly 27 of fission gas atoms produced per 100 atoms fissioned [65].

According to Morgan and Bowen [57], annealing of neutron-irradiated MgO results in formation of rectilinear inert gas bubbles. Morgan and Bowen suggested that vacancy condensation in MgO results in formation of cubical cavities that act as sinks for neon and helium produced by transmutation of Mg and O. Vacancy condensation can only occur at a certain threshold concentration of mobile vacancies. For the threshold concentration to be achieved, first, the fluence should be sufficient to generate enough vacancies, and, second, the temperature should be high enough to ensure vacancy mobility. Morgan and Bowen concluded that the annealing temperature should be above 1500^{o}C and the fluence above10^{20}n/cm^2. Specifically, bubbles having {100} surfaces and sides ranging from 40 to 400 Angstrom were observed in MgO irradiated to the fluences1-8.8x10^{20} n/cm^2 at 150^{o}C and annealed at 1500-2000^{o}C. The number density of bubbles was 1.3-4.7x10^{14} cm^{-3}. For the irradiation temperature of 1000^{o}C, fluence of 4x10^{20}n/cm^2, and annealing temperature of 1800^{o}C, the size of bubbles was 300-2000 Angstrom, and variety of bubble shapes were observed. The number density of bubbles was 4x10^9 cm^{-3}.

2.3.3 Dimensional changes in neutron-irradiated MgO and effect of thermal annealing

Effect of fast neutron fluence on the density change of single crystal and polycrystalline MgO is shown in Figure 2.10. Two trends are evident from Figure 2.10.

First, the volumetric swelling tends to increase with the fluence, as seen from the data set compiled by Wilks [66] and a data point from Clinard and Hurley [61]. Second, increase of irradiation temperature inhibits swelling, as observed for three data points obtained at elevated irradiation temperatures of 353^{o}C [62], 600^{o}C, and 1000^{o}C.

The expansion in neutron-irradiated MgO is isotropic according to Stevanovic and Elston [55].

The lack of MgO swelling data for LWR conditions is evident from Figure 2.10. It is desirable to quantify the extent of swelling for polycrystalline MgO at irradiation temperatures up to 1000^{o}C and fast neutron fluence up to $1.2x10^{22}$.

Effect of thermal annealing on linear dimensions of neutron-irradiated MgO is shown in Figure 2.11. Figure 2.11 shows that a complete recovery was achieved for the specimens irradiated at lower temperature and lower fluence, while the specimens irradiated at higher temperature and higher fluence exhibited only partial recovery. The difference is likely due to the fact that coarse dislocation loops formed in MgO at higher irradiation temperatures and higher fluences have lower mobility impeding the complete recovery.

The lack of the annealing data for the LWR conditions precludes directly applying the results shown in Figure 2.11 to the MgO-based IMF. The trends present in Figure 2.10 and Figure 2.11 allow speculating that partial annealing of linear dimensions is possible in the MgO-based IMF during a fuel temperature rise. A complete annealing is improbable due to the likelihood of coarse dislocations loops formation in MgO irradiated to the EOL fluence typical for LWR.

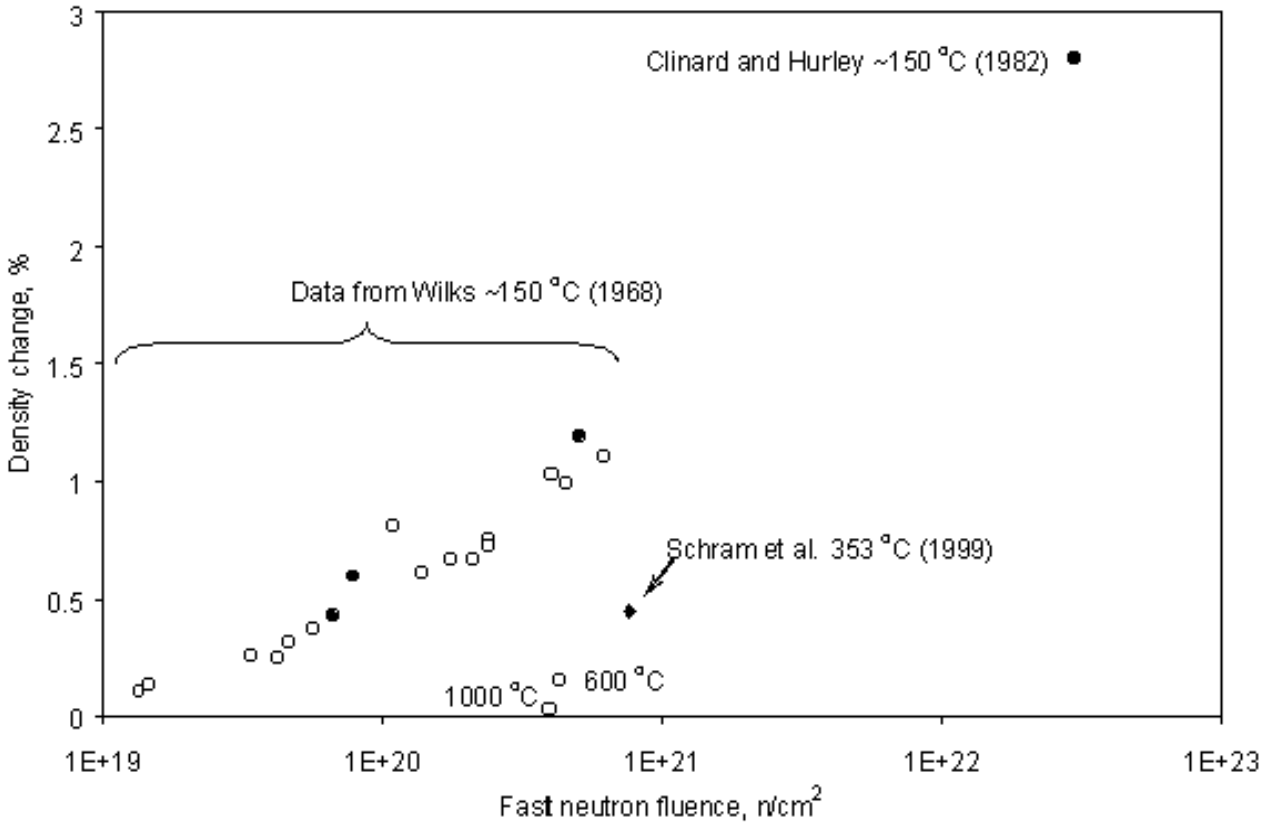

Figure 2.10. Neutron-induced density change in MgO. Open symbols indicate single crystal targets, filled symbols indicate polycrystalline targets.

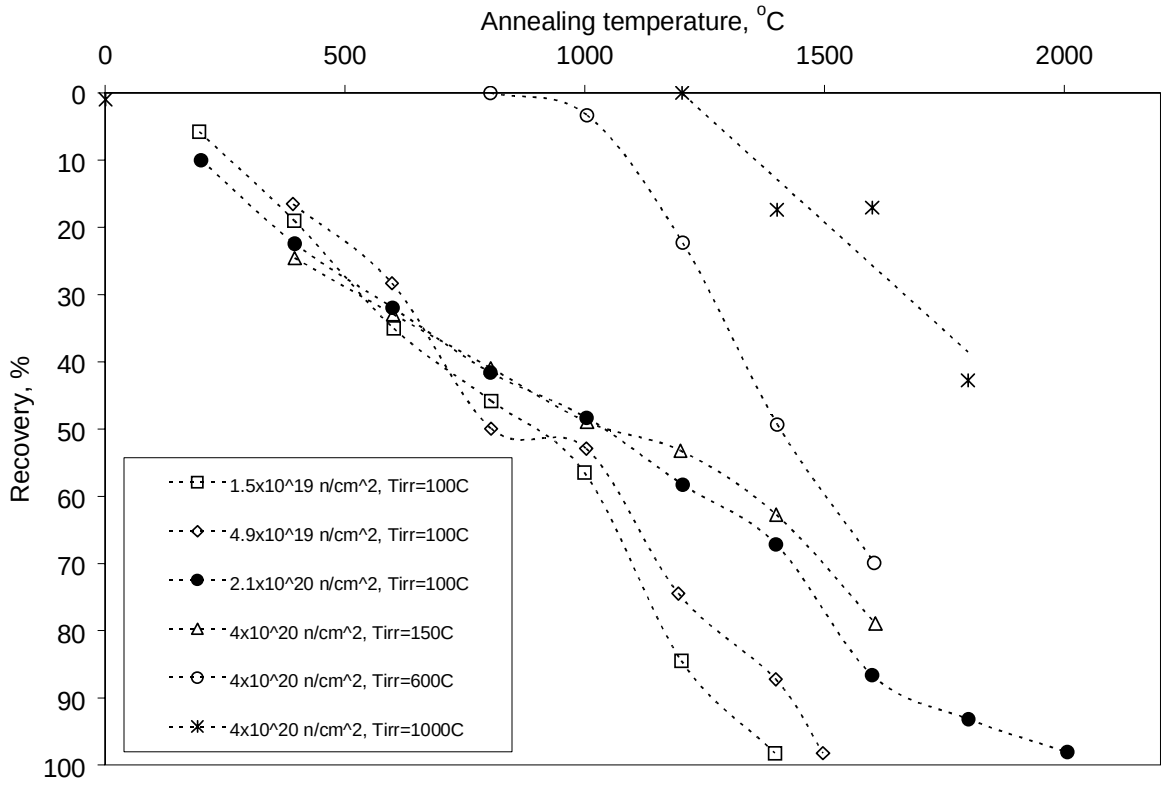

Figure 2.11. Recovery of macroscopic density of MgO on post-irradiation annealing. Open symbols indicate single crystal targets, filled symbols indicate polycrystalline targets. Reprinted from the Journal of Nuclear Materials Vol. 26, R.S. Wilks, Neutron-induced damage in BeO, Al_2O_3, and MgO: a review, Copyright © (1968) p. 170, with permission from Elsevier.

2.3.4 Effects of neutron irradiation on thermal conductivity of MgO

Thermal conductivity degradation with neutron irradiation and its recovery upon post-irradiation annealing was assessed by Stevanovic and Elston [55]. The samples of polycrystalline and single-crystal MgO were irradiated at 60-80^{o}C to the fluence of $0.8x10^{20}$ n/cm^2. Irradiated samples we subjected to 24-hr post-irradiation anneals at various temperatures. Irradiation to a fluence of $0.8x10^{20}$ n/cm^2 at ~70 ^{o}C resulted in a 44% decrease of thermal conductivity measured at 300^{o}C. Thermal conductivity was 15% less than pre-irradiation value after annealing for 24 hr at 1000^{o}C. It should be noted, that the experiments of Stevanovic and Elston featured fluence and temperature lower than that in a LWR. At this time, there is no experimental data that would help assess the extent of MgO thermal conductivity degradation at LWR conditions.

2.3.5 Effect of neutron irradiation on mechanical properties of MgO

Creation of interstitial dislocation loops formed with Burgers vectors b=1/2<110> on {110} planes, as discussed in subsection 2.3.2, hamper slip in neutron-irradiated MgO. This leads to an increase of microhardness (Groves and Kelly [49]; Stevanovic and Elston [55]; Caceres et al. [63]), fracture strength (Sambell and Bradley [50]), critical resolved shear stress (Davidge [58]) and decrease of Young's modulus (Stevanovic and Elston [55]). Increase of yield strength and thermal creep resistance is expected as well.

2.4 EFFECT OF FISSION FRAGMENT IRRADIATION

Elleman et al. [67] performed in-reactor irradiation of various ceramic materials to assess the fission fragment induced expansion. Thin ceramic specimens were placed in aluminum capsules with uranium foil attached above each specimen. The irradiation was performed in the Battelle research reactor for a time period sufficient to produce fission recoil concentrations in the specimen of 1 to $5x10^{14}$ fission fragments/cm^2. The irradiation temperature was 45^oC, and the fast neutron fluence was less then 10^{17} n/cm^2. The study has shown that the fission –fragment-induced expansion increased in the order:

$$MgO < SiO_2 < BeO < Graphite < Al_2O_3 < ZrO_2 < Pyrolitic\ Carbon < SiC$$

Further analysis by Elleman et al. included a calculation of the fission fragment induced stresses and their comparison with approximate failure stresses. These results are shown in Table 2.3. Results for other materials are included for comparison. According to the data in Table 2.3, the calculated maximum fission-fragment-induced tensile stress for MgO constitutes only 13% of the approximate tensile failure strength, and the calculated maximum fission-fragment-induced compressive stress for MgO constitutes only 7% of the approximate compressive failure strength.

Table 2.3. Calculated maximum stresses in ceramic coatings produced by fission product irradiation. Reprinted from the Journal of Nuclear Materials Vol. 15, T.S. Elleman, R.B. Price, D.N. Sunderman, Fission fragment induced expansion in ceramic materials, p. 174, Copyright © (1965) with permission from Elsevier.

Material	Calculated Maximum Stresses at 10^{14} Fission fragments per cm^2, GPa		Approximate Failure Strength, GPa	
	Tensile	Compressive	Tensile	Compressive
Graphite	2.1	11.7		
SiO2	9.0	51.7	68.9	1379.0
Pyrolytic carbon	10.3	57.9		
MgO	**13.1**	**101.4**	**103.4**	**1379.0**
Cubic ZrO_2	28.3	206.8	137.9	1379.0
BeO	40.7	289.6	117.2	1379.0
Al_2O_3	66.2	537.8	399.9	2068.4
SiC	26.2	1654.7	137.9	2068.4

Beauvy et al. [68] attempted to simulate fission product and recoil ion damage by irradiating UO_2-MgO solid solutions and composites at room temperature by krypton or cadmium ions having energy from 100 Mev to 1 GeV. Beauvy et al. concluded the MgO-based composites have shown the best behavior compared to other IMF prototypes (Al_2O_3, $MgAl_2O_4$, and $Y_3Al_5O_{12}$) irradiated within the same experiment.

Other experiments dealing with ion irradiation of MgO but not necessarily focused on assessing the fission fragment damage are listed in Table 2.4 and main findings are briefly described below. The experiments included in Table 2.4 were performed at ion energy significantly lower than the energy of fission products.

Perez et al. [69] performed a study combining optical absorption, conversion electron Mossbauer spectroscopy and TEM focused on high dose iron implantation effects in MgO single crystals. Large concentration of defects in both anionic and cationic sublattices as well as super-paramagnetic iron precipitates (~20 Angstrom in diameter), and Fe^{2+} ions were observed. The thermal annealing at 700^{o}C resulted in the removal of point defects and conversion of the iron into Fe^{3+} ions, most of which aggregated into Fe_2O_3 particles, and some located substitutionally in the MgO matrix. After annealing at 800^{o}C, the aggregates coarsened (~200 Angstrom) and $MgFe_2O_4$ or Fe_3O_4 were formed. Further coarsening of aggregates (~200 Angstrom) was observed at 900^{o}C.

Table 2.4. Experimental studies dealing with ion irradiation of MgO. (Listed in chronological order).

Reference	Incident ion	Energy (MeV)	Fluence ($1/cm^2$)	T, K
Perez et al. [69]	Fe^{2+}	0.1	$6x10^{16}$	300
Burnett and Page [70, 71]	Ti^{+} Cr^{+}	0.3	10^{16} - 10^{18}	300
Horton et al. [72]	O^{+} Fe^{2+}	2 4	$1.5x10^{18}$ $8.0x10^{16}$	575
Aoki et al. [73]	Ar^{+} Xe^{2+}	0.13 or 1.8 0.4	$1x10^{15}$ - $7x10^{17}$	
Zinkle [74]	H^{+} - Zr^{3+}	1 - 4		377
Zinkle and Snead [75]	Mg^{+}	2.4		300
Sonoda et al. [76]	He+, C+, O+, Mg+, Ar+, and Xe+	0.1-0.6		773-1073

Burnett and Page [70, 71] suggested that ion implantation to the fluence below that required for amorphization, not only hardens the surface of MgO by operation of radiation and solid-solution hardening mechanisms, but also results in the increase of chemical inertness of the surface. The latter phenomenon may assist in production of environment-insensitive surfaces resistant to different operating atmospheres. When exposed to higher ion fluences, MgO becomes amorphous. The threshold fluence for amorhization was found to be 10^{16}-10^{17} ions/cm^2. Amorphization of MgO results in the loss of hardness gained due to ion irradiation. Post irradiation annealing of the amorphized MgO resulted in precipitation hardening by formation of a variety of unknown second phases with Ti and Cr.

Horton et al. [72] reported the TEM results of ion-irradiated cross-sectional specimens of single crystalline MgO. The depth of damage consisting primarily of dislocations was 2.8μm for iron irradiation and 2.4μm for oxygen irradiation. The depth of damage was far beyond the calculated value in both cases. For both irradiations, the damage consisted of two bands where the dislocation density peaked. Between these bands the dislocation density was suppressed as compared to the rest of the profile. The location of implanted ions coincided with the low dislocation density bands on the damage profile. It was concluded that the damage is produced directly by the energetic ions rather than by stress or knock-on oxygen atoms.

Aoki et al. [73] reported effects of ion irradiation on Vickers hardness on MgO single crystals. According to Aoki et al., ion irradiation results in hardening of the surface layer in MgO at the fluences below 2.5x10^{16}n/cm^2 (see Table 2.4 for the

characteristics of ion beams used). At the higher fluences some softening was registered, but the surface was still harder than unirradiated MgO. The hardening mechanism is likely to be similar to that during the fast neutron irradiation; when forming dislocation loops hamper slip in MgO. According to Aoki et al. the softening may be due to the aggregation of gas elements and/or vacancies produced by implantation. Swelling and blisters were observed in MgO irradiated to high fluences.

Zinkle [74] utilized TEM to study radiation-induced microstructural changes in Al_2O_3, MgO, SiN_4, and $MgAl_2O_4$ ceramics after irradiation with a wide variety of energetic ion beams. The microstructural evolution of irradiated ceramics was found to be strongly affected by the irradiation spectrum. Nucleation of dislocation loops was very difficult under light ion irradiation. The processes of defect aggregate formation and amorphization were strongly dependent on the concentration and chemical nature of the implanted ion.

Zinkle and Snead [75] recommended the following ranking of ceramics with regard to increasing resistance to amorphization by ion beams:

$$SiC, SiN_3, Al_2O_3, MgAl_2O_4, MgO.$$

$MgAl_2O_4$ and MgO were found to be equally radiation resistant. This recommendation was a result of cross-sectional TEM examinations of the abovementioned materials irradiated with various ions. According to Zinkle and Snead [75] microstructure of MgO irradiated at 300K to doses of ~10dpa with 2.4 MeV Mg^+ ions consisted of a mixture of

dislocation loops and network dislocations. Zinkle and Snead speculated that the presence of network dislocation is an indicator of significant point defect diffusion, and suggests that amorphization in MgO is not possible at higher doses at room temperature in the absence of implanted impurity atoms which might trap the point defects and thereby "lock in" a thermodynamically unstable microstructure.

Sonoda et al. [76] observed formation of the ½<110> {110} type of interstitial dislocation loops under irradiation with various particles. According to Sonoda et al. [76] the formation rate of the loops increases but the growth rate decreases with the increase of the mass of the incident ions.

2.5 COMPATIBILITY OF MAGNESIUM OXIDE WITH REACTOR MATERIALS

2.5.1 High-temperature and high-pressure water

As mentioned in Section 2.2, MgO reacts with water forming $Mg(OH)_2$. The free enthalpy of formation of $Mg(OH)_2$ at 25°C (-924.7 kJ/mol) is less then the free enthalpy of formation of MgO (-601.7 kJ/mol), thus, $Mg(OH)_2$ is thermodynamically more stable than MgO in the presence of water. The theoretical densities of MgO and $Mg(OH)_2$ are 3.5 g/cm^3 and 2.4 g/cm^3 respectively, therefore, nearly 117% volumetric swelling is expected if MgO completely reacts with water forming $Mg(OH)_2$. It should be noted, that dead-burned and pure-fused MgO are rather chemically inert and do not hydrate easily.

Magnesium oxide surfaces dissociate water yielding highly hydroxilated surfaces. The reactivity of MgO surfaces towards water has been a subject of detailed theoretical and experimental investigations (eg.: Noguera [77], Abriou and Jupille [78]). The reactivity of MgO surfaces depends on their crystallographic orientation, and, according to Abriou and Jupille, the theoretical analysis suggests that water dissociation is 'forbidden' on the checkerboard MgO {100} face; however, Abriou and Jupille were unable to verify this experimentally. The latter may be due to the defects present on the freshly cleaved MgO surfaces capable of dissociating water. Abriou and Jupille further comment that that there exists a tendency of self-inhibition of water dissociation on the MgO surfaces that had prior exposure to water.

Possible interaction of MgO with the coolant water in case of the cladding breach is viewed as a main obstacle in implementing MgO-based IMF in water-cooled environments according to Freshley [2].

Freshley was the first to document of the MgO-water chemical reaction occurring after a cladding failure in the MgO-PuO_2 experimental fuel pin. The fuel pin was manufactured by swage compacting incrementally loaded arc-fused MgO (3.35mm) and calcined PuO2 (45μm). The fuel pin experienced brittle failure, associated with a massive hydride deposit on the outer surface of the cladding and severe corrosion on the inner surface. The author tentatively attributed primary failure to the reaction between 0.2% water found in MgO, residual fluoride ions from the etching process trapped in internal cladding defects, and Zircaloy. According to Freshley, the subsequent water ingress into the pin resulted in fuel swelling, splitting of the cladding, Zircaloy hydriding

and fuel washout. The post irradiation examination revealed a longitudal split in the cladding of the failed rod (0.64cm wide and 3.8cm long). The original length of the rod was 224 cm. 24 cm of fuel was lost to the coolant. Out-of-pile autoclave tests of punctured rods containing arc-fused MgO resulted in swelling of the rods having slit-type punctures, but no swelling was observed in the rods having drilled holes.

Sah et. al. [79] reported the results of post-irradiation examination of a failed MOX fuel pin irradiated in a pressurized water loop of a research reactor. In the setup described by Sah et al. the fuel pellets themselves consisted of conventional MOX fuel, but the upper and lower spacer pellets were manufactured from 90% T.D. sintered magnesia. Internal clad hydriding caused the primary failure of the cladding. Subsequent ingress of the coolant water caused excessive swelling of the MgO spacer pellets and rupture of the cladding at the MgO pellet locations. To further explore the swelling of MgO, an out-of-pile autoclave test was performed on a simulated fuel pin with magnesia spacer pellets. Both the upper and lower seals of the autoclave-tested pin had fine leaks, and the pin was positioned vertically and submerged in water. The autoclave test resulted in clad bulging at the lower end of the pin, while the upper end remained intact. The difference was due to the higher void volume in the upper end of the fuel pin. Sah et al. concluded that the sintered magnesia pellets were not compatible with coolant water, and should not be used in the pressurized water loop. The authors recommended a stringent control of the moisture content of the fuel pin to prevent internal hydriding of the cladding.

The issue of interaction of MgO-based fuel with water was addressed by Kurina et al. [80]. Unlike the previous two cases, the autoclave tested unirradiated fuel pellets consisting of UO_2 (35 wt. %), ThO_2 (33 wt. %), and MgO (32 wt. %) remained visually and compositionally intact after 50 hr in 300^{o}C water. Kurina et al. emphasized the importance of the pellet fabrication process on the water corrosion resistance of the final product. In this process, the oxide powder mixture was obtained by co-precipitation, and the precipitate was heat-treated. Subsequent steps were reduction in hydrogen, molding, and sintering in hydrogen. According to the investigators, the temperature of the heat treatment of the precipitate was a key factor affecting the quality of the final product. It was determined, that 1000^{o}C is the optimum heat treatment temperature for the above composition. The samples that received insufficient heat treatment (600^{o}C and 700^{o}C) broke down into (U, Th)O_2 powder, while MgO turned into $Mg(OH)_2$.

In a project unrelated to nuclear fuels, Monastra and Grandstaff [81] investigated kinetics of water dissolution of MgO as a potential additive to backfill Waste Isolation Pilot Plant (WIPP) repository. The studies were carried out using >99% pure, fused MgO powder consisting of 75-125 μm and 125-250 μm grain size fractions. The dissolution rate was found to be 52 μmol/m^2/min at 25^{o}C. The rate was found to be constant throughout the experiment lasting 140 hr. A very weak decrease of dissolution rate (rate order 0.07) with an increase of pH was observed (pH range 3-9.5).

2.5.2 Zircaloy

Irradiation experiments of Freshley [2] and Sah et al. [79] cited above provided no indication of chemical interaction between MgO and Zircaloy. Both studies suggest, however, that the moisture present in the fuel rod might have been a cause of the primary failure. Freshley names MgO as the source of moisture. Therefore, the MgO-based IMF should be manufactured in such way, that its moisture content remains very low. No $Mg(OH)_2$ should be present in MgO, since H_2O is a product of thermal decomposition of $Mg(OH)_2$.

Economos [82] investigated behavior MgO and other refractory oxides in contact with metals at temperatures 1400°C, 1600°C, and 1800°C. In these tests the metal pellets or powder was placed on sintered MgO discs and fired in inert atmosphere at various temperatures. MgO was found to be inert towards Zr (T_{melt}=1855°C) and Nb (T_{melt}=2477°C) metals at 1400°C and 1600°C, but a slight reaction, manifested by surface discoloration and penetration, was observed at 1800°C. The reaction products were ZrO_2 and Nb_2O_5 respectively.

Tolksdorf [83] claimed that internally oxidized Zr-1%MgO alloy surpasses Zircaloy-2 in resistance to corrosion and hydriding. Although the extent of diffusion of Mg into Zircaloy in MgO-based IMF is unknown, the findings of Tolksdorf provide some indication that presence of Mg in Zr is not detrimental, and may even be beneficial.

2.5.3 Fissile material and actinides

A list of investigations dealing with binary systems consisting of MgO and either PuO_2, UO_2, or AmO_2 is provided in Table 2.5.

Zhang et al. [84, 85] presented the most recent analysis of the available experimental data supported by theoretical calculations of the phase diagrams in the systems Pu-Mg-O and Am-Mg-O. The system MgO - PuO_2 exists when free oxygen is present, while MgO – $PuO_{1.61}$ is observed in dry inert gas atmosphere, where PuO_2 is easily reduced to $PuO_{1.61}$. Evidently, the system MgO - PuO_2 has a eutectic point at 40 mol % of PuO_2 and melts at a temperature around 2500 K. The FCC solid solution exists in the PuO_2-rich end of the phase diagram. Hough and Marples [86] proposed a terminal solubility value of 3.2 ± 1.5 mol. % of MgO in PuO_2, stating, however, that this value is uncertain. The system MgO - $PuO_{1.61}$ melts at the temperature around 2300K and has a eutectic point at 54-57 mol. %. Finally, Zhang et al. presented a calculated phase diagram for the ternary system MgO – $PuO_{1.61}$ – PuO_2 suggesting that a liquid starts to form from the fcc + halite mixture at the temperature 2450K. Based on the calculation, Zhang et al. recommended that in order to avoid the occurrence of the liquid at 2450K the mole ratio of PuO_2 to $PuO_{1.61}$ must be higher than 0.5, or the temperature should be lower than 2450K if the PuO_2 to $PuO_{1.61}$ mole ratio is 0.5.

Table 2.5. List of investigations dealing with binary systems consisting of MgO and either PuO_2, UO_2, or AmO_2.

Reference	Composition	Manufacture route	Sintering			TD, %
			T, C	Time, hr	Atmosphere	
Anderson and Johnson [87]	MgO-20-80% UO_2	Coprecipitation	1100-2150	0.1-30	vacuum	
Lambertson and Mueller [88]	MgO-0-100% UO_2	Dry mixing	1600-1750		hydrogen	
Lang et al. [89]	MgO-2-80 mole% UO_2	Dry mixing	400-2000		vacuum	
Budnikov et al. [90]	MgO-1-90% UO_2	Dry mixing	1450-2300	0.5-10	vacuum air	
Carrol [91]	MgO-0-100% PuO_2	Dry mixing	1600	20	He	
Freshley and Carrol [47] ETR	MgO-2.71% PuO_2	Dry mixing	1600	12	He	86-91
	MgO-12.95% PuO_2	Dry mixing	1600	12	He	86-91
Freshley [2] PRTR	MgO-2.1% PuO_2	Swage compacting	none	none	none	
Hough and Marples [86]	MgO - 78.8% PuO_2	Dry mixing	1250	2	O_2	98.5
	MgO – 80.5% PuO_2					
	MgO – 82.1% PuO_2					
Casalta et al. [92]	MgO - AmO_2	Dry mixing	Up to 1620	various	various	85-90
Kurina and Moseev [93]	MgO – 36% PuO_2	Coprecipitation	1500	5	vacuum	
Beauvy et al.[68]	MgO – 43%UO_2	Dry mixing	1750		Ar+5%H_2	
	MgO – 43%NpO_2		1750		Ar+5%H_2	
	MgO – 69%NpO_2		1750		Ar+5%H_2	
	MgO – 43%PuO_2		1500		Ar+5%H_2+ H_2O	
Chauvin et al. [18]	MgO-40%UO_2					
Schram et al. [62]	MgO – 2.5% UO_2	Dry mixing	1600	5	Ar+5%H_2	89.4
	MgO – 19.6% Y_xUO_x	Dry mixing	1600	5	Ar+5%H_2	80.6
Kurina et al. [80]	MgO-35%UO_2-33%ThO_2	Coprecipitation	1600		H_2	93-99

According to Zhang et al. [84] behavior of system Mg-Am-O is similar to Mg-Pu-O. Zhang et al. emphasized that the melting temperature of the MgO-AmO_{2-x} is very low (1930K) at partial oxygen pressures below 1bar. In order to raise the melting temperature to 2200K the oxygen partial pressure must exceed 4.5bar. Because, the increase of oxygen concentration results in corrosion damage of the cladding, Zhang et al. recommended that MgO is not a good matrix material for Am transmutation. It should be noted there is no experimental data supporting this recommendation.

Binary phase diagrams for MgO-UO_2 in argon and air were presented by Budnikov et al. [90]. According to Budnikov et al. the MgO-UO_2 in argon is a simple eutectic (~60 mol. % MgO) melting at 2280^{o}C. Presence of oxygen results in the formation of ternary solid solution in the uranium-rich corner of the system and a notable reduction of the melting temperature (~1750^{o}C for 40 to 100 mol. % of MgO). Therefore, the system is referred to as metastable with respect to oxygen by Holden [94]. Based on these observations, Holden suggested that the advantages of the true dispersion fuel will be lost if the UO_2 particles are dissolved to form UO_2 – MgO – O solid solution. The fabrication of a true dispersion fuel in this case is complicated due to solubility of oxygen, and reducing atmosphere is essential (Holden, [94]).

2.5.4 Fission products

Due to the limited prior use of MgO in the environment of a fission reactor, little is known about its chemical interaction with the fission products.

2.6 PRIOR AND ON-GOING EFFORTS TO UTILIZE MAGNESIUM OXIDE AS A MATRIX MATERIAL FOR IMF

2.6.1 Irradiation of MgO-PuO_2 fuel at Hanford in 1962-1963

Twenty-seven test rods of MgO-PuO_2 fuel were irradiated at Hanford in 1962-1963 as a part of plutonium utilization studies. The details of these investigations were presented by Freshley and Carroll at the 1963 ANS Winter Meeting [47], and included in Chapter 20 of the *Plutonium Handbook; a Guide to technology* [2].

Out of the twenty-seven rods, eight rods contained sintered MgO-PuO_2 pellets (four with 2.71 wt. % PuO_2 and four 12.95 wt. % PuO_2) and were irradiated in the ETR. The other nineteen rods were incrementally loaded with swage compacted arc-fused MgO and calcined PuO_2 and irradiated in the PRTR. As discussed in subsection 2.5.1. one of the nineteen swage-compacted fuel rods failed causing the termination of the PRTR experiment. However, the ETR experiment was successfully completed becoming the first demonstration of the satisfactory irradiation performance of the MgO-PuO_2 fuels.

Figure 2.12 shows the fuel centerline temperature as a function of linear heat generation rate (LHGR) plotted for the results of Freshley. Similar results for other types of fuel (ZrO_2-PuO_2 [2], UO_2 [96], SiC-PuO2 [95]) are included for comparison. It should be noted that except for the UO_2 data (FRAPCON-3, Lanning et al., 1997[96]), the trends shown in Figure 2.12 are only estimates. Nevertheless, Figure 2.12 clearly shows that use of MgO as the IMF matrix results in a significant reduction of the fuel centerline temperature due to higher thermal conductivity.

Freshley [2] provided a detailed description of the microstructure of the irradiated pellets. The samples irradiated at lower heat ratings exhibited uniform distribution of fission products over the entire surface of the sample. PuO_2 particles were uniformly dispersed throughout the MgO matrix. In the vicinity of the centerline the boundaries of PuO_2 particles were diffuse, most likely due to the release of the fission products from the higher temperature PuO_2 particles. The center region of the sample contained an unidentified white inclusion. The samples irradiated at higher power exhibited a central void formation and grain growth. The following radial regions were observed: the central void, translucent columnar grains, the area of high concentration of PuO_2 and fission products, opaque columnar grains, and undisturbed material. The chemical analyses revealed that the Pu concentration in translucent columnar grains was nearly 100 times lower than in the area of high concentration of PuO_2 and fission products, and ten times lower than in the outer region.

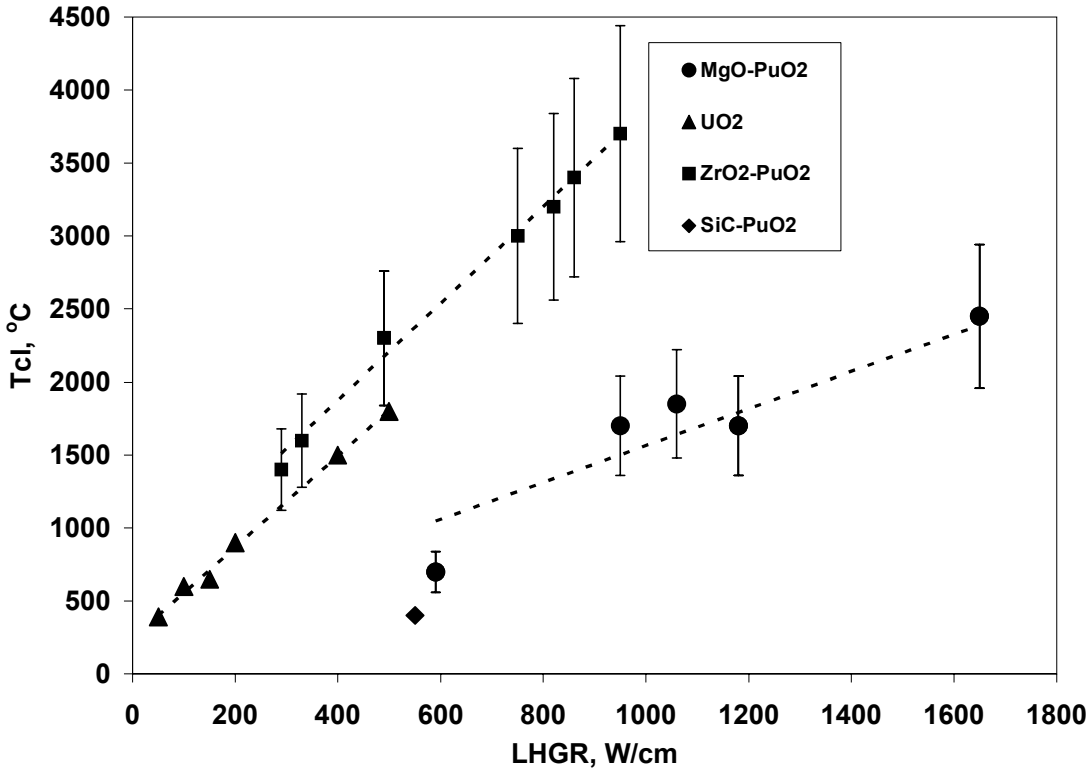

Figure 2.12. Fuel centerline temperature as a function of LHGR for various fuels.

2.6.2 Irradiations of MgO-UO_2 fuels in the Phénix reactor in 1994-1996

Two fuel pins containing MgO-40%UO_2 (19.5% ^{235}U enriched) were irradiated among nineteen IMF candidates in the Phénix reactor in France as a part of the materials selection experiment MATrices for INcineration of Actinides [18]). The irradiation time was 61 equivalent full power days. Irradiation conditions are summarized in Table 2.6. The destructive examination results were reported only for the fuel pin irradiated to the lower fluence.

Destructive examination revealed that two MgO-UO_2 pellets out of twenty-eight were broken in 2 pieces, yet no other cracking was observed on any of the pellets. The fission gas release was below the detection limit. An increase of both open and closed porosity was observed during ceramographic examination. The electron-microprobe analyses revealed that the fuel was composed of 1 - 10 μm pure UO_2 grains homogeneously dispersed in practically pure MgO matrix. Chauvin et al. concluded that MgO-based IMF showed a good behavior under irradiation. A similar conclusion was made about spinel.

Table 2.6. Irradiation conditions and results of the MATINA experiment. Only MgO-based fuels are listed.

Sample	Fast fluence, m^{-2}	Burnup UO_2, %	LHGR, W/cm	T_{cl}, ^oC	Column elongation, %	Density change, %
MgO-40% UO_2	$1.95x10^{26}$	1.27	43	~800	-0.3-0.0	From -1.06 to -1.68
MgO-40% UO_2	$5.6x10^{26}$	3.6	43	~800		

2.6.3 Irradiation of MgO-UO_2 and MgO-$Y_{5.78}UO_x$ in the High Flux Reactor in 1998

A fuel pin containing MgO-2.5 vol. % UO_2 (20% ^{235}U enriched) pellets and a fuel pin containing MgO-19.6 vol. % $(U,Y)O_x$ pellets were irradiated among sixteen other IMF candidates in the High Flux Reactor in Petten, Netherlands as a part of the Experimental Feasibility of Targets for TRAnsmutation (EFTTRA-3) experiment [14, 62]. Both MgO-2.5 vol. % UO_2 and MgO-19.6 vol. % $(U,Y)O_x$ compounds were produced by mixing the fissile particles and inert matrix and the fissile phase inclusions were in the order of 100-300 micron. The irradiation time was 198.9 equivalent full power days. The irradiation conditions and some results relevant to MgO-based fuels are summarized in Table 2.7.

Despite observed cracks possibly caused by swelling of the UO_2 inclusions, Neeft et al. [14] concluded that the performance of the MgO matrix was good.

2.7 SUMMARY

A detailed review of material properties of MgO as a candidate inert matrix for LWR Pu-bearing fuel reveals an array of features desired for such application. These include:

- thermal conductivity higher than that of UO_2,
- high melting point,
- low thermal neutron absorption cross-section,

Table 2.7. Irradiation conditions and results of the EFTTRA-3 experiment. Only MgO-based fuels are listed.

Sample	TD, %	Fast fluence, m^{-2}	Burnup, % FIMA	Pellet elongation, %	Pellet diameter increase, %	FGR Xe, %
MgO-2.5%UO_2	89±3	$6.23x10^{25}$	17.5	0.1±0.6	0.4±0.4	4
MgO-19.6 vol. % $(U,Y)O_x$	81±5	$5.98x10^{25}$	17.3	-0.4±0.4	0.1±0.5	3

- high resistance to neutron and ion irradiation,
- inertness towards the fissile phase,
- simple phase relations with fissile phase,
- low cost and ease of manufacture,
- good solubility in strong acids ensuring ease of reprocessing.

The main disadvantage of the MgO-based IMF is its reaction with water, and because of this, the use of MgO in LWRs has been discouraged by Freshley [2] and Sah et al. [79]. However, the recent autoclave tests for unirradiated fuels containing 32 wt % of MgO reported by Kurina et al. [80] show satisfactory results. Significant thermal expansion is another potential disadvantage of MgO, although it may provide a negative reactivity feedback.

Significant progress has been made in developing the MgO-based IMF. The technology to manufacture MgO-based IMF is available. Both co-precipitation and powder mixing manufacture routes yielding either micro- or macro-dispersions have been proven feasible. The irradiation experience of MgO based IMF includes 31 fuel rod with burnup up to 64% fissile atoms and LHGR up to 1650 W/cm. All irradiation experiments involving sintered MgO-based IMF are described as successful. There exists, however, a record failure of swage-compacted MgO-PuO_2 fuel.

Future work on developing MgO-based IMF for LWRs is only feasible if its stability in water is demonstrated. The water - MgO interaction can be investigated in an autoclave, and such phenomena as MgO dissolution, swelling due to $Mg(OH)_2$ formation, and washout of the reaction products from the fuel rod can be quantified. In

addition, the effect of MgO grain size, sintering temperature, and effect of burnable neutron absorbers and fissile material on the MgO-water reaction must be investigated. The work of Kurina et al. [80] sets a good example of such study; however, this work alone cannot be used as evidence of MgO-based IMF stability in water due to a low content of MgO (32%) in the fuel composition proposed by the authors.

No experimental data describing the behavior of MgO in contact with neptunium oxide and burnable neutron absorbers is available. Effect of these additions on the melting temperature, and the phase composition of the IMF must be investigated. Possible effect of these additions on the stoichiometry of the plutonium oxide requires attention as well.

No experimental data exists characterizing the thermal conductivity degradation of MgO with fast neutron fluence at LWR conditions. This data can be obtained by irradiation of polycrystalline MgO targets at temperatures of 300-1000^{o}C and fluences up to 1x10^{22} n/cm^{2} and post-irradiation conductivity measurements. The study of Stevanovic and Elston [55] indicates that there exists a notable degradation of thermal conductivity of neutron-irradiated MgO, however, this study was conducted at the fluence and temperature lower then typical for a LWR. The data on neutron induced swelling and thermal annealing is needed as well and can be collected from the samples used for thermal conductivity measurements.

No experimental data exists assessing the extent of interaction between MgO and Zircaloy. The study of Economos et al. [82] indicates that a reaction may occur at the temperatures above 1800^{o}C, but these tests are not fully representative of LWR

conditions, because zirconium used in these tests was in the form of a pellet/powder. It is desired to investigate possible interaction of MgO with Zircaloy by conducting experiments in which polished MgO ceramic surface would be pressed against Zircaloy surface and heated to the temperatures up to 2000^{o}C.

Although the review presented in Section 5 suggests that MgO is highly resistant to fission fragment damage, the value of the threshold ion fluence required to amorphize MgO at the temperatures typical for LWR is unknown. This threshold fluence can be determined experimentally by irradiation of MgO ceramic samples with beams of fission products at fission energy (e.g. 72 MeV iodine ions) from an accelerator.

Desired fissile phase, minor actinide, and burnable neutron absorber concentrations must be determined by conducting a neutronic calculation. The concentrations must be optimized from the standpoint of core criticality and control.

Radial burnup and radial power profile evolution must be calculated for the proposed fuel using a neutron transport computer code. Due to plutonium self-shielding higher fission rates are expected at the fuel pellet periphery. A burnup calculation would yield the information on fission product distribution, including the amount of generated fission gas.

Steady-state fuel performance modeling would be complicated and is likely to produce uncertain results due to the lack of experimental data on thermal conductivity of the proposed fuel, fission product migration, and effect of irradiation on mechanical properties. Modeling of transient response of the MgO-based IMF is expected to be more informative, revealing, for example, the effect of higher fuel thermal expansion on

the cladding strain during a rapid fuel temperature rise, or effect of higher thermal conductivity on behavior of the fuel rod during a loss of coolant accident. Transient analysis of the of the BOL fuel rods would produce less uncertainties, since it can be carried out without taking into account the long-term irradiation effects.

CHAPTER III

DEVELOPMENT AND CHARACTERIZATION OF MAGNESIA-BASED CERAMICS WITH IMPROVED HYDRATION RESISTANCE

3.1 PRELIMINARY CONSIDERATIONS

To develop magnesia-based ceramics with improved hydration resistance, the phenomenon of magnesia hydration and possible strategies to disrupt hydration were further investigated by reviewing the relevant literature and conducting a set of preliminary experiments. The findings of these research efforts are discussed herein.

3.1.1 Observations of magnesia hydration

As stated earlier, hydration of magnesia in hydrothermal conditions is catastrophic and results in a complete conversion to hydroxide. Neither single crystals, nor polycrystals of near theoretical density are immune. Kitamura et al. [97] has demonstrated that both are destroyed within 10-20 hours in saturated water vapor at 200oC. These observations related to magnesia ceramics were reproduced in this work by conducting hydration tests on magnesia ceramics. Immersion-type hydration tests were performed in boiling water at atmospheric pressure and in a water-filled pressure vessel at 300^{o}C. Effect of the exposure to the boiling water was investigated by visual

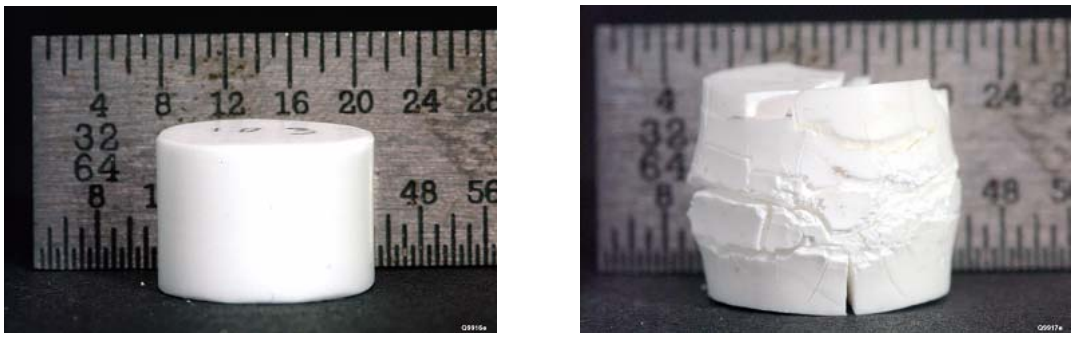

Figure 3.1 As manufactured magnesia ceramic pellet (left) and a magnesia ceramic pellet after a 3-hour exposure to the boiling water (right).

observation, optical microscopy (Trinocular Stereoscopic Zoom Microscope Nikon SMZ-2T), and scanning electron microscopy (SEM, Zeiss DSM960A). Figure 3.1 illustrates severe degradation of a magnesia ceramic pellet (density 2.99 g/cm^3) caused by exposure of the pellet to the boiling water. Profuse cracking and swelling caused by hydration are difficult to overlook.

Optical microscopy of a polished and thermally etched surface of magnesia ceramic (density 3.45 g/cm^3), exposed to the boiling water, revealed that cracks develop within an hour of exposure (Figure 3.2). Cracks propagating from the surface of the pellet were found on the polished and thermally etched cross-section of magnesia ceramic briefly exposed to the water at 300^{o}C (Figure 3.2). SEM provided additional evidence (Figure 3.3) of the degradation believed to be caused by hydration. These observations, once again, rule out safe use of pure magnesia as an inert matrix for LWR fuels.

3.1.2 Nature of the hydration problem and possible solutions

Kitamura et al. [97] proposed the following hydration mechanism for magnesia polycrystals. The hydration attack begins on the grain boundaries near the surface of polycrystalline magnesia. It causes grain boundary destruction, disintegration of the polycrystal, first into finer particles, then into single crystals, with consequent hydration of single crystals. The process is shown schematically in Figure 3.4. This figure depicts a sequence of events that occur when a group of magnesia grains is attacked by water. Figure 3.4a shows initial stage of the process characterized by hydration of exposed

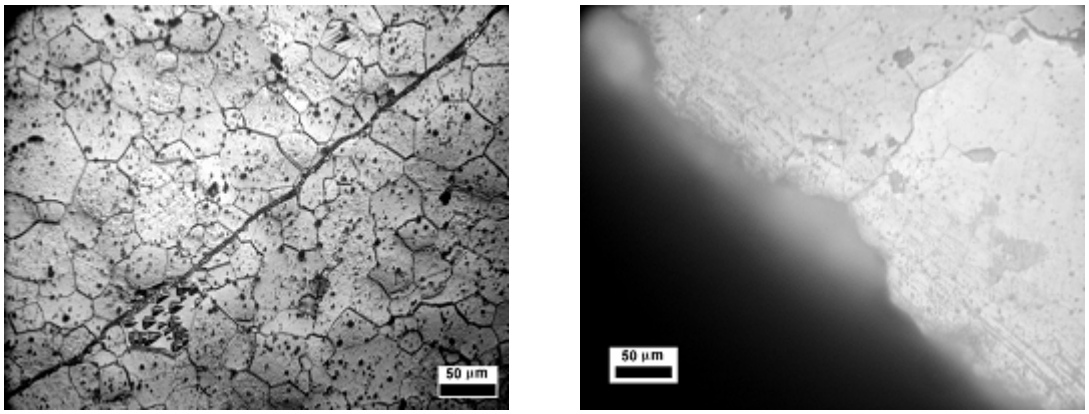

Figure 3.2. Cracks observed in magnesia ceramics exposed to the boiling water (left) and 300^{o}C water (right).

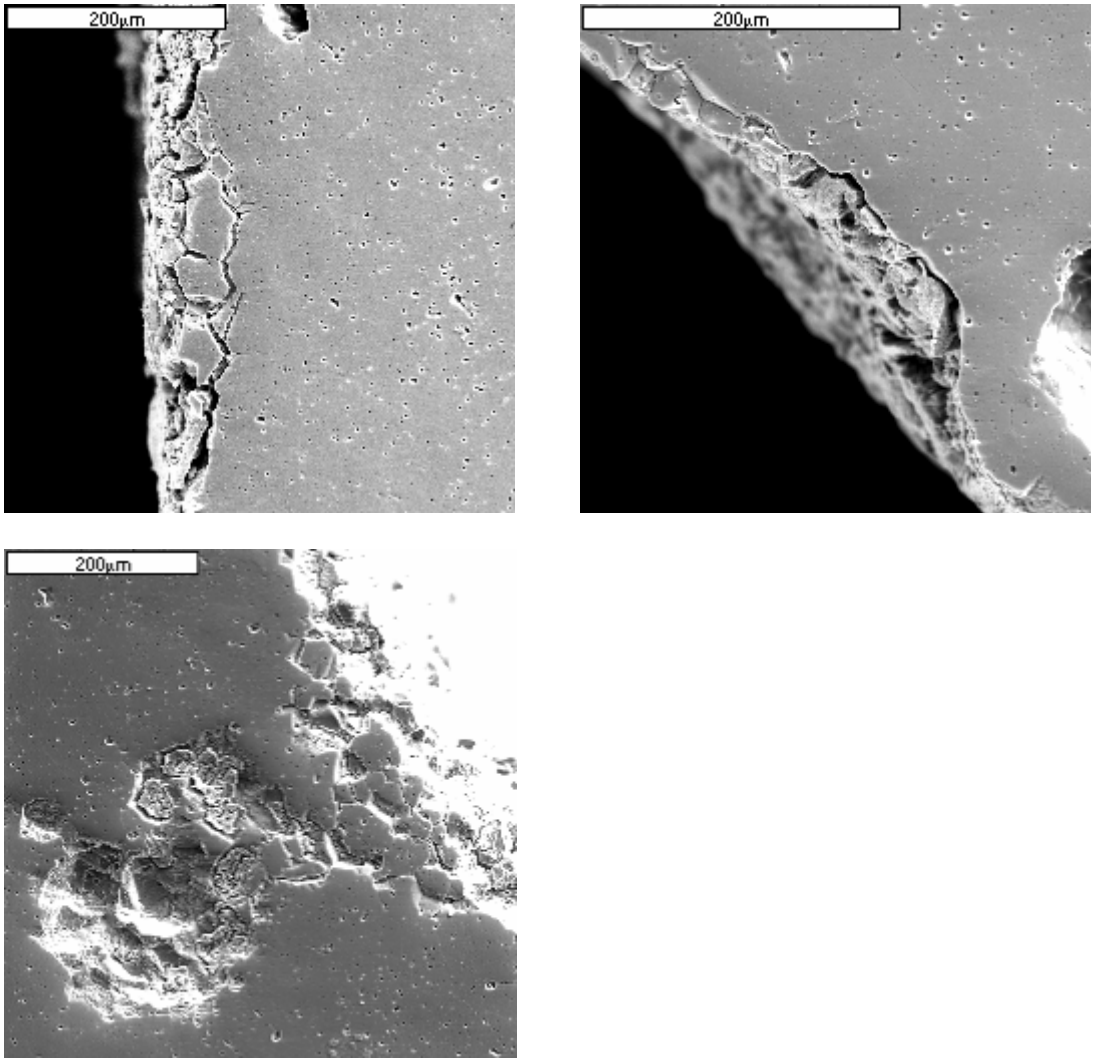

Figure 3.3. SEM images of magnesia cross-sections after exposure to 300°C water.

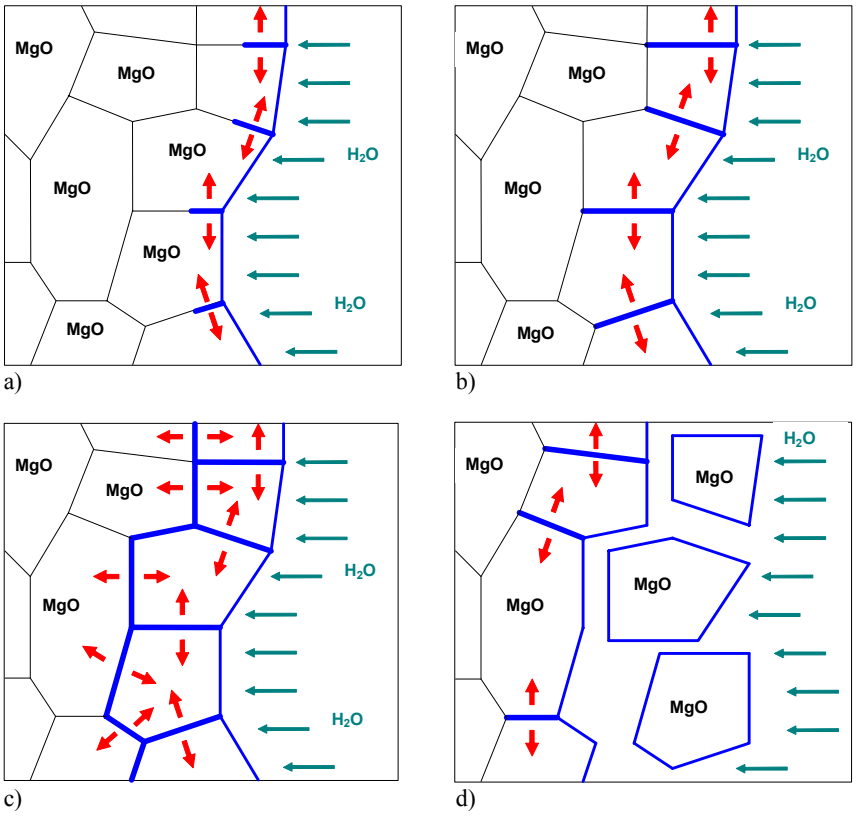

Figure 3.4. Destruction of polycrystalline magnesia by hydration of grain boundaries.

grain surfaces and grain boundaries. Blue color signifies the hydration product, magnesium hydroxide. The chemical reaction between magnesia and water is accompanied by a volume increase of 117%. As a result, the hydration product, forming on the grain boundaries, exerts stresses on the neighboring grains. The stresses are shown as red arrows. With the buildup of the hydration product on the grain boundaries, the stresses become large enough to initiate grain boundary cracking. The cracks serve as pathways for the water exposing more magnesia available for hydration (Figure 3.4b and Figure 3.4c). Finally, the grain boundaries of the first layer of grains are destroyed, and the first layer of grains is detached from the monolith (Figure 3.4c). The process then repeats itself until the entire polycrystalline monolith is powderized, i.e. reduced to individual grains. Hydration of individual grains separated from the monolith continues at a slower rate until all magnesia is converted to hydroxide.

The following measures are likely to be effective in reducing the hydration rate:

- Surface coating which acts as a physical barrier separating water from magnesia;
- Use of additives resulting in a formation of a hydration-resistant grain boundary phase, solid solution, or a multiphase system.

Coating individual fuel pellets to protect them from hydration is not viable due to the cost considerations. Furthermore, radiation induced swelling, cracking due to thermal gradients, and fission gas release associated with fuel operation would constantly challenge the integrity of the coating. Therefore, the use of additives is a more promising proposal, given the nature of the intended application. It is known, that some oxide additives have long been used to control the sintering kinetics,

microstructure and toughness of magnesia ceramics [98,99]. However, their effect on hydration has never been fully investigated. This study will address this aspect.

3.1.3 Selection of an additive to improve hydration resistance of magnesia

The initial search of candidate additives was focused on classic refractory materials: zirconia (ZrO_2), alumina (Al_2O_3), silica (SiO_2), and spinel ($MgAl_2O_4$). Members of this list have high melting temperatures, low neutron absorption cross-sections, and are highly hydration-resistant. It is understood, that this list is far from being exhaustive. Other materials, such as NiO, BeO, ZrC, SiC, AlN, and $ZrO_2 \cdot SiO_2$ may be effective additives as well. However, recognizing the budget and time limitations of this project, only materials included in the first list were given further consideration.

To select an additive from the list of candidates discussed above, a set of quick preliminary experiments was conducted. Binary ceramic composites containing magnesia and one of the following: zirconia, alumina, silica, and spinel; were fabricated using conventional pressing and sintering techniques. Resulting pellets were tested for hydration resistance in boiling water. Among tested combinations only magnesia-zirconia composites containing up to 50 mol. % of zirconia have shown an improvement in hydration resistance. Based on these results, zirconia was selected as an additive to improve hydration resistance of magnesia. Further research was focused solely on magnesia-zirconia ceramics.

3.2 EXPERIMENTAL PROCEDURE

Once the zirconia was selected as an additive to improve hydration resistance of magnesia ceramics, a procedure to fabricate magnesia ceramics doped with zirconia was developed. This fabrication procedure and the analytical techniques utilized to characterize the microstructure of the final product are presented in this section.

3.2.1 Magnesia-zirconia ceramic fabrication

Magnesia-zirconia ceramic composites were fabricated using conventional pressing and sintering techniques. Magnesium oxide (item M-1017, lot X25111, typically 99.95% pure) was procured from Cerac Incorporated (Milwakee, WI). Magnesium zirconium oxide (stock 12343, lot C01E, 99.7% metals basis) supplied by Alfa Aesar (Ward Hill, MA) was used as a source of zirconia. When choosing the source of zirconia, the preference was given to magnesium zirconium oxide rather then pure zirconium oxide. This saved some effort required for producing a homogeneous mixture of the two. Recognizing that LWR fuels often contain burnable neutron poisons, erbium oxide (lot C25H, 99.9% metals basis), Johnson Matthey Electronics (Ward Hill, MA), was added to some compositions.

Pre-weighed amounts of magnesia, erbia, and magnesium zirconium oxide powders were combined with water in a beaker. The weight of water was approximately 3 times greater than the weight of the powders combined. The water and powder mixture were stirred using a magnetic stirring bar for 6 hours. The slurry was dried in air at 80^{o}C for 5 hours. The resulting powder was transferred into an alumina crucible

and heat-treated at 1000^{o}C for 5 hours in a high temperature tube furnace (model F59348CM-75, Barnstead International, Dubuque, IA). Time-temperature profile used during the heat treatment is shown in Figure 3.5a. Upon cool-down, zinc stearate (Fisher Scientific Fair Lawn, NJ Z-78-4, lot 871095, UPS grade) in the amount of 1% by weight was mixed into the powder using a mortar and a pestle. The powder was then pressed into pellets with a force of 10000 lbs using a cylindrical die of 0.5 inch diameter. Resulting pellets were ground into powder using mortar and pestle. The powder was passed through a sieve with an aperture size of 212 microns (ASTM-E11 #70). The mixture was pressed again into pellets with a force of 3000 lbs using a cylindrical die of 0.5 inch diameter. The pellets were placed into alumina crucibles and sintered in air for 7.5 hours at 1700^{o}C in a high temperature tube furnace (model F59348CM-75, Barnstead International, Dubuque, IA). The pellets were cooled with the furnace after sintering. Time-temperature profile used during sintering is shown in Figure 3.5b.

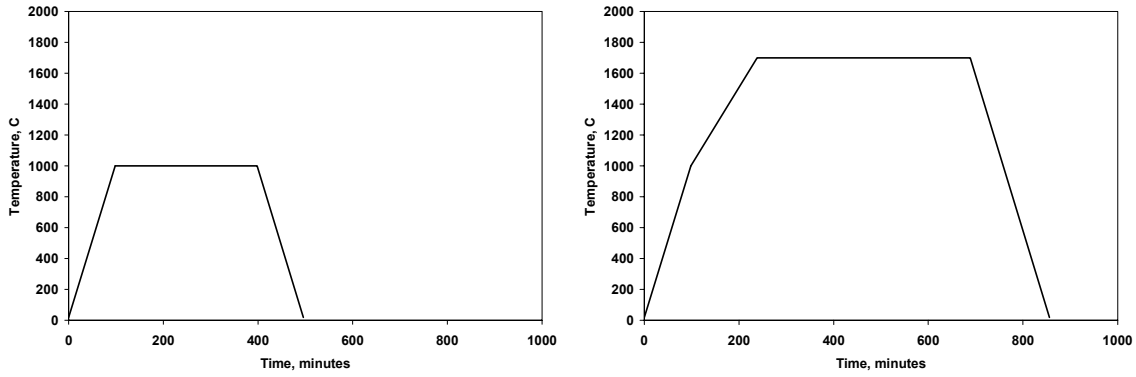

Figure 3.5. Time-temperature profiles used for heat treatment (a) and sintering (b).

3.2.2 Characterization

Sintered pellets were subjected to optical microscopy (Trinocular Stereoscopic Zoom Microscope Nikon SMZ-2T), scanning electron microscopy (SEM, Zeiss DSM960A), energy dispersive x-ray analysis (EDS, Oxford Instruments, Freemont, CA), x-ray diffraction analysis (XRD, Scintag X1), pycnometric density measurements (Ultapycnometer-1000, Quantachrome Inc, Boyton Beach, Fl), and immersion density measurements. Green density of the pressed pellets was derived from their weight and linear dimensions measured using an electronic caliper.

3.3 RESULTS AND DISCUSSION

3.3.1 Ceramic fabrication

Ceramics of three binary and three ternary compositions were fabricated. The binary compositions were as follows:

- 40 wt. % MgO, 60 wt. % ZrO_2, further referred as 40/60;
- 50 wt. % MgO, 50 wt. % ZrO_2, further referred as 50/50;
- 60 wt. % MgO, 40 wt. % ZrO_2, further referred as 60/40.

The ternary compositions:

- 37.2 wt. % MgO, 55.8 wt. % ZrO_2 7 wt% Er_2O_3, further referred as 40/60-Er;
- 46.5 wt. % MgO, 46.5 wt. % ZrO_2 7 wt% Er_2O_3, further referred as 50/50-Er;
- 55.8 wt. % MgO, 37.2 wt. % ZrO_2 7 wt% Er_2O_3, further referred as 60/40-Er.

Fabrication of ceramics of several compositions was undertaken in order to provide further opportunity to explore possible compositional dependence of the microstructure and properties of the final product.

Photographs of ceramic pellets are shown in Figure 3.6. The pellet on the left is light pink due to erbia doping.

3.3.2 Optical microscopy

Optical microscopy proved irreplaceable as a quality assurance tool during fabrication of ceramic samples. It was used to monitor homogeneity of the samples and to ensure that the samples are crack-free. Micrographs representative of each of the studied compositions are shown in Figure 3.7. White and grey fields dominate the optical micrographs. The contrast between the fields is due to the difference in the refractive indices of the corresponding phases. Because of its higher refractive index (2.13-2.19) zirconia appears as a white phase in the optical micrographs. Magnesia appears as a grey phase (refractive index is 1.736). The black features found in the micrographs are likely the voids created by the grain pull-out during ceramographic preparation of samples. Besides these voids no other indicators of porosity are present in the micrographs. This suggests that the density of samples is near theoretical.

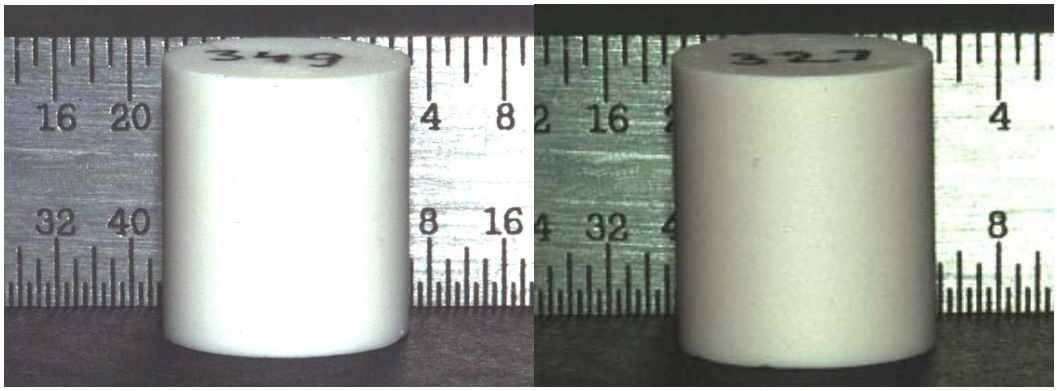

Figure 3.6. As-sintered magnesia-zirconia ceramic (60/40, left) and magnesia-zirconia ceramic doped with erbia (50/50-Er, right).

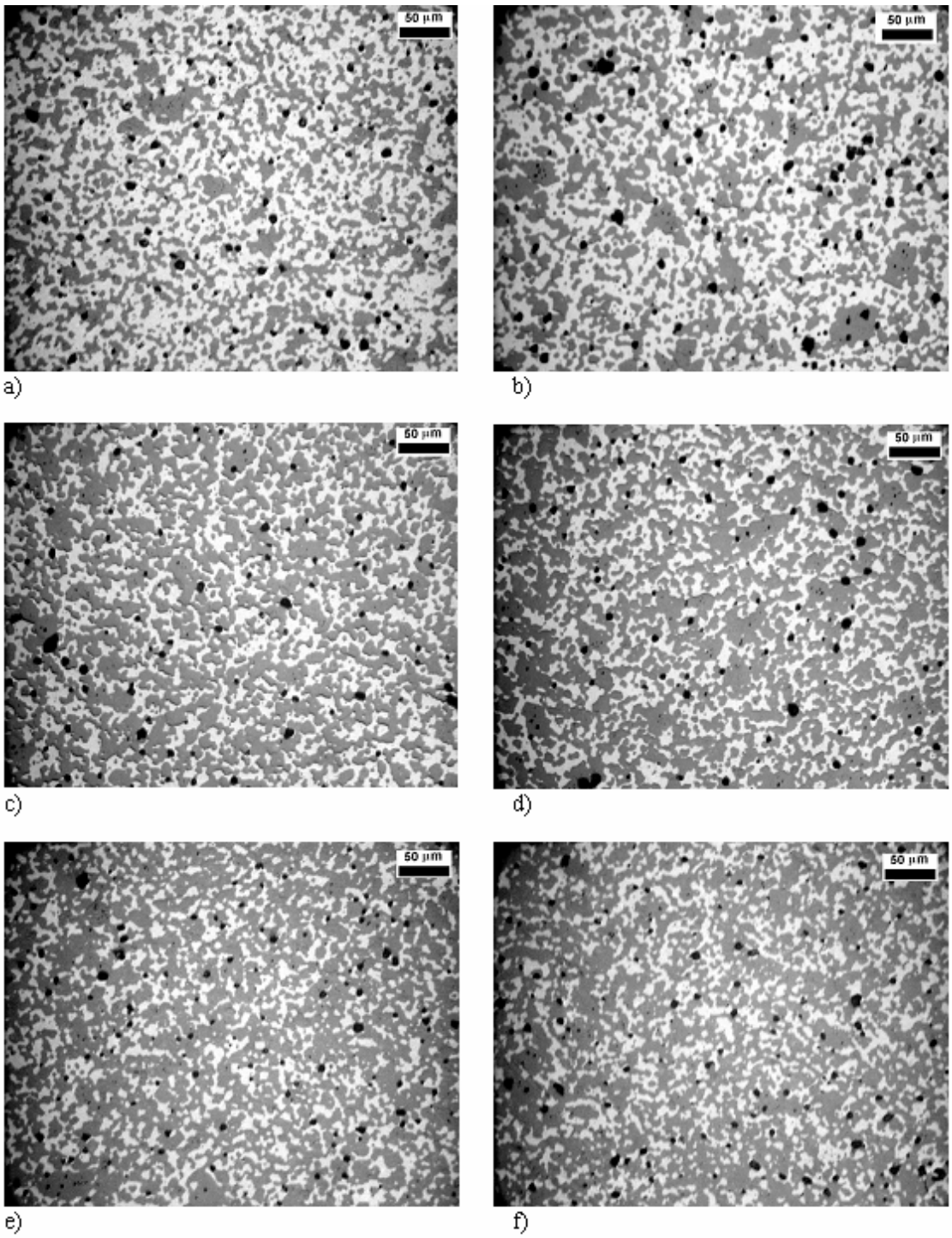

Figure 3.7. Optical microscopy images.

3.3.3 Scanning electron microscopy

3.3.3.1 SEM of binary compositions

The microstructures observed for the binary magnesia-zirconia compositions are shown in Figure 3.8, Figure 3.9 and Figure 3.10. Two phases comprise the ceramic microstructure. The dark phase is magnesia and the light phase is a magnesia-zirconia solid solution. In this system the microstructure is obviously driven by the ratio between batched amounts of the initial components. The 60/40 composition (Figure 3.8) appears as a dispersion of zirconia in the magnesia phase, while the 40/60 composition (Figure 3.10) is clearly a dispersion of magnesia in the zirconia phase. The 50/50 composition (Figure 3.9) manifests itself as a combination of two interpenetrating phases.

3.3.3.2 SEM of ternary compositions

The microstructures observed in the ternary erbia-magnesia-zirconia compositions are shown in Figure 3.11, Figure 3.12, and Figure 3.13. Two phases comprise the ceramic microstructure. The dark phase is magnesia and the light phase is erbia-magnesia-zirconia solid solution. As in the binary system described above, the microstructure of the ternary system is driven by the ratio between batched amounts of the initial components.

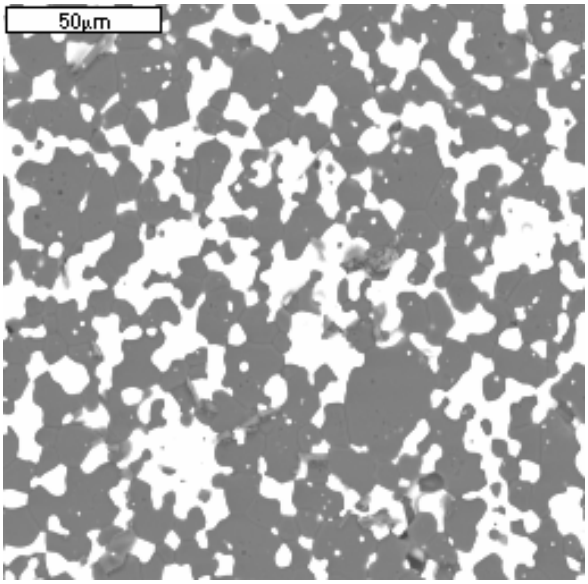

Figure 3.8. SEM image of the 60/40 ceramic.

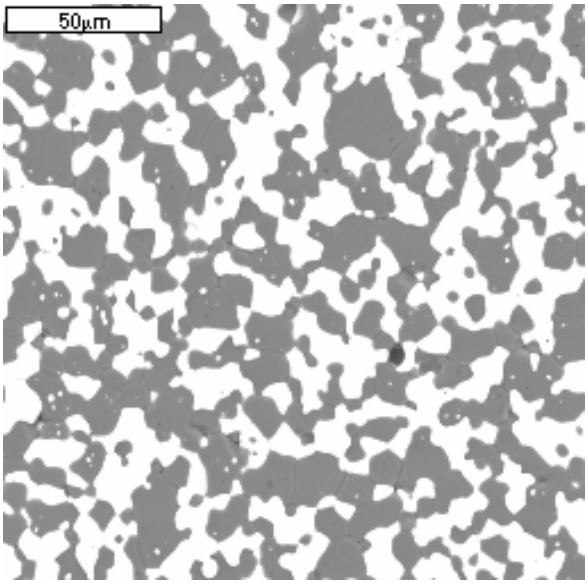

Figure 3.9. SEM image of the 50/50 magnesia-zirconia ceramic.

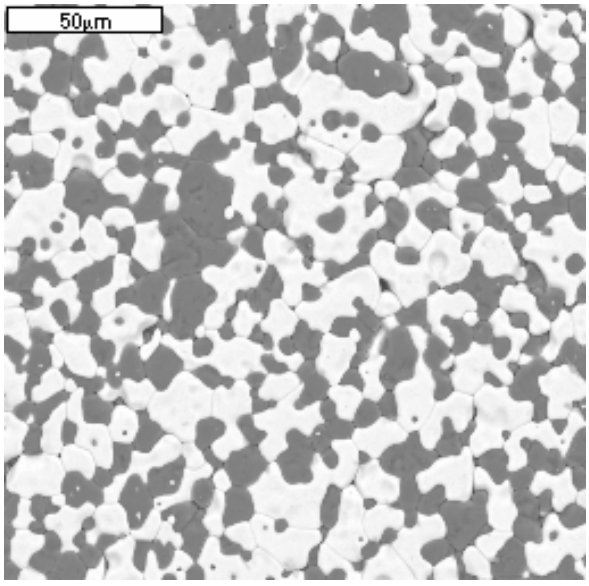

Figure 3.10. SEM image of the 40/60 magnesia-zirconia ceramic.

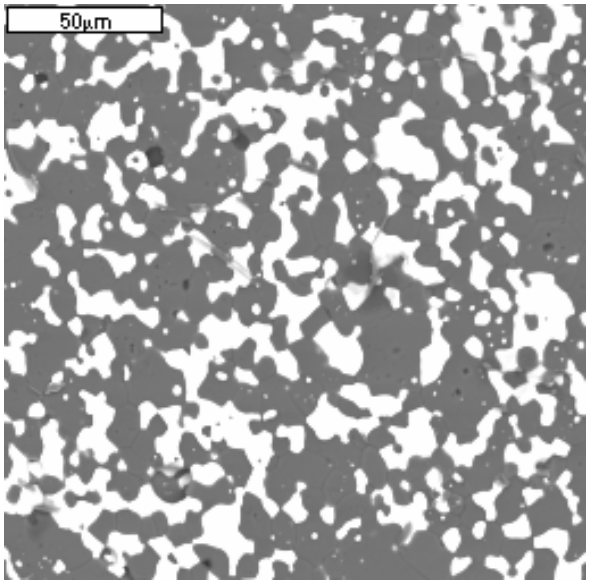

Figure 3.11. SEM image of the 60/40-Er magnesia-zirconia-erbia ceramic.

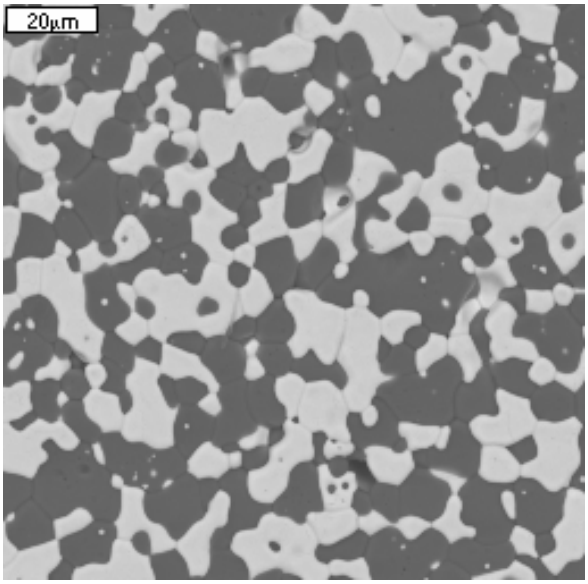

Figure 3.12. SEM image of the 50/50-Er magnesia-zirconia-erbia ceramic.

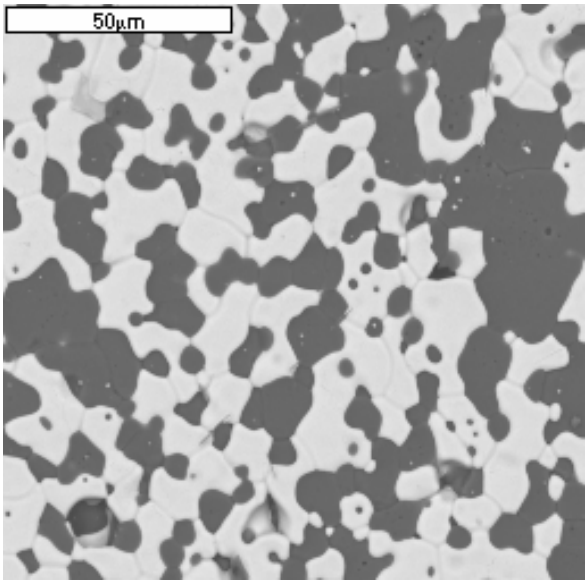

Figure 3.13. SEM image of the 40/60-Er magnesia-zirconia-erbia ceramic.

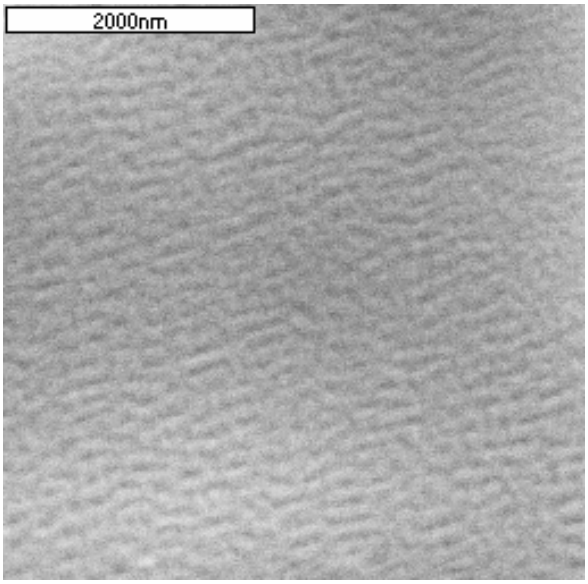

Figure 3.14. Nano-sized substructure on the surface of zirconia grains in the magnesia-zirconia sample.

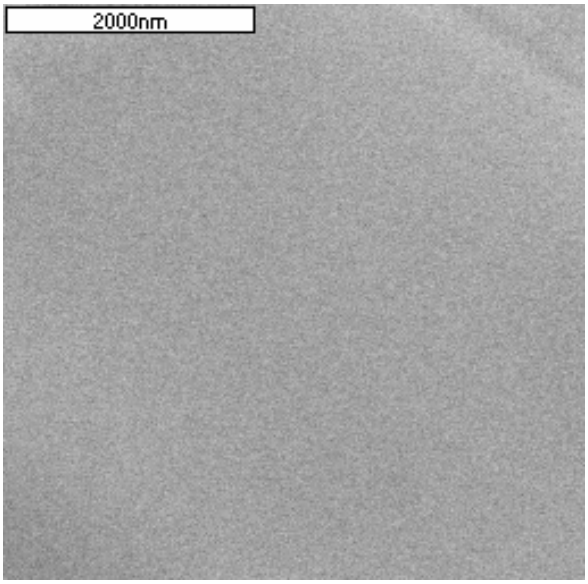

Figure 3.15. Surface of zirconia grain in the erbia-doped magnesia-zirconia sample.

3.3.3.3 High magnification SEM of zirconia grains

High magnification scanning electron microscopy revealed presence of nano-sized substructure on the surface of zirconia grains in the magnesia-zirconia sample (Figure 3.14). This substructure was not detected in the erbia-doped sample (Figure 3.15).

3.3.4 Energy dispersive x-ray analysis

The amount of magnesium present in the magnesia-zirconia solid solution phase was determined by the standardless energy dispersive (EDS) X-ray spectrometry. The analysis of each sample was performed by measuring the concentrations of magnesium and zirconium in 15 locations within the magnesia-zirconia solid solution grains. The resulting ratios between magnesium and zirconium atomic concentrations are shown in Table 3.1. These ratios represent the average of the meaningful measurements. The standard deviation is also included. The Zr/Mg atomic ratios for binary compositions shown in Table 3.1 are in good agreement with the published phase diagram for MgO-ZrO_2. According to the latter, the solubility of MgO in ZrO_2 at 1700^oC is approximately 16% molar, which is equivalent to the Zr/Mg atomic ratio of 5.25.

Using a similar approach, the magnesia phase was analyzed for the presence of zirconium and erbium. The analysis of each sample was performed by measuring the concentrations of magnesium, zirconium and erbium in 5 locations within magnesia grains. No zirconium or erbium was detected in magnesia grains.

Table 3.1. Composition of the magnesia-zirconia solid solution phase.

Sample	Ratio of Zr/Mg atomic concentrations	Composition of the MgO-ZrO_2 solid solution phase
40/60	5.35 ±0.58	$Mg_{0.158}Zr_{0.842}O_{1.842}$
50/50	5.24 ±0.60	$Mg_{0.160}Zr_{0.840}O_{1.840}$
60/40	4.81 ±0.60	$Mg_{0.172}Zr_{0.828}O_{1.828}$
40/60-Er	5.50 ±0.74	$Er_{0.067}Mg_{0.143}Zr_{0.789}O_{1.823}$
50/50-Er	5.78 ±0.82	$Er_{0.082}Mg_{0.135}Zr_{0.783}O_{1.824}$
60/40-Er	5.63 ±0.90	$Er_{0.099}Mg_{0.136}Zr_{0.765}O_{1.815}$

Since the EDS analysis detected no erbium presence in the magnesia phase, the amount of erbium present in zirconia grains was determined from the batched amounts of erbium and zirconium oxides, assuming that all added erbium oxide has completely dissolved in zirconia. The EDS analysis to determine erbium content in the zirconia phase was attempted as well. However, the measured values were higher than expected due to the matrix effects explained by the higher atomic number of erbium as compared to other constituents of the ceramic.

The amount of oxygen shown in Table 3.1 was determined from the known stoichiometry of the metal-to-oxygen ratio of the oxides. The following oxidation states were used: Mg^{2+}, Zr^{4+}, Er^{3+}.

3.3.5 X-ray diffraction analysis

X-ray diffraction analysis of samples was performed on binary and ternary compositions. First, the analysis was carried out on ~1.5 mm thick discs cut from as-sintered pellets. After completion of the analysis, the discs were ground in a mortar and passed through a sieve with an aperture of 45 microns. The resulting powder was re-analyzed. The XRD spectra from sintered and cut monolithic samples were found to be identical to the respective powder patterns, thus it was concluded that no phase transformation was induced by grinding. The XRD results presented herein are for the powdered samples.

Refinement of the XRD patterns was performed with DMS/NT data acquisition and analysis software. Refinement included background and k-alpha-2 stripping, peak-finding, matching library files with the data, peak profile fitting, peak indexing and lattice parameter determination. Phases detected in the analyzed samples are listed in Table 3.2. Superposition of the raw XRD data for the binary compositions is shown in Figure 3.16. It is evident from Table 3.2 and Figure 3.16 that transition from one composition to another does not result in a change of the phase make up of the ceramics. The only difference between the XRD patterns is in the relative peak intensity, which is caused by the difference in relative amounts of magnesia and zirconia phases. This implies that any possible compositional property dependence in these ceramics will be driven solely by the ratio between the cubic zirconia and cubic magnesia phases, not by a phase transformation. These observations and conclusions also apply to the ternary compositions. Superposition of the raw XRD data for the ternary compositions is shown in Figure 3.17.

Table 3.2. Phases identified by X-ray diffraction analysis.

Sample	Identified phases			Lattice parameter, Angstrom	
	ZrO_2-cubic	ZrO_2-monoclinic	MgO-cubic	ZrO_2 cubic phase	MgO phase
40/60	yes	trace	yes	5.0782	4.2100
50/50	yes	trace	yes	5.0782	4.2089
60/40	yes	trace	yes	5.0763	4.2103
40/60-Er	yes	no	yes	5.1042	4.2112
50/50-Er	yes	no	yes	5.0999	4.2102
60/40-Er	yes	no	yes	5.0969	4.2100

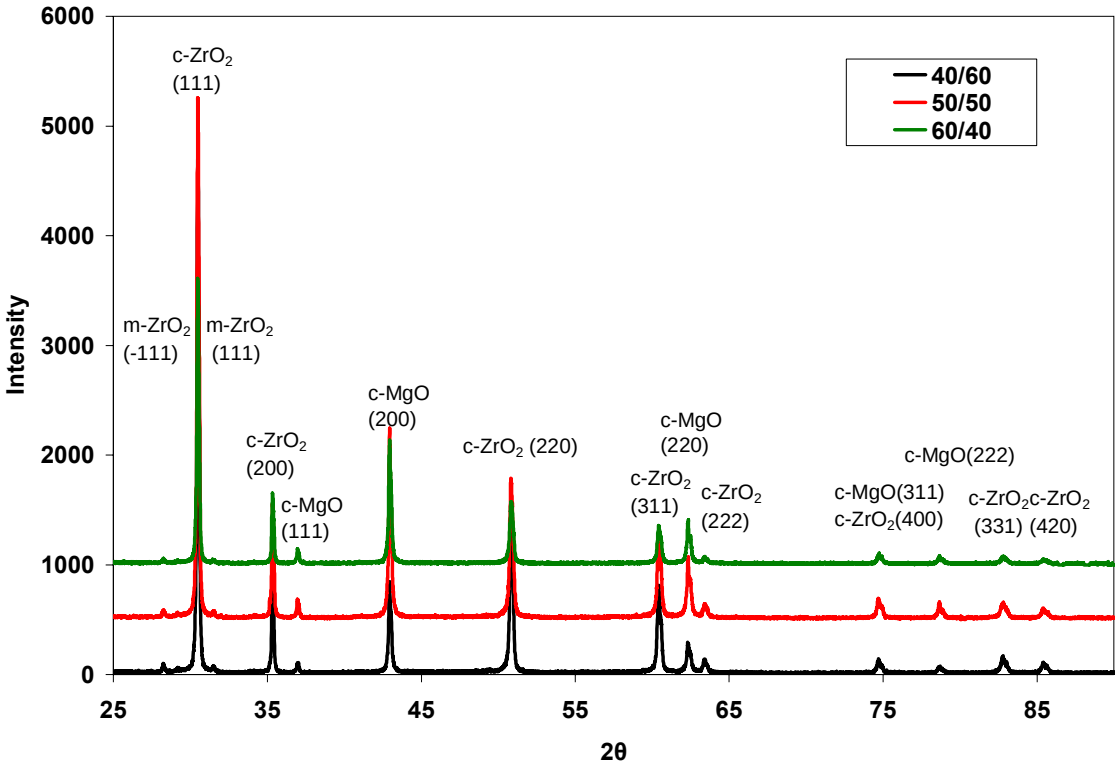

Figure 3.16. Superposition of the raw XRD data for the binary compositions.

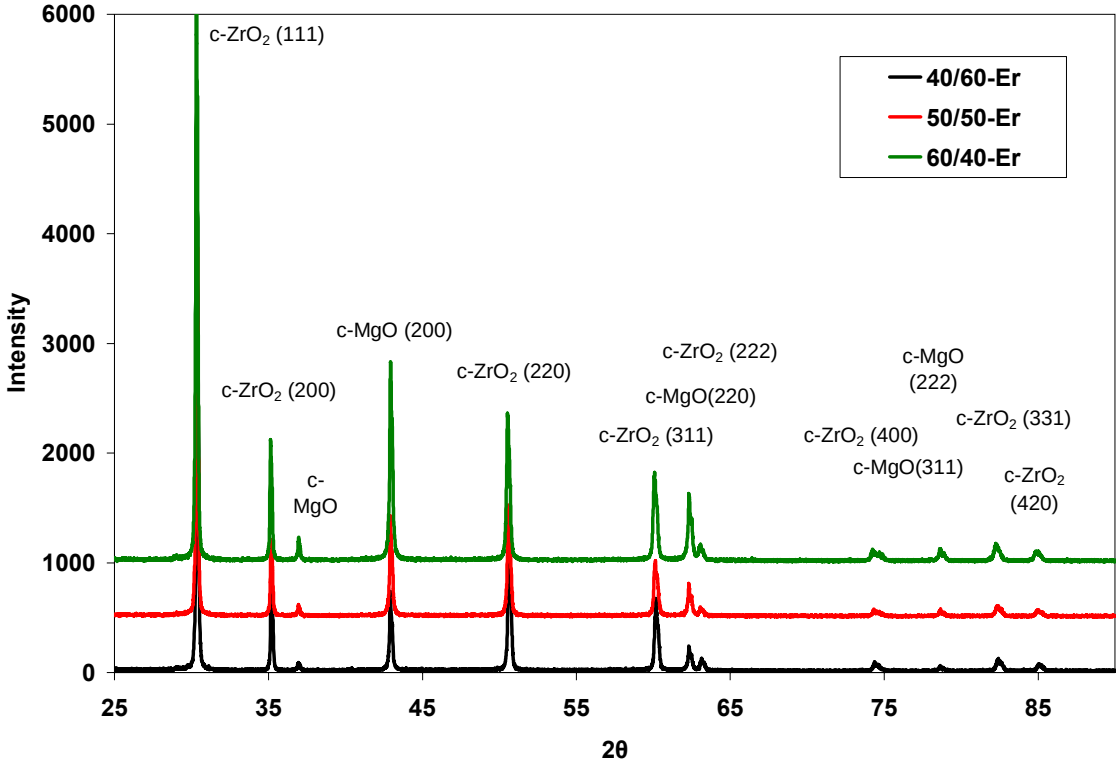

Figure 3.17. Superposition of the raw XRD data for the ternary compositions.

Results of the XRD analysis relative to the behavior of erbia dopant in the magnesia-zirconia system were consistent with the EDS findings discussed in Section 3.3.3.3. Because no erbium-containing phases were detected by XRD, erbia had to have dissolved in either magnesia or zirconia phases. Since the pattern from magnesia phase matched very well the corresponding library pattern, and the magnesia lattice parameter matched the corresponding library value (4.2112 Angstrom), the magnesia phase can be considered practically pure. On the other hand, the zirconia pattern exhibited a notable peak shift to the left, when Er was added to the system (Figure 3.18). The shift was explained by the expansion of the zirconia unit cells caused by substitution of zirconium ions with larger erbium ions. Furthermore, the trace amounts of monoclinic zirconia present in binary magnesia-zirconia compositions were not detected in the erbia doped samples, likely due to stabilization of zirconia by erbia. Based on these observations it was concluded that erbia has fully dissolved in the zirconia phase and formed a ternary erbia-magnesia-zirconia solid solution.

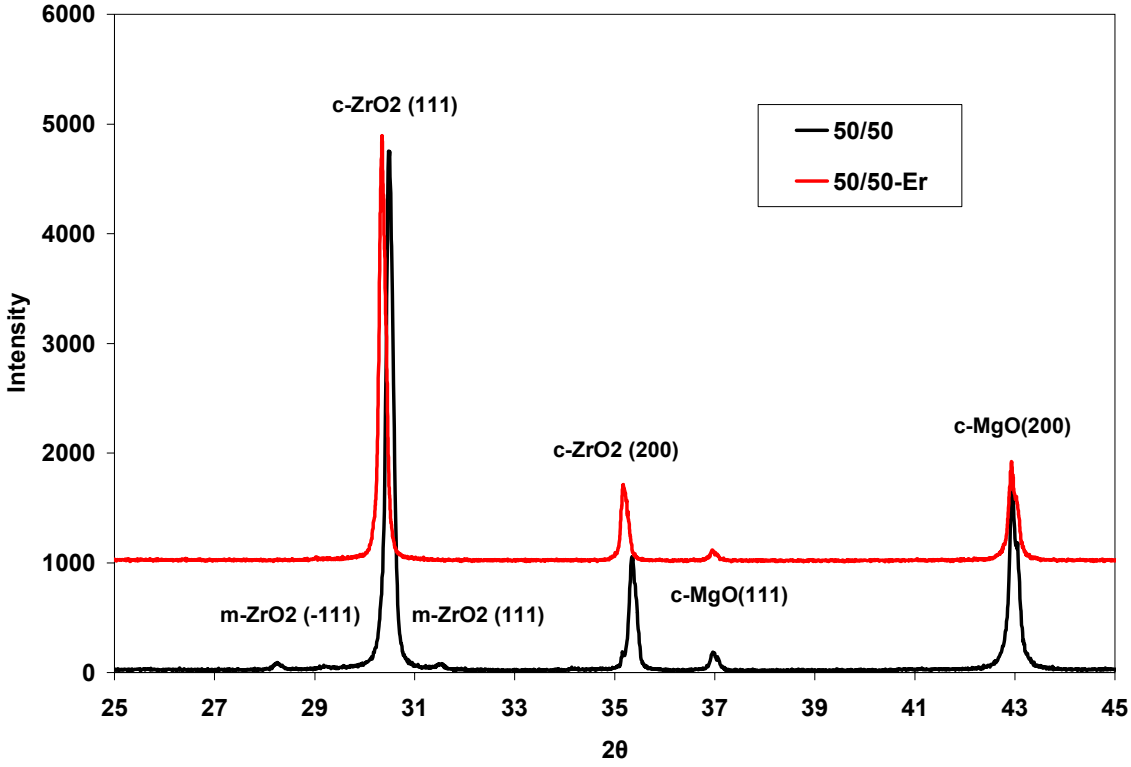

Figure 3.18. Shift of the zirconia phase reflections believed to be caused by forming a ternary erbia-magnesia-zirconia solid solution.

3.3.6 Lattice parameter modeling

To cross-check the EDS and XRD results, the values of the lattice parameter of the zirconia-based solid solutions were calculated from the EDS results and compared with those measured by XRD. Methodology, originally developed by Kim [100], was used to calculate the lattice parameter of magnesia-zirconia, and erbia-magnesia-zirconia solid solutions. Derived from regression analysis of experimental data, this methodology is applicable to solid solutions based on a fluorite-structured oxide. It relies on an empirical relationship between the lattice parameter of such solid solution and the ionic radii, valence, and concentration of the dopant species.

According to Kim [100] the lattice parameter of a zirconia-based solid solution can be expressed as follows:

$$a = 0.5120 + \sum_k (0.0212\Delta r_k + 0.00023\Delta z_k) m_k \qquad (3.1)$$

where

a lattice parameter of the zirconia-based solid solution in nanometers;

Δr_k difference in ionic radius $(r_k - r_h)$ of the kth dopant (r_k) and the host cation (r_h) in the eightfold coordination from Shannon's compilation [101] in nanometers;

Δz_k difference in valence $(z_k - z_h)$ of the kth dopant (z_k) and the host cation (z_h);

m_k mole percent of the kth dopant in the form of MO_x (i.e., if Y_2O_3 is a dopant, its mole percent should be estimated using the $YO_{1.5}$ formula rather than Y_2O_3).

The lattice parameters calculated using the above methodology for the binary and ternary compositions are shown in Table 3.3. The ionic radii used for Er^{3+}, Mg^{2+}, and

Zr^{4+} are 0.1004 nm, 0.089 nm, and 0.084 nm respectively [101]. The ionic radii correspond to the eightfold coordination. The values of the lattice parameters obtained from the XRD analysis are included for comparison.

The calculated values of the lattice parameter are in a good agreement with the values measured by XRD. Figure 3.19 shows experimentally determined values of the lattice parameter versus values calculated using Kim's methodology. To further support the validity of the methodology relative to the compositions of interest, the lattice parameter calculation was performed for several magnesia-zirconia and erbia-zirconia compositions whose lattice parameters are available in the literature [102, 103, 104] and in the powder diffraction file (PDF) [105]. These results are included in Figure 3.19. In Figure 3.19 the diagonal represents the perfect agreement between the calculated and the measured value. The dashed lines represent 0.5% deviation. Evidently, the accuracy of the model is at least 0.5% for all but one data point.

Both the calculation and the measurement agree in predicting a decrease of the lattice parameter with an increase of magnesia content in binary compositions, and an increase of the lattice parameter with an increase of erbia content in the ternary compositions. To illustrate this agreement related to the binary compositions, experimentally determined lattice parameters are presented as a function of magnesia content in Figure 3.20. Published experimental values are included for comparison. Table 3.4 and Table 3.5 provide a summary of published experimental data used for constructing Figure 3.19 and Figure 3.20. The values of lattice parameter, calculated using the methodology described above, are also included.

Table 3.3. Lattice parameters calculated and measured for cubic zirconia doped with magnesia and erbia

Sample	Solid solution composition as determined by EDS	m_k, mole percent of the kth dopant		a calculated, nm	a measured, nm	$(a_{calc}-a_{meas})/a_{meas}$
		m_{Mg}	m_{Er}			
40/60	$Mg_{0.158}Zr_{0.842}O_{1.842}$	15.8	0	0.50641	0.50782	-0.0028
50/50	$Mg_{0.160}Zr_{0.840}O_{1.840}$	16.0	0	0.50634	0.50782	-0.0029
60/40	$Mg_{0.172}Zr_{0.828}O_{1.828}$	17.2	0	0.50591	0.50763	-0.0034
40/60-Er	$Er_{0.067}Mg_{0.143}Zr_{0.789}O_{1.823}$	14.3	6.7	0.50771	0.50969	-0.0039
50/50-Er	$Er_{0.082}Mg_{0.135}Zr_{0.783}O_{1.824}$	13.5	8.2	0.50816	0.50999	-0.0036
60/40-Er	$Er_{0.099}Mg_{0.136}Zr_{0.765}O_{1.815}$	13.6	9.9	0.50835	0.51042	-0.0041

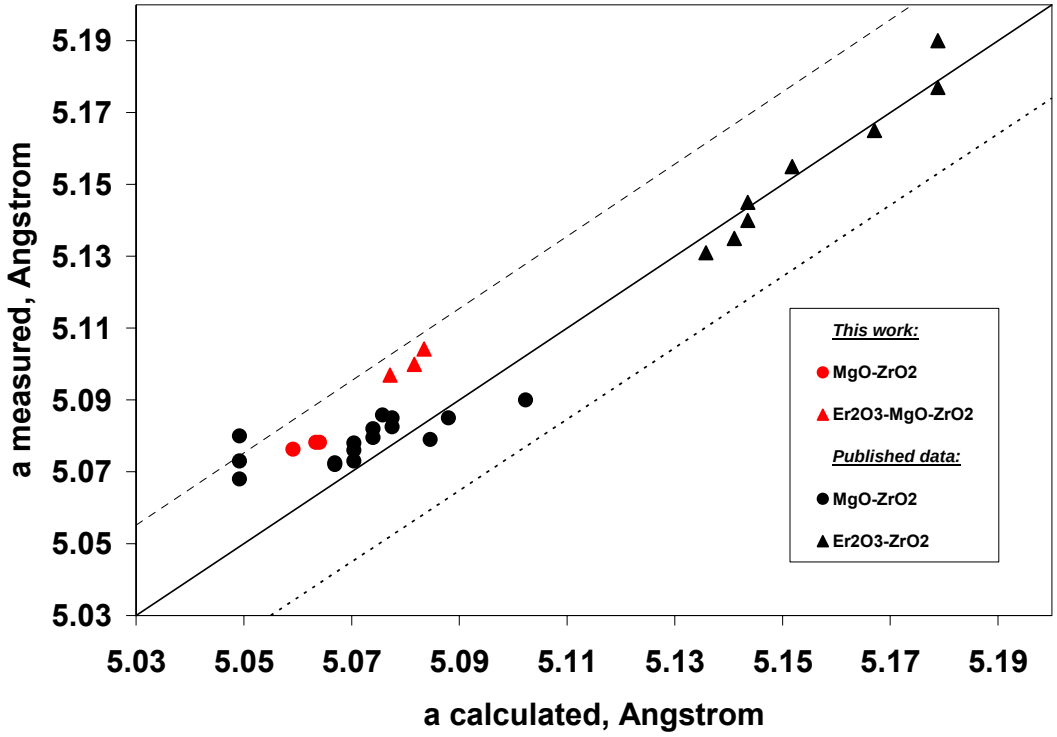

Figure 3.19. Measured versus calculated lattice parameter.

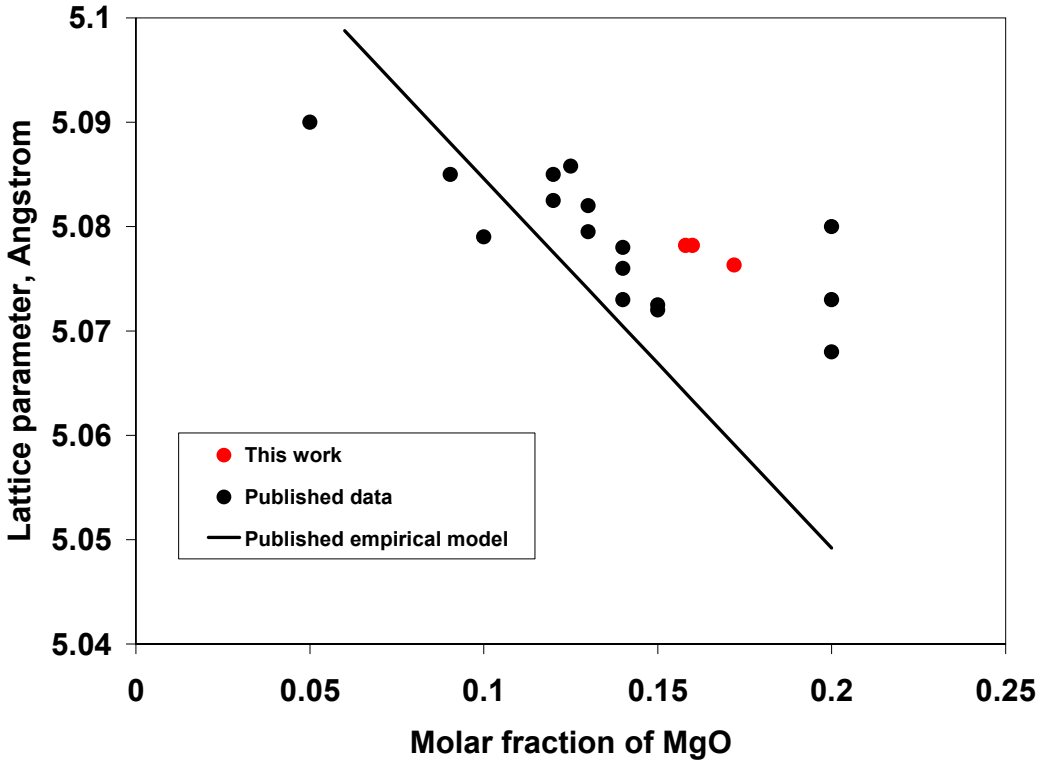

Figure 3.20. Lattice parameter of the magnesia-zirconia solid solution as a function of magnesia content.

Table 3.4. Published and calculated lattice parameter data for magnesia-zirconia solid solutions.

MgO mole fraction	Reported lattice parameter, Å	Calculated lattice parameter, Å	Reference
0.12	5.0825	5.0775	Yin and Argent [104]
0.13	5.0795	5.0740	
0.14	5.076	5.0704	
0.15	5.0725	5.0669	
0.2	5.068	5.0492	Saiki et al. [103]
0.1	5.079	5.0846	
0.05	5.09	5.1023	
0.12	5.085	5.0775	Sim and Stubican [102]
0.13	5.082	5.0740	
0.14	5.078	5.0704	
0.15	5.072	5.0669	
0.0904	5.085	5.0880	PDF 78-1809 [105]
0.2	5.073	5.0492	PDF 77-2156 [105]
0.2	5.08	5.0492	PDF 75-0345 [105]
0.125	5.0858	5.0758	PDF 78-1810 [105]
0.14	5.073	5.0704	PDF 80-0964 [105]

Table 3.5. Published and calculated lattice parameter data for erbia-zirconia solid solutions.

$ErO_{1.5}$ mole fraction	Reported lattice parameter, Å	Calculated lattice parameter, Å	Reference
0.2	5.145	5.1435	PDF 78-1307 [105]
0.5	5.190	5.1788	PDF 78-1299 [105]
0.134	5.131	5.1358	Stewart and Hunter [106]
0.179	5.135	5.1411	
0.2	5.140	5.1435	
0.27	5.155	5.1518	
0.4	5.165	5.1671	
0.5	5.177	5.1788	

3.3.7 Density

Results of the density measurements are shown in Table 3.6. The theoretical density of the composites was calculated from the theoretical densities of the constituent phases: magnesia and zirconia-based solid solution. The theoretical density of magnesia is known to be 3.58 g/cm^3. The theoretical density of the zirconia-based solid solutions was calculated from their crystallographic unit cell weight and volume. The crystallographic unit cell weight was determined from the stoichiometry of the solid solutions, and the unit cell weight was determined from the lattice parameter measured by XRD. The resulting theoretical density values of the zirconia-based solid solutions are given in Table 3.7. The relative amount of the phases in the composites was determined from the mass balance.

The theoretical density values of the magnesia-zirconia solid solutions agree well with the published data (Figure 3.21). The published data is from the Powder Diffraction File [105] cards 78-1809, 77-2156, 75-0345, 78-1810, and 80-0964. Comparison with the published data was not possible for the ternary solid solutions, since no such data is available.

Table 3.6. Results of the density measurements.

Sample	Density, g/cm3			
	Green	Pycnometric	Immersion	Theoretical
40/60	2.68	4.61	4.61	4.63
50/50	2.45	4.40	4.39	4.41
60/40	2.25	4.18	4.19	4.20
40/60-Er	2.78	4.81	4.76	4.79
50/50-Er	2.55	4.56	4.54	4.58
60/40-Er	2.40	4.35	4.33	4.38
MgO	1.84	3.57	3.45	3.58

Table 3.7. Theoretical density values of the zirconia-based solid solutions.

Solid solution composition	Theoretical density, g/cm^3
$Mg_{0.158}Zr_{0.842}O_{1.842}$	5.56
$Mg_{0.160}Zr_{0.840}O_{1.840}$	5.55
$Mg_{0.172}Zr_{0.828}O_{1.828}$	5.51
$Er_{0.067}Mg_{0.143}Zr_{0.789}O_{1.823}$	5.78
$Er_{0.082}Mg_{0.135}Zr_{0.783}O_{1.824}$	5.87
$Er_{0.099}Mg_{0.136}Zr_{0.765}O_{1.815}$	5.95

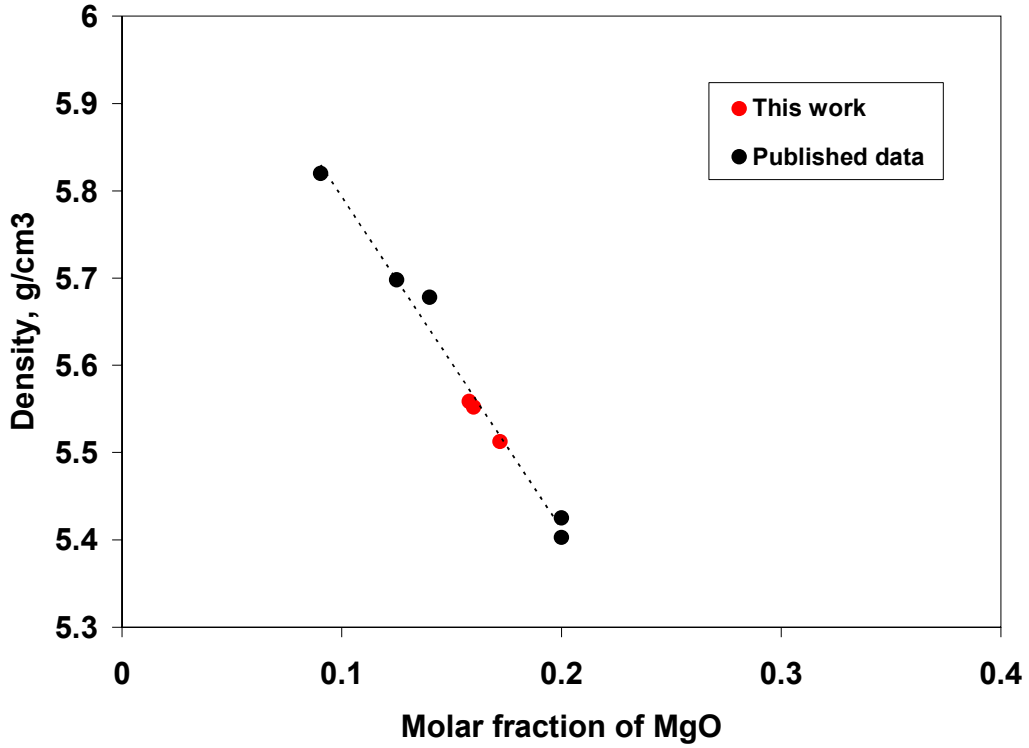

Figure 3.21. Density of the magnesia-zirconia solid solutions.

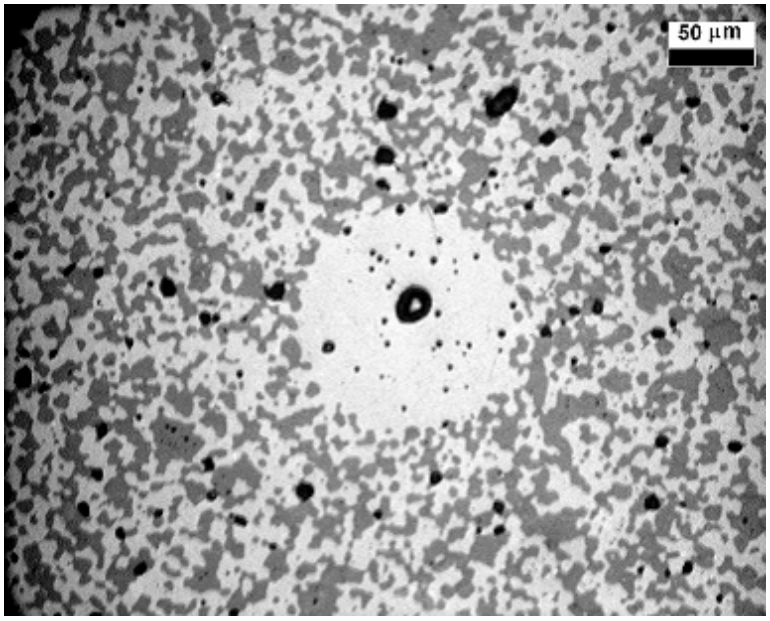

a)

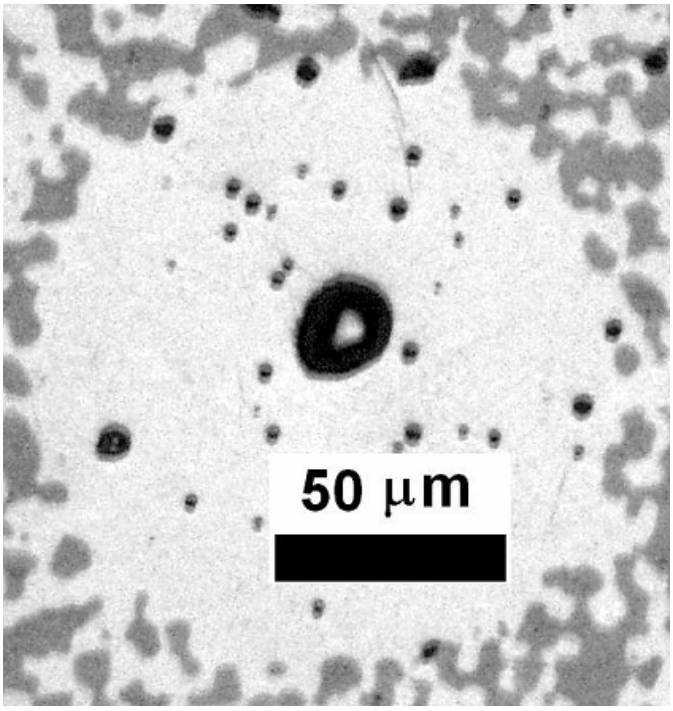

b)

Figure 3.22. Optical micrographs of the ceramic containing microspheres.

3.4 SIMULATION OF DISPERSION-TYPE FUEL FABRICATION

To imitate fabrication of the dispersed fuel, 0.1mm diameter zirconia microspheres simulating fissile inclusions were added prior to sintering to the ceramic compositions under investigation. The microspheres (lot 1000168) were obtained from Tosoh Corporation (Tokyo, Japan). The purpose of this experiment was to demonstrate that the microspheres can be sintered into the ceramic, and a high-quality crack-free product can be obtained.

Optical micrographs of the ceramic containing the microspheres are shown in Figure 3.22. The images reveal that the microspheres are fully integrated into the surrounding matrix. Absence of cracks is an evidence of good thermal and mechanical compatibility between of the microsphere and the ceramic.

3.5 SUMMARY

Binary magnesia-zirconia ceramics containing 40, 50, and 60 wt% of magnesia, and magnesia-zirconia ceramics doped with 7 wt% of erbia were fabricated using conventional pressing and sintering techniques consistent with those currently used in LWR fuel manufacture. The densities of the final product were near theoretical. The microstructural characterization established, that regardless of the composition and regardless of erbia doping, the final product consists of two phases: cubic zirconia-based solid solution, and cubic magnesia. In each case, the composition of the zirconia-based solid solution phase was determined by EDS. The EDS results were verified by

demonstrating a good agreement between the lattice parameter values calculated from the solid solution compositions with the lattice parameter values measured by XRD; and between the solid solution theoretical densities calculated from the solid solution compositions and published theoretical density values.

CHAPTER IV

ASSESSMENT OF KEY FEASIBILITY ISSUES

This chapter is intended to provide the evidence that the magnesia-based ceramic with improved hydration resistance developed in this study is a feasible IMF matrix for use in a LWR. The feasibility assessment is limited to the experimental investigation of long-term effects of hydrothermal exposure, and to the measurement of thermal transport properties to predict fuel operating temperature.

4.1 INVESTIGATION OF HYDRATION RESISTANCE

4.1.1 Experimental procedure

The purpose of hydration testing was three-fold: to assess the mass loss of the magnesia-zirconia ceramics in hydrothermal conditions, to determine the effect of the zirconia content on the mass loss, and to investigate the mechanism behind improved hydration resistance. The particulars of hydration tests are as follows. As-sintered ceramic pellets were exposed to static de-ionized water at 300^{o}C for the periods of up to 30 days. The tests were performed in a commercial 316 stainless steel two-liter pressure vessel (model 4622, Parr Instrument Company, Moline, Illinois), rated for operation at a maximum pressure of 1900 psi at 350°C. The pressure vessel was equipped with a pressure relief valve set at 1700 psi, a 2100 psi rupture disk, a pressure gauge, an inlet/outlet valve, a heating mantle, and a temperature controller with two

thermocouples. During the operation the thermocouples resided in a specially designed thermowell protruding into the reaction volume.

As-sintered ceramic pellets were placed into the pressure vessel filled with one liter of de-ionized water. The vessel was closed, positioned in the heating mantle and the thermocouples were inserted into the thermowell. The temperature controller was set at 300°C. A heating time of one hour was required for the water temperature to reach this setting. After that the test continued without further operator intervention until the desired exposure time was attained.

Periodically, the heat to the pressure vessel was shut off, the vessel was allowed to cool, and samples were removed, rinsed with de-ionized water, visually inspected, dried for 5 hours at 80^{o}C, and weighed. Some samples were photographed, analyzed by optical microscopy (Trinocular Stereoscopic Zoom Microscope Nikon SMZ-2T), SEM (Zeiss DSM960A), EDS (Oxford Instruments, Freemont, CA), and XRD (Scintag X1). After the samples were placed back into the vessel, the vessel was refilled with fresh water and the test was resumed. The typical frequency of such shut-downs was once every 5 days.

The tests were intended to simulate the exposure of an IMF pellet to the reactor coolant in an event of a fuel pin failure and consequent ingress of reactor coolant into the failed fuel pin. It is recognized that an ideal simulation of such event would involve a dynamic test where the water is allowed to flow through the test volume. However, the water solubility of the phases comprising the ceramic under investigation is minimal, and the degradation mechanism is not driven by dissolution, but by hydration of

magnesia. Thus, it was concluded that no "poisoning" of water would occur during long-term hydration tests. Here the term "poisoning" implies saturation of water by dissolved species turning the water non-reactive towards the ceramic. Due to these considerations, the static tests were chosen as a low cost and robust alternative to the dynamic tests. For the same reasons, the tests were performed on multiple samples simultaneously, rather then on one sample per run. A test-to-test consistency of the ratio of the sample surface area to the liquid volume, normally required in situation when sample dissolution is present, was unnecessary here. A typical surface area to the liquid volume ratio in these tests was up to 3 m^{-1}. This involves testing up to six ceramic pellets per run, with each pellet having a surface area of 0.5 cm^2 in an autoclave filled with one liter of water.

4.1.2 Results and discussion

4.1.2.1 Effect of zirconia content on the mass loss due to hydration

As mentioned earlier, the pellet mass loss was used as a quantitative indicator of the extent of hydration. The Normalized Mass Loss (NML) was determined from measured mass loss according to the following equation:

$$NML(t) = \frac{m_i - m(t)}{A_i} \tag{4.1}$$

where,

m_i – sample mass before the exposure, grams

$m(t)$ – sample mass after the exposure at time t, grams

A_i – initial sample surface area, cm^2.

The plot of NML versus the elapsed time in hours observed at the temperature of 300^oC is shown in Figure 4.1. The plot represents the tests conducted for three samples of each composition, except the 30/70 composition for which only two samples were tested. The data points on the plot represent the mass loss measured during periodic shut-downs.

The plot (Figure 4.1) shows good reproducibility of the NML between different samples of the same compositions. The data scatter observed here is due to occasional chipping of the pellets during tests. The chipping was likely caused by inhomogeneity of the samples and possibly by contamination of the surface layers of the pellets by the furnace insulation debris during sintering.

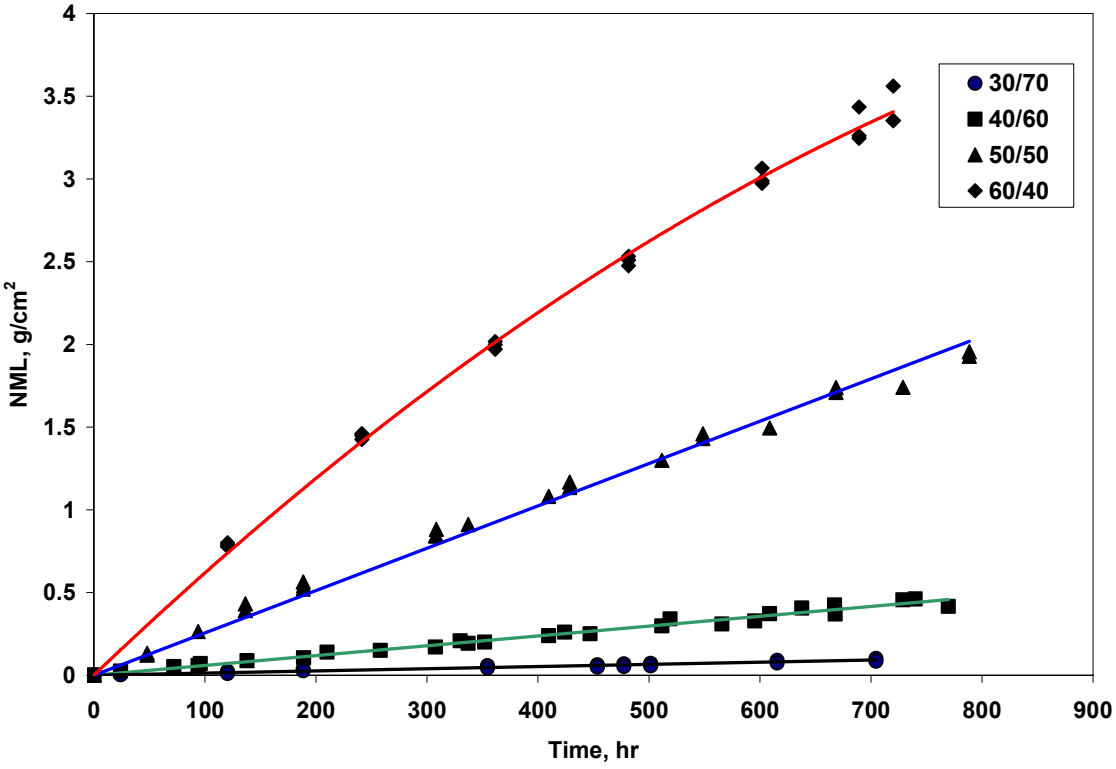

Figure 4.1. Normalized ceramic mass loss due to hydration versus the elapsed time.

The time dependence of the mass loss appears linear for the 30/70, 40/60, and 50/50 compositions and parabolic for the 60/40 composition. The decrease with time of the hydration rate observed for the 60/40 composition is due to the decrease of the surface area of the pellets. The mass loss for the ceramics of this composition is sufficient to cause the decrease of the surface area at higher exposure times. This was confirmed by monitoring the relative surface area of the 60/40 composition during the exposure. The time dependence of the relative surface area is shown in Figure 4.2. The dependence shown in Figure 4.2 is clearly linear with a slope of -0.000453. Thus, for this composition the time dependence of the surface area can be expressed as follows:

$$A(t) = A_i(1 - 0.000453t) \tag{4.2}$$

where A_i initial sample surface area.

Knowing the time dependence of the pellet surface area, the NML for the 60/40 composition can be recalculated to account for the decrease of the surface area:

$$NML_{60/40} = \frac{m_i - m(t)}{A_i(1 - 0.000453t)} \tag{4.3}$$

The NML for the 60/40 composition corrected for the surface area decrease is plotted in Figure 4.3. Evidently, the dependence becomes linear after the correction is applied.

Therefore, it can be concluded that samples of all compositions exhibited the mass losses that increase linearly with the exposure time.

The normalized mass loss rate (NMLR) can be readily determined from the slope of the curves in Figure 4.1 and Figure 4.3. The NMLR is shown in Figure 4.4 as a

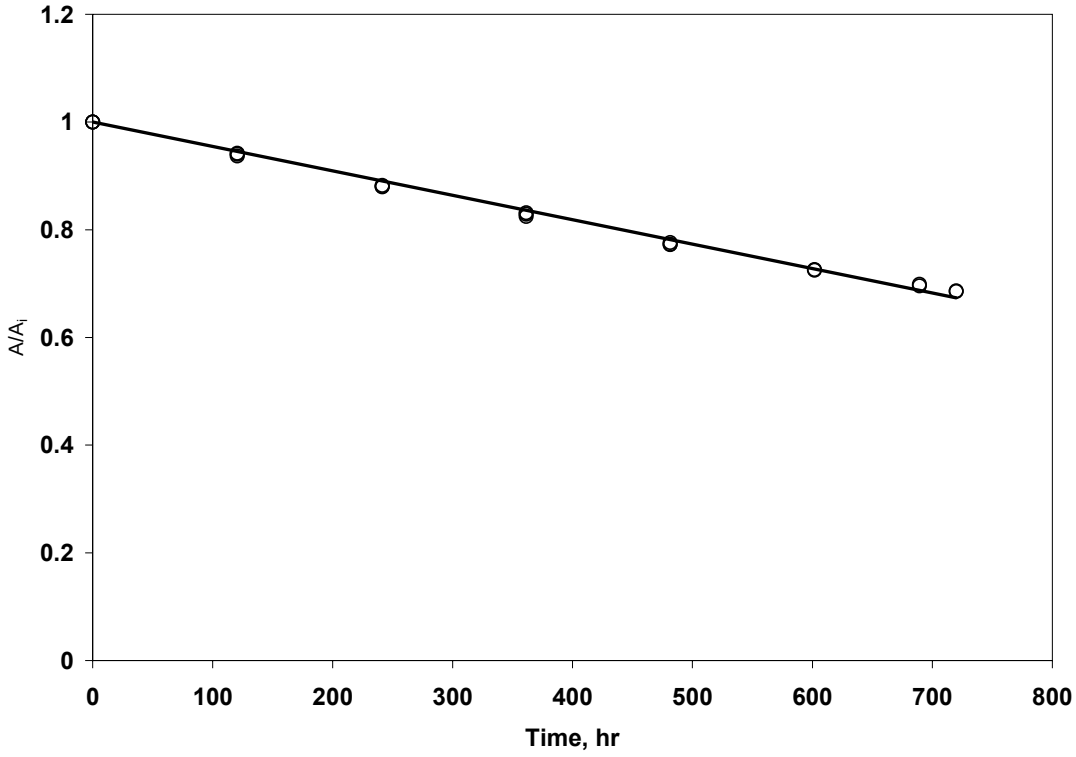

Figure 4.2. The decrease of the pellet surface area for the 60/40 composition.

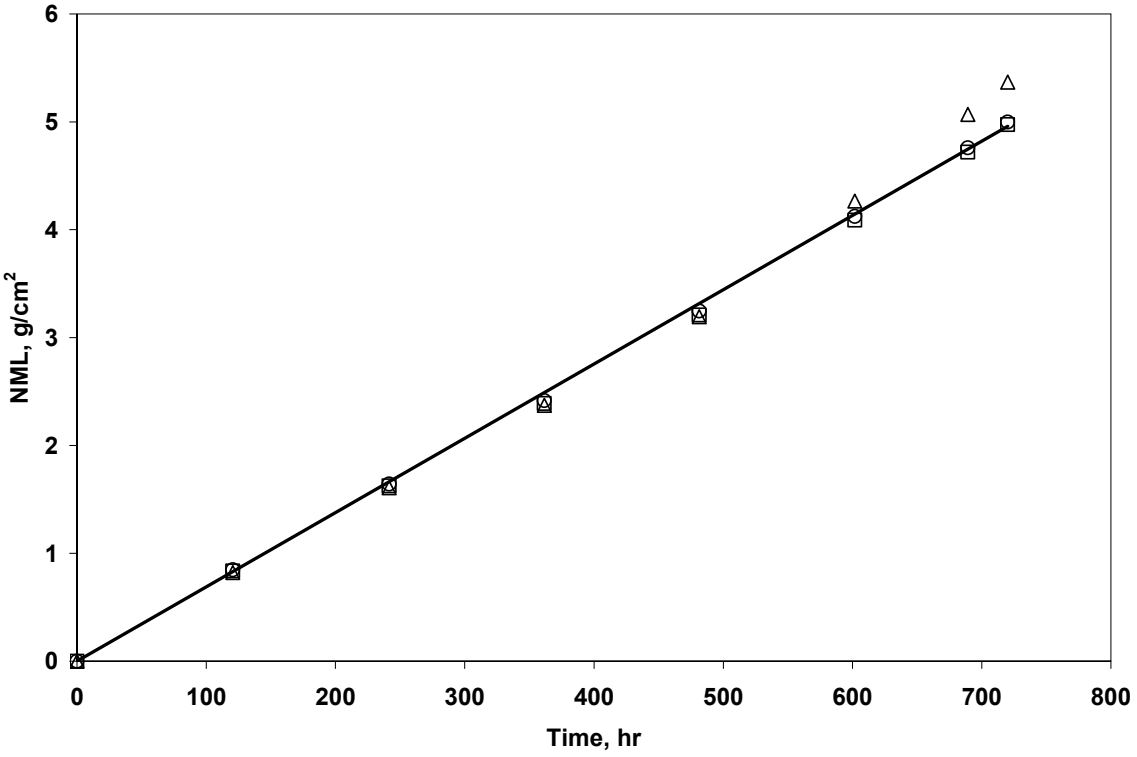

Figure 4.3. Normalized ceramic mass loss for the 60/40 composition corrected for the surface area decrease.

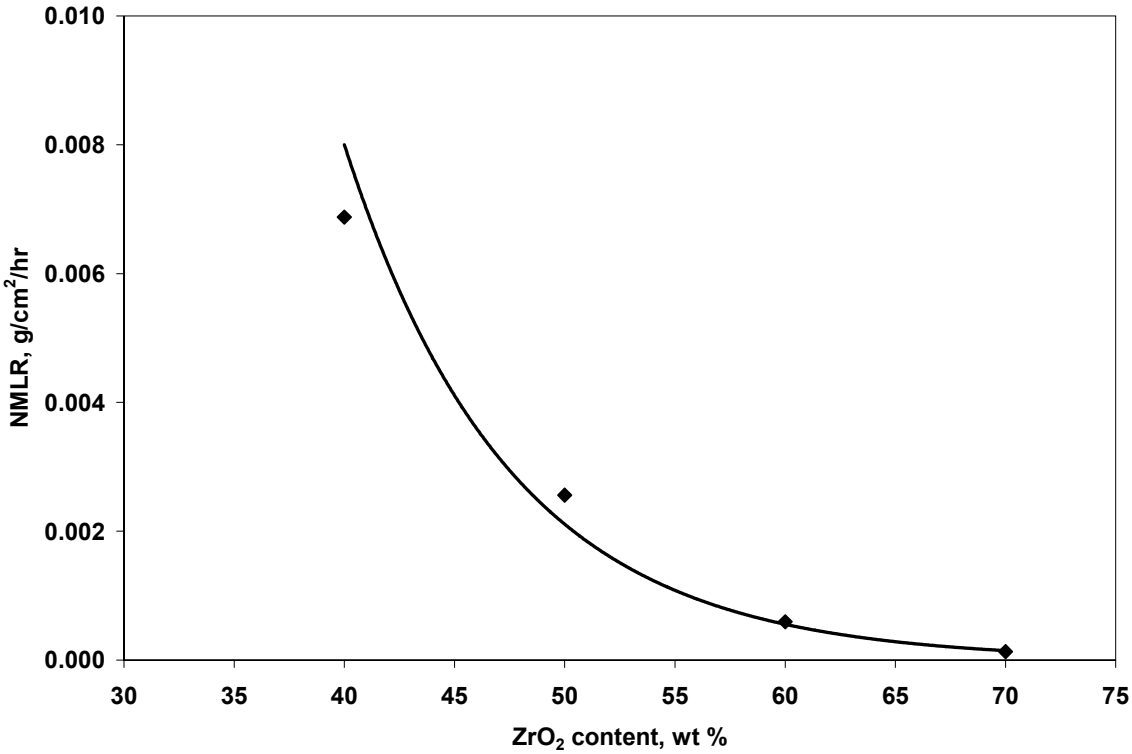

Figure 4.4. Normalized mass loss rate as a function of zirconia content.

function of zirconia content. The Arrhenius-type trendline in Figure 4.4 follows the equation:

$$\text{NMLR} = 1.6569\exp(-\frac{2c_{Zr}}{15}) \quad (4.4)$$

where, *NMRL* is the normalized mass loss rate in grams per square centimeter of the ceramic surface per hour, and c_{Zr} is zirconia content in weight percent.

4.1.2.2 Observation of the hydrated microstructures and hydration mechanism

Photographs of magnesia-zirconia ceramics after exposure to water at 300^{o}C for 720 hours are shown in Figure 4.5. As evident from Figure 4.5, the integrity of the pellets is preserved. However, some roughness is obvious in both pellets as well as chipping in the case of the erbia-doped sample. Nevertheless, these images establish a remarkable contrast with Figure 3.1, in which severe hydration-induced degradation of pure magnesia ceramics is illustrated.

To understand the mechanism behind the improved hydration resistance in magnesia-zirconia ceramics, several hydrated pellets were examined by SEM and XRD. SEM was conducted with an objective to locate the hydration product, and to determine the extent of degradation on the microscopic scale. XRD was performed to identify the crystallographic phases present in the hydrated samples.

An SEM image of a magnesia-zirconia ceramic surface after exposure to the de-ionized water at 300^{o}C for 700 hours is shown in Figure 4.6. The bright phase shown in Figure 4.6 is a magnesia-zirconia solid solution. The dark phase contains both MgO and

$Mg(OH)_2$. This phase was analyzed by conducting point-by point EDS to determine the atomic ratio between magnesium and oxygen. EDS revealed that the dark phase contained approximately 1.5 oxygen atoms per 1 magnesium atom. Because MgO contains 1 oxygen atom per 1 magnesium atom, and $Mg(OH)_2$ contains 2 oxygen atoms per 1 magnesium atom, the dark phase observed in Figure 4.6 is likely MgO with the hydration product $Mg(OH)_2$ deposited on its surface. Because the penetration depth of the electron probe has exceeded the thickness of the $Mg(OH)_2$ layer, the resulting EDS spectrum represents a sum of the spectra produced by the surface $Mg(OH)_2$ layer and the underlying MgO layer.

To evaluate the extent of hydration in relation to the volume of the ceramic pellet rather than its surface, a pellet, previously exposed to the de-ionized water at 300^{o}C for 700 hours, was cut with a high speed diamond saw, polished and thermally etched. The pellet's cross-section was then examined by SEM. The results of this examination are shown in Figure 4.7. Incomplete and missing MgO grains present on the pellet's edge were interpreted as the signs of a hydration attack. The arrows on Figure 4.7 point to such sites. As evident from Figure 4.7, only magnesia grains located on the surface of the pellet and supposedly exposed to the water show signs of degradation. Other grains appear intact. Thorough examination of the remainder of the cross-section was unable to detect any hydration damage beyond the surface layer of the grains.

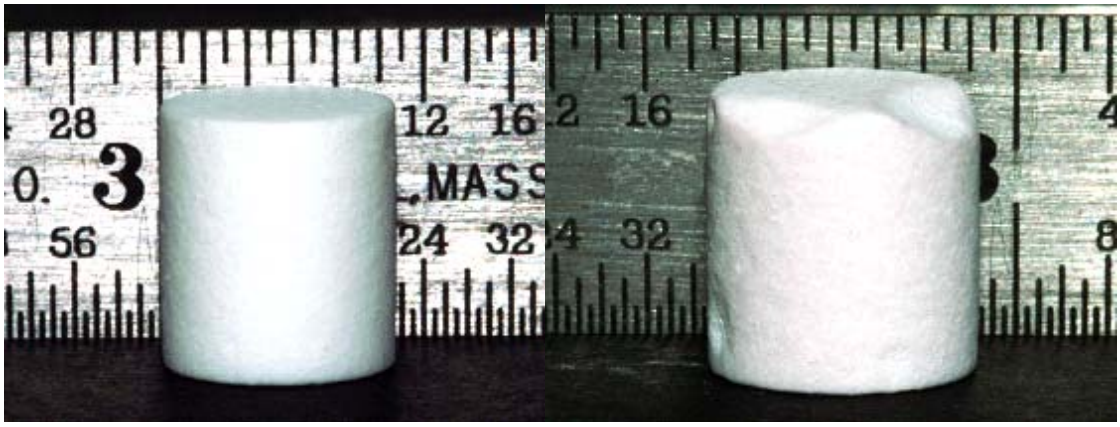

Figure 4.5. Magnesia-zirconia (60/40) ceramic (left) and magnesia-zirconia ceramic doped with erbia (50/50-Er) (right) after 720 hours of exposure to the water at 300^{o}C.

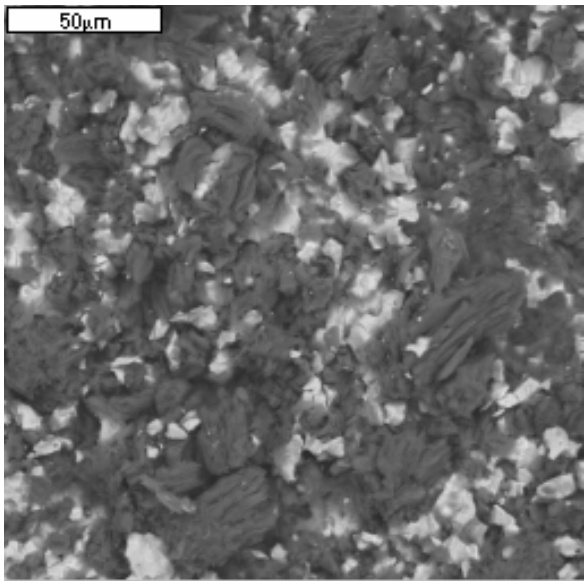

Figure 4.6. Surface of the 50/50 ceramic after 700 hr exposure to water at 300°C White phase: ZrO_2-MgO(ss); grey phase: $Mg(OH)_2$+MgO.

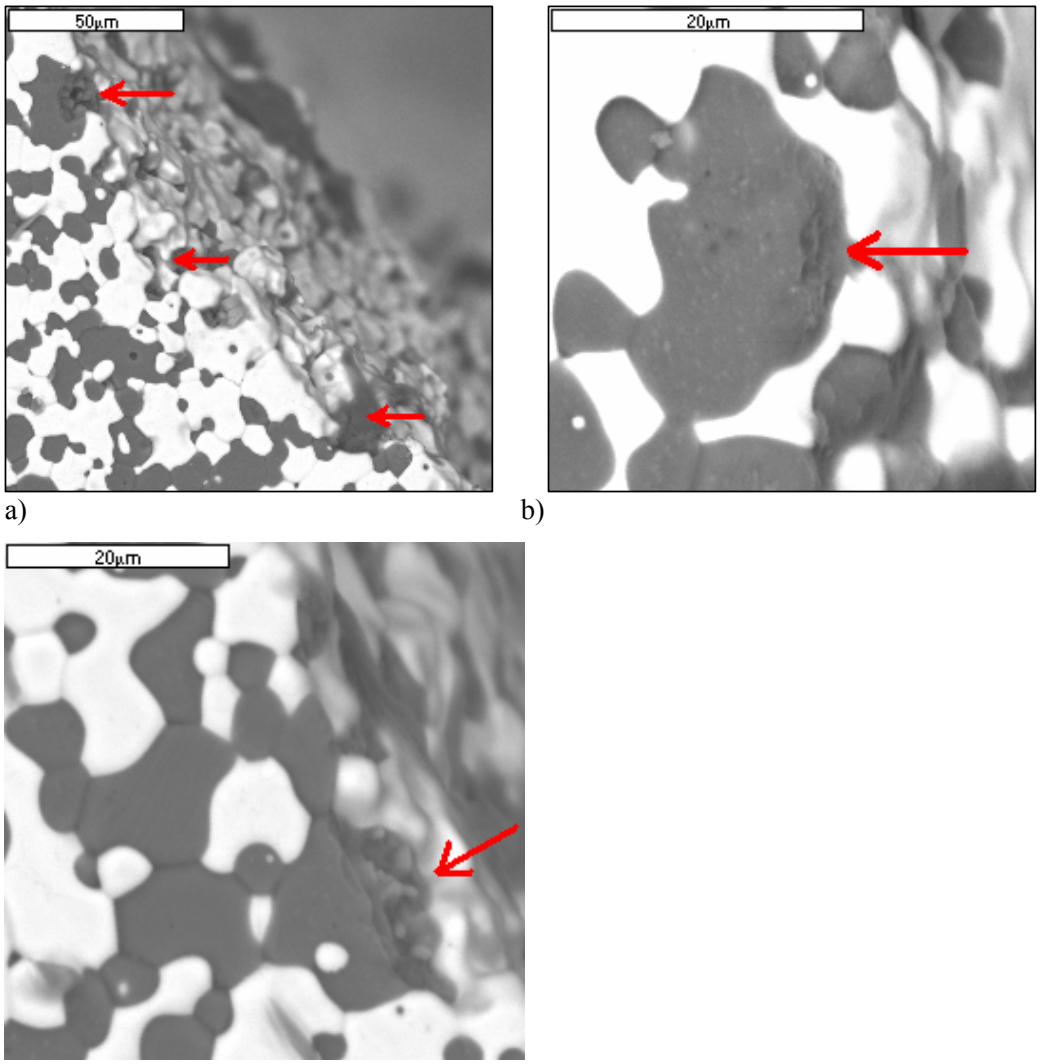

a) b)

c)

Figure 4.7. The edge of polished and thermally etched cross-section of the 40/60 ceramic after 700 hr exposure to water at 300°C.

Earlier it was shown that in the case of pure magnesia ceramics the degradation quickly propagates inside the sample due to the hydration induced cracking that provides pathways for the water. Therefore, absence of hydration-induced cracks in magnesia-zirconia ceramics is a key difference in microstructure of the hydrated pure magnesia ceramics and the dual-phase magnesia-zirconia ceramics.

XRD analysis of a hydrated ceramic was first performed on a monolithic sample. The sample was prepared by cutting a disc from an as-sintered pellet. The disc was then exposed to water at 300^{o}C for 240 hours. After exposure the disc was dried in 80^{o}C air for 5 hours and subjected to X-ray diffraction analysis. After completion of the analysis the disc was ground in a mortar and passed through a sieve with an aperture of 45 microns. The resulting powder was re-analyzed. The superposition of the XRD patterns from the monolithic and powdered sample is shown in Figure 4.8. In addition to the phases characteristic for the as-sintered ceramic (cubic magnesia-zirconia solid solution and cubic magnesia), the hexagonal magnesium hydroxide $Mg(OH)_2$ was found in the monolithic sample. However, the peaks related to magnesium hydroxide were missing from the pattern collected from the powdered sample. This is likely due to the fact that magnesium hydroxide was present as a thin layer on the surface of a hydrated monolithic sample. Grinding caused dilution of magnesium hydroxide by the bulk of the sample driving the magnesium hydroxide concentration below the detection limit. These observations are consistent with the results of the SEM analysis of the hydrated microstructures discussed earlier in this section. Both SEM and XRD detect the hydration product magnesium hydroxide, but only on the surface of the ceramic.

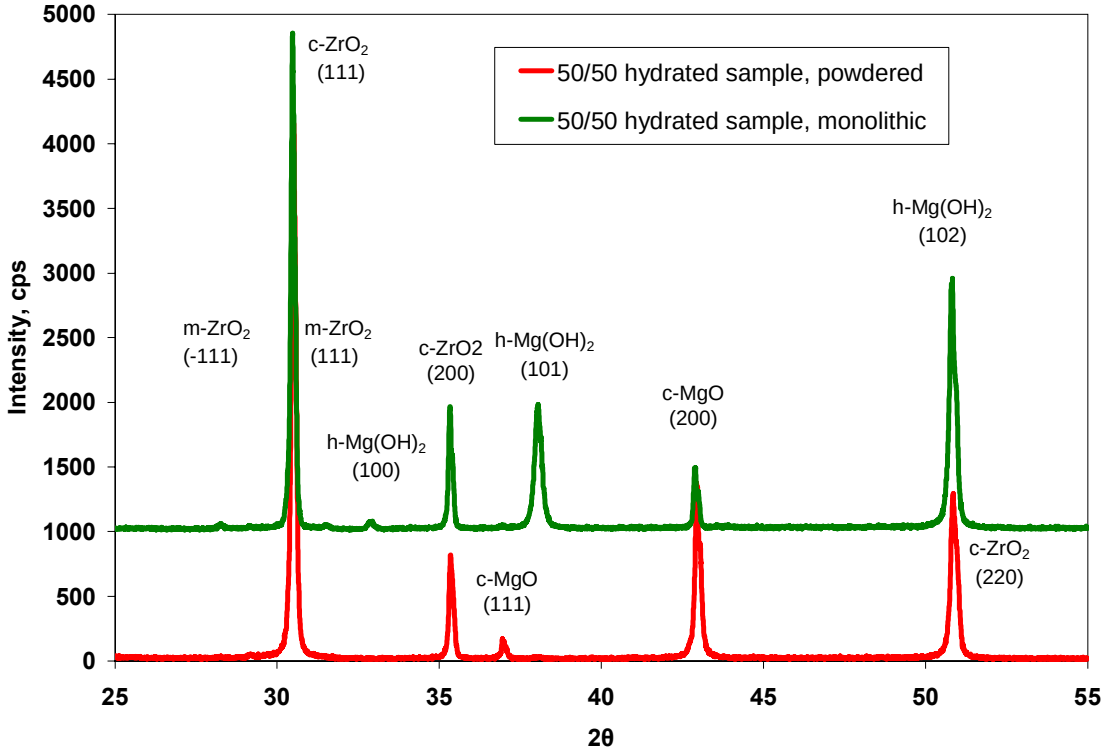

Figure 4.8. Superposition of the XRD patterns from the monolithic and powdered hydrated sample (50/50).

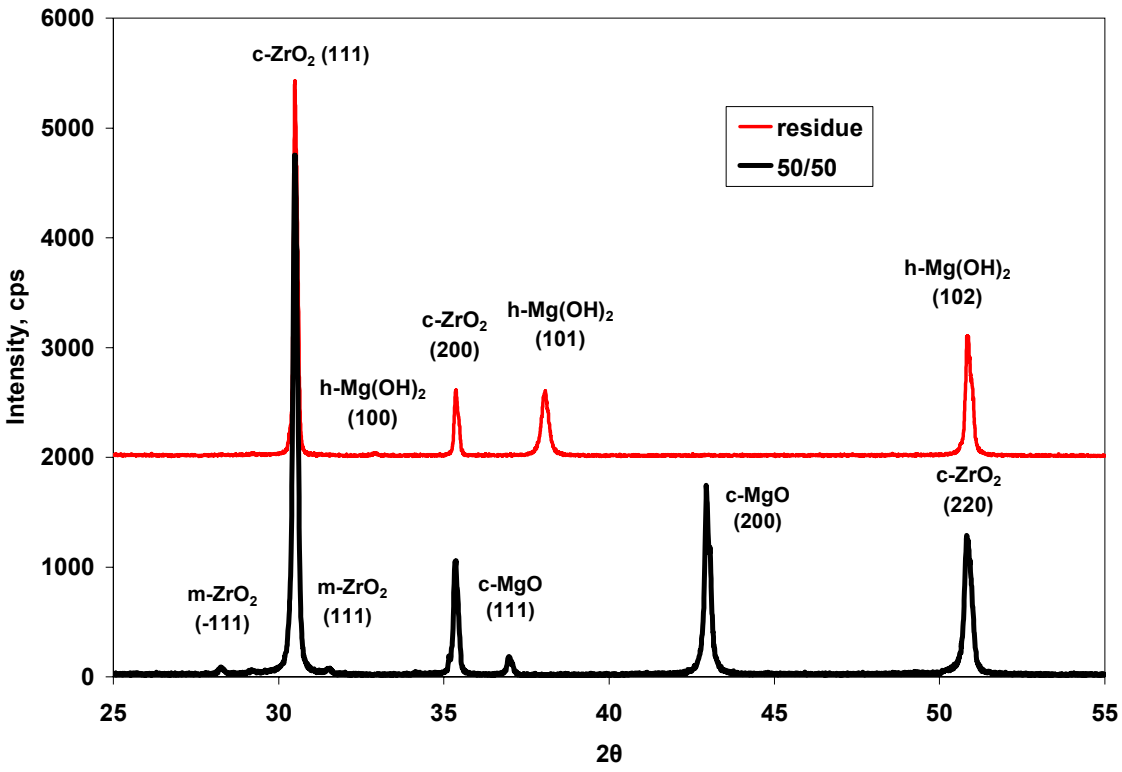

Figure 4.9. Superposition of the XRD patterns from the residue collected from the bottom of the pressure vessel and from as-sintered powdered ceramic.

While some of the hydration product was detected on the surface of the samples, the bulk of it sloughed from the samples and deposited on the bottom of the pressure vessel. This residue was collected, dried for 5 hours at 80^{o}C and subjected to the XRD analysis. The analysis of the residue revealed that it consists of two phases: cubic magnesia-zirconia solid solution and hexagonal magnesium hydroxide. The superposition of this pattern with the pattern from an as-sintered powdered ceramic is shown in Figure 4.9.

The superposition points to the absence of magnesia but presence of magnesium hydroxide in the residue, which indicates that magnesia lost by the sample is completely converted to hydroxide. The pattern for the cubic magnesia-zirconia solid solution in the residue is identical to that in the as-sintered sample. Furthermore, because no shift of zirconia peaks is observed between the two patterns, the composition of the solid solution is unaffected by hydration. No leaching of magnesium occurred from the solid solution. The most important conclusion stemming from the XRD analysis of the residue is that degradation of the magnesia-zirconia ceramics is solely due to the hydration of the magnesia phase. The loss of the cubic magnesia-zirconia solid solution phase occurs because the neighboring magnesia grains are destroyed, and the solid solution grains are no longer attached to anything.

Based on these considerations, a schematic diagram of the hydration process shown in Figure 4.10 was developed. The hydration begins on the surface and on the grain boundaries of magnesia grains (Figure 4.10a). The blue color signifies the hydration product. As in the case with pure magnesia ceramic, the stresses do arise on

the grain boundaries due to the volume increase associated with the hydration reaction. These stresses are shown as red arrows. However, the stresses in this case are not sufficient to initiate cracking of the ceramic. This assertion is based on the SEM observations that showed absence of cracks and confinement of the degradation to the surface layer of the grains, and on the XRD results that indirectly indicated that the hydration product is present as a thin layer on the surface of the ceramics. With the cracks absent, the hydration is limited to the magnesia grains on the surface (Figure 4.10b). Once they are consumed, the next layer of grains is attacked (Figure 4.10c). The hydration product in the form of fine particulate is removed from the site of reaction by convective water movement and deposited on the bottom of the pressure vessel. Finally, enough magnesia is consumed so that zirconia grains belonging to the first layer loose the bond with the monolith and are deposited on the bottom of the pressure vessel (Figure 4.10d). The process then repeats itself.

The key factor behind the improvement of the hydration in magnesia-zirconia ceramics as compared to pure magnesia ceramics is its ability to withstand the hydration induced cracking. The other significant factor is reduction of the surface area of the magnesia phase due to addition of the insoluble zirconia phase.

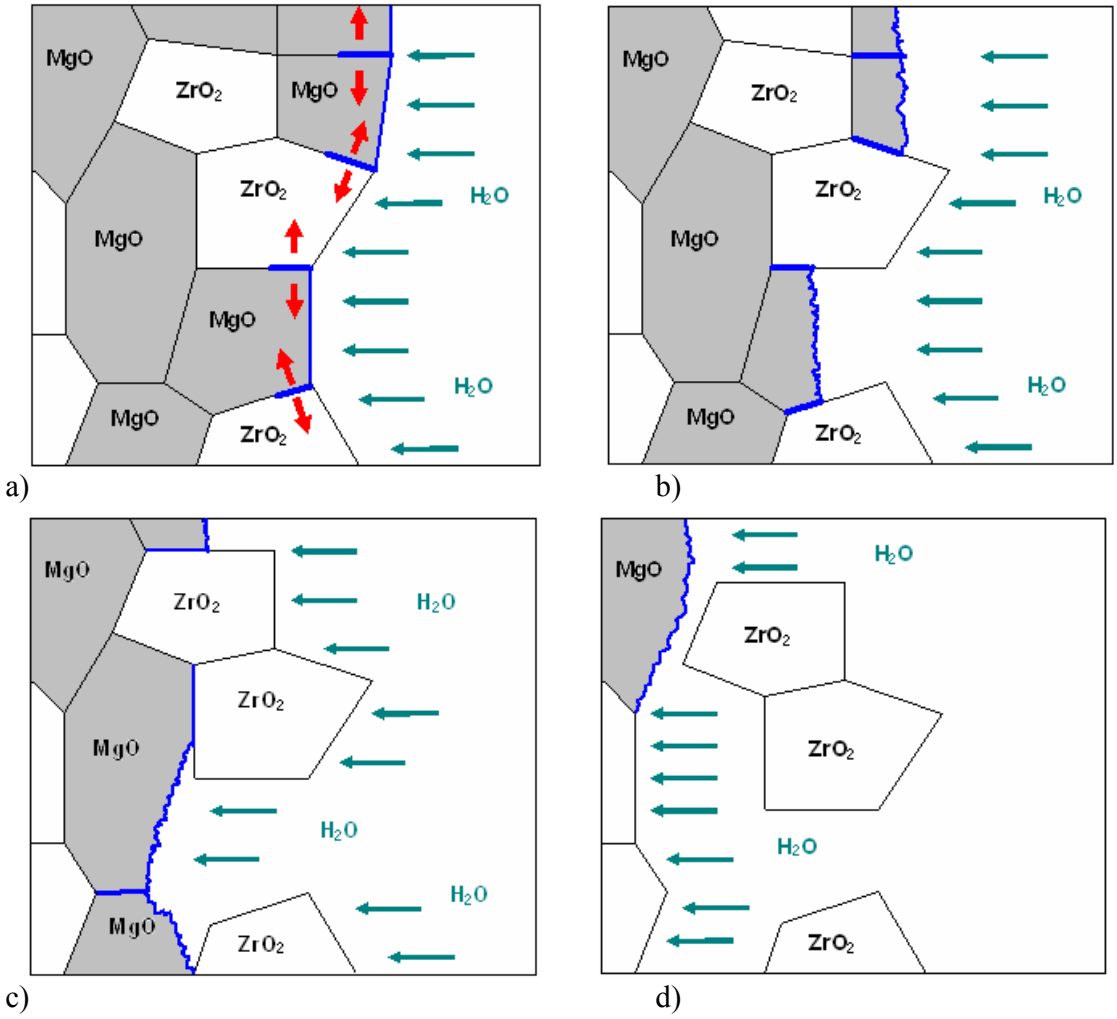

Figure 4.10. Schematic of the hydration process of the magnesia-zirconia ceramics.

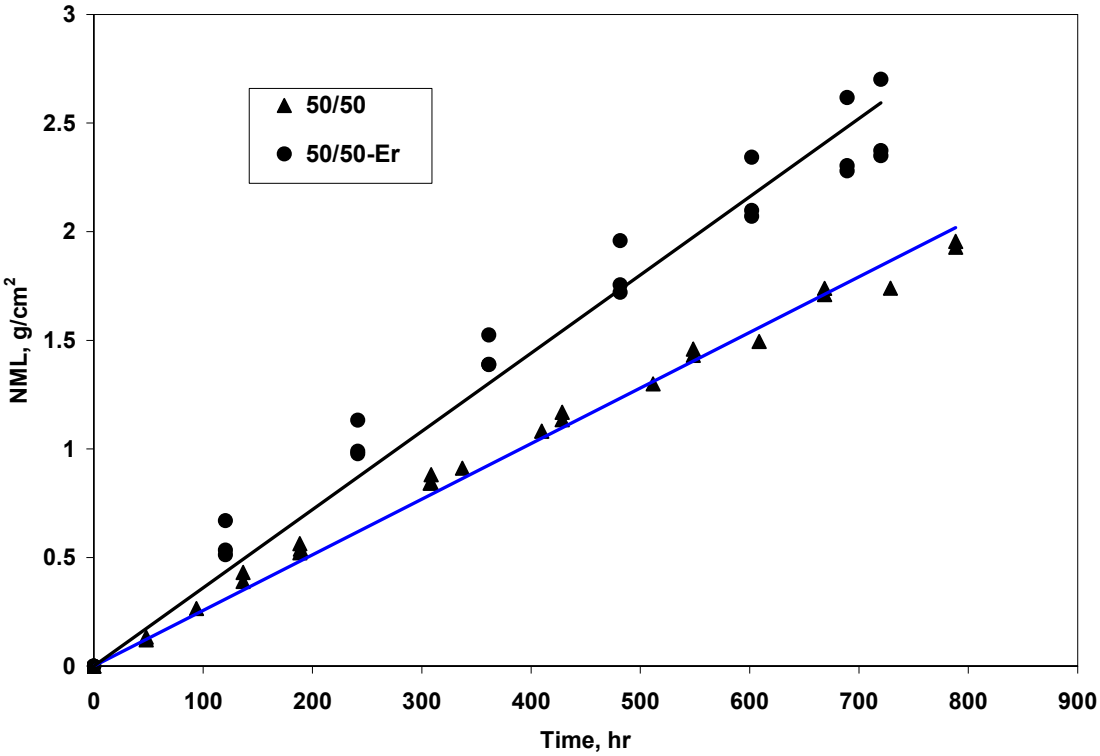

Figure 4.11. Effect of erbia doping on hydration resistance.

4.1.2.3 Effect of erbia doping on hydration resistance

Erbia doping had a negative effect on hydration resistance which is illustrated in Figure 4.11. The NMLR for the 50/50-Er composition was 0.003669 g/cm^2/hr while the NMLR for the 50/50 composition was 0.002559 g/cm^2/hr.

4.1.2.4 Effect of the boron presence in the water on hydration resistance

Presence of boron in the water had a dramatic positive effect on the hydration resistance. At 300^{o}C the NMRL for the 50/50 composition was 0.00005667 g/cm^2/hr in the 13000 ppm aqueous solution of the boric acid (pH=4.9) containing trace amounts (~7 ppm) of lithium hydroxide. This is 45 times less than the NMRL measured for the same ceramic in the de-ionized water. Furthermore, the mass loss exhibits saturation with time, as evident from Figure 4.12. Saturation of mass loss with time is a key difference between the behavior in borated and de-ionized water. This suggests that the reaction in borated water is likely self-limiting and results in the passivation of magnesia.

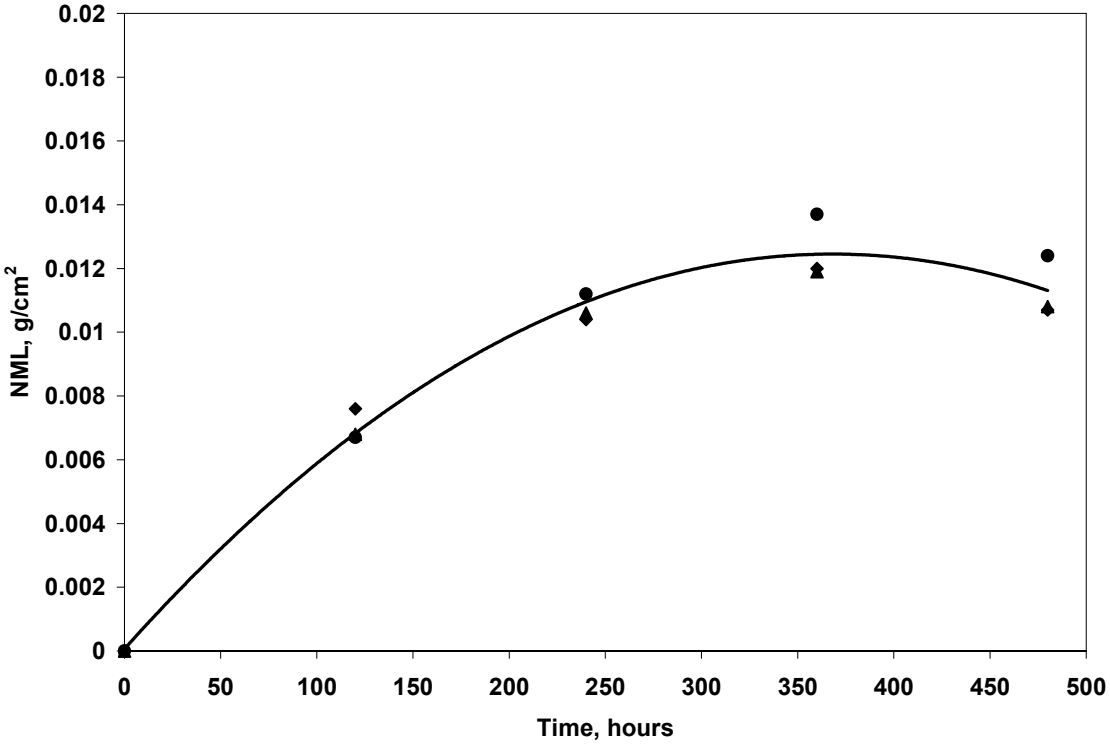

Figure 4.12. Saturation with time of the sample mass loss exhibited in the 13000 ppm borated water.

Explanation of the positive effect of boron on the hydration resistance was found by conducting XRD analysis of the surface of the ceramic pellet previously exposed to the 13000 ppm aqueous solution of the boric acid at 300^{o}C. The corresponding XRD pattern is shown in Figure 4.13. Besides magnesia and magnesia-zirconia solid solution phases, the magnesium borate hydroxide $Mg(OH)BO_2$ was identified in the sample. Magnesium hydroxide, typically observed in samples exposed to the de-ionized water, was not detected in the sample exposed to the borated water. Based on these results it was concluded that in the presence of the boric acid the reaction of magnesia with water with formation of magnesium hydroxide is suppressed. Instead, the following reaction takes place:

$$MgO+H_3BO_3 \rightarrow Mg(OH)BO_2\downarrow+H_2O \qquad (4.5)$$

Therefore, the difference in the behavior of the ceramics in de-ionized and borated water is due to the different chemical reaction that takes place during exposure.

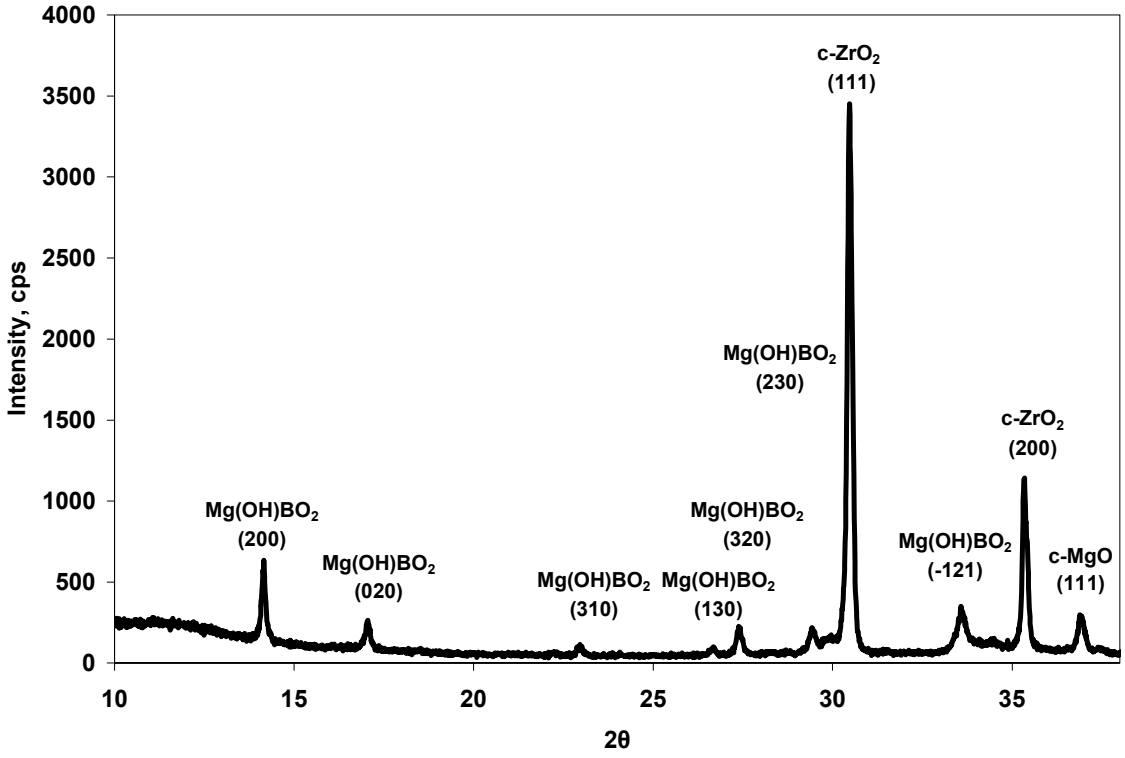

Figure 4.13. XRD pattern of the surface of the ceramic pellet exposed to the 13000 ppm aqueous solution of the boric acid at 300^{o}C

It is recognized, that in a LWR the boron concentration is expected to vary from 0 ppm to 4400 ppm depending on the reactor power and burnup [107]. Here the concentration of 4400 ppm of boron is equivalent to the 25198 ppm of boric acid. Thus, the value of 13000 ppm used in this work represents a median value. A more detailed investigation of the boron effect on the hydration resistance, particularly at different boron concentrations, was beyond the scope of this work. However, the results shown here indicate that presence of boron in the reactor coolant should be viewed as an advantage in addressing the fuel safety implications of the hydration issue.

4.2 THERMAL ANALYSIS

4.2.1 Thermal diffusivity measurement

4.2.1.1 Experimental procedure

The experimental procedure described elsewhere [108] was followed. The procedure is based on delivering a pulse of thermal energy to one face of the analyzed sample and monitoring the temperature rise of the opposite face. The thermal diffusivity, α (cm^2/s) is determined from sample thickness L (cm), and the time elapsed from the moment when the pulse of thermal energy is delivered to the moment when the temperature of the opposite face of the sample reaches half of its maximum $t_{½}$ (s):

$$\alpha = \frac{0.13879 L^2}{t_{1/2}} \tag{4.6}$$

The Flashline 5000 Thermal Properties Analyzer (Anter Corporation, Pittsburg, PA) was utilized in this work. The apparatus employs a neodymium/glass laser as a source of thermal energy. The temperature rise of the sample is monitored by a solid-state infrared detector. Measurement and data collection are fully automated, and up to six samples can be analyzed simultaneously.

The measurements were performed on two sets of disk-shaped test specimens. The specimens included in the first set were 2 mm thick, while the specimens included in the second set were 3 mm thick. The diameter of specimens in both sets was 6.25-6.28 mm. They were machined from as-sintered pellets by an outside contractor (International Ceramics Engineering, Worcester, MA). Machined discs were coated on both faces with a very thin layer of palladium using a Hummer sputter coater (Anatech LTD, Denver, NC). A second coat of colloidal graphite was then sprayed-on to prevent possible reflection of the laser beam by the palladium coating. The measurements were performed in a flowing argon atmosphere.

For each analyzed sample multiple attempts to measure thermal diffusivity were performed at each given temperature. Spurious measurements caused by either excessive or insignificant laser power were identified by examining the raw data and the temperature rise curves. Results of such measurements were excluded from further consideration.

4.2.1.2 Results and discussion

The results of thermal diffusivity measurements versus temperature are shown in Figure 4.14 through Figure 4.19. These figures reflect the values of corrected for undesired conduction and radiation heat losses that occur during the measurement. The Cowan cooling curve correction [108] was used to account for the conduction heat losses to the sample holders and for the radiation heat losses from the sample surfaces. The correction was performed utilizing the software provided by the manufacturer of the Flashline 5000 Thermal Properties Analyzer (Anter Corporation, Pittsburg, PA). Due to this correction, the reported values were 5-25% lower then the raw values determined from the temperature rise data using the equation above. The difference due to the correction increased with an increase of temperature, which indicated that more heat is lost by conduction and radiation at higher measurement temperatures. An illustration of how the Cowan correction has affected the data is shown in Figure 4.20.

The trendlines included in Figure 4.14 through Figure 4.19 represent the third order polynomial fits of the corrected thermal diffusivity data. The polynomial fits were generated by conducting a least squares linear regression analysis. The resulting equation is as follows:

$$\alpha = aT^3 + bT^2 + cT + d \tag{4.7}$$

where α is thermal diffusivity in s/cm^2; T is temperature in degrees C; and a, b, c, and d are coefficients. The coefficients for specific compositions are listed in Table 4.1. The values of R-squared are included in Table 4.1 as indicators of the goodness of fit.

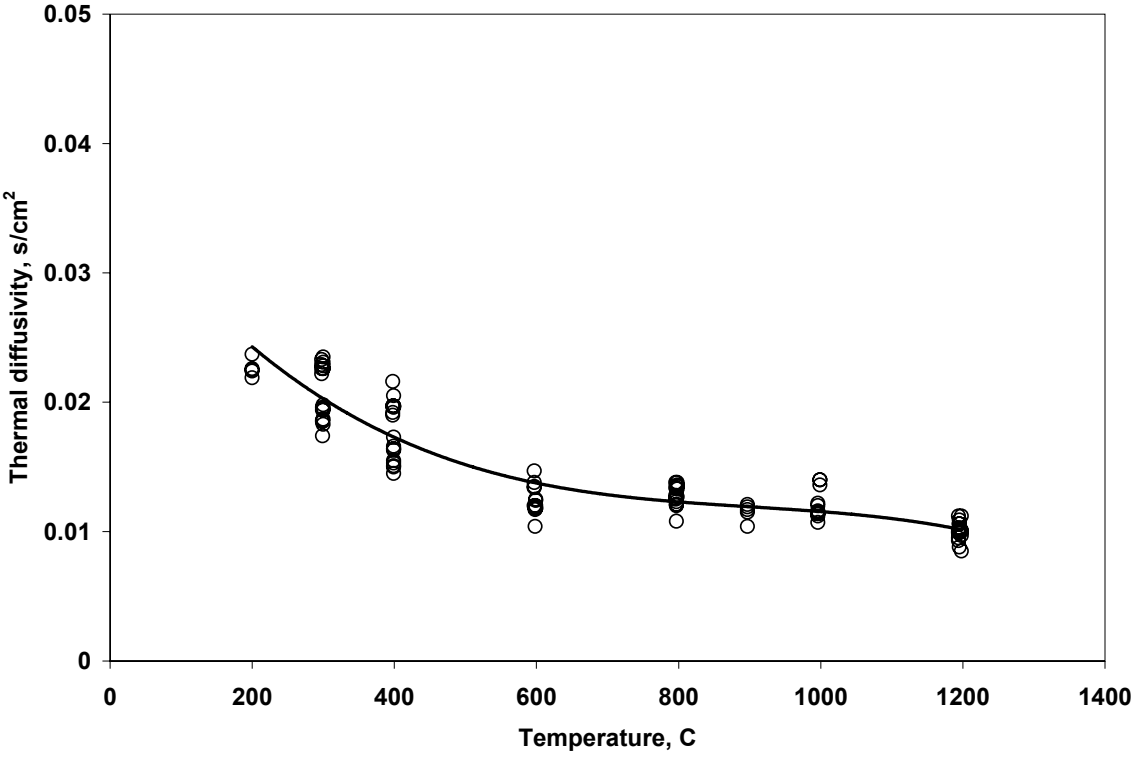

Figure 4.14. Thermal diffusivity of the 40/60 ceramic composite.

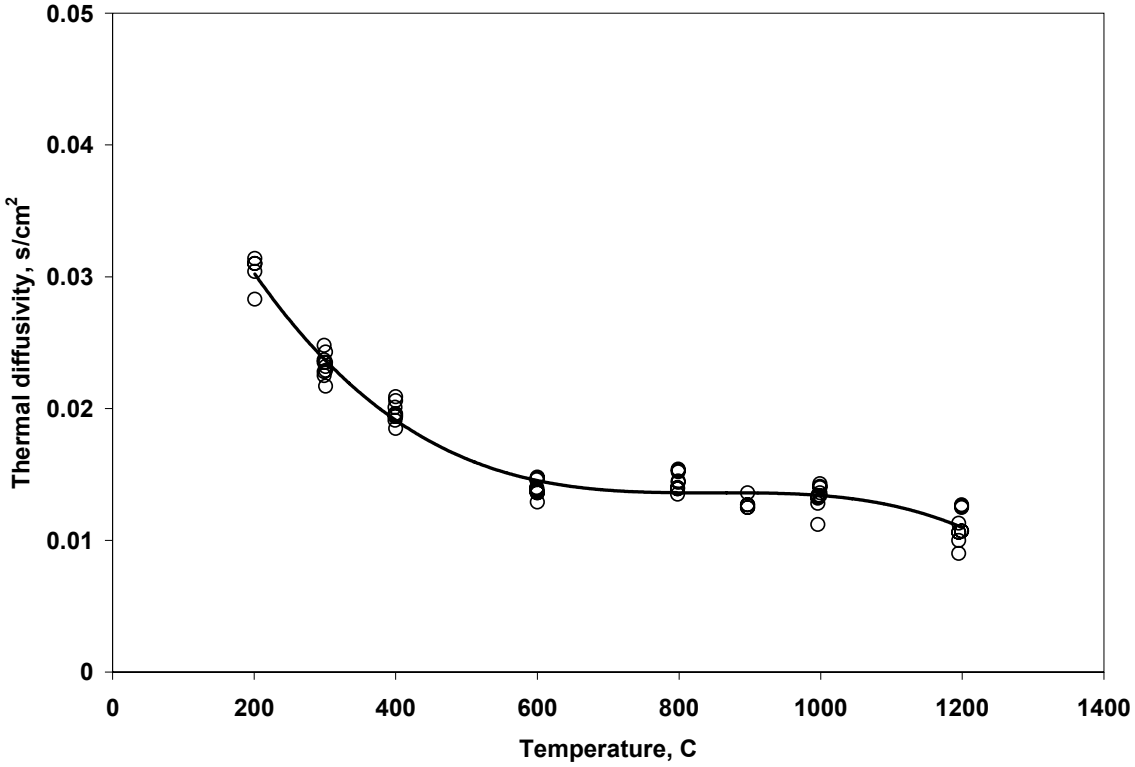

Figure 4.15. Thermal diffusivity of the 50/50 ceramic composite.

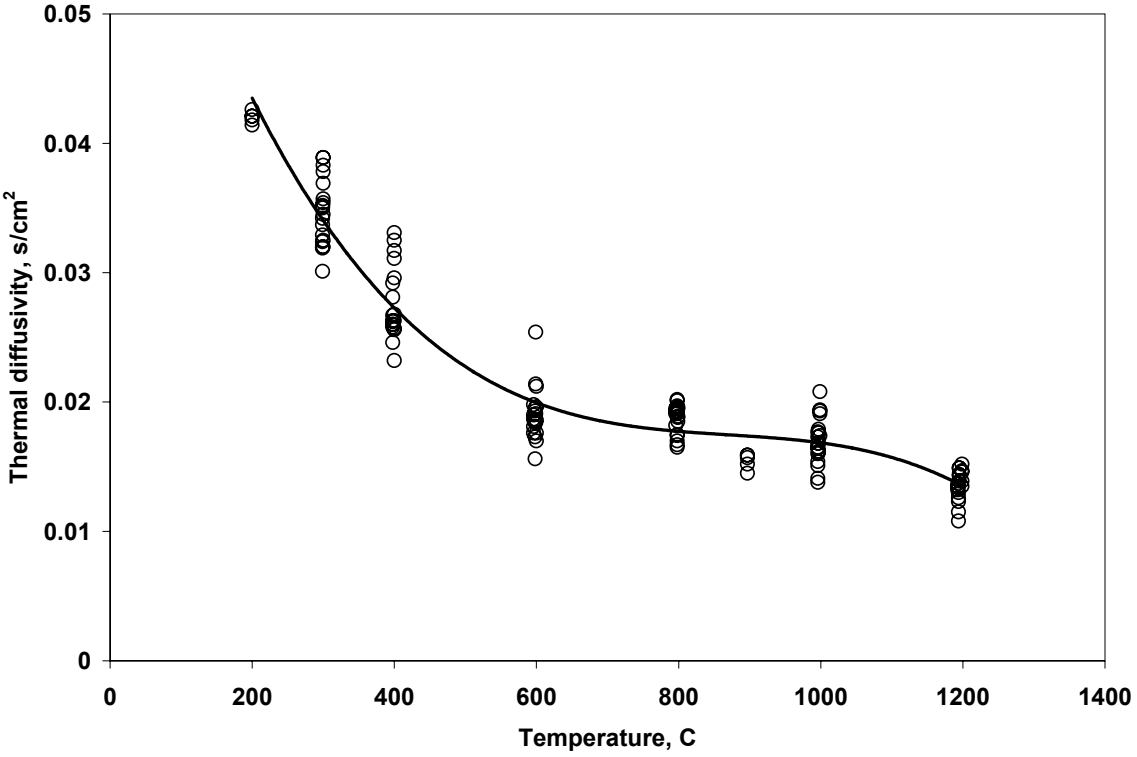

Figure 4.16. Thermal diffusivity of the 60/40 ceramic composite.

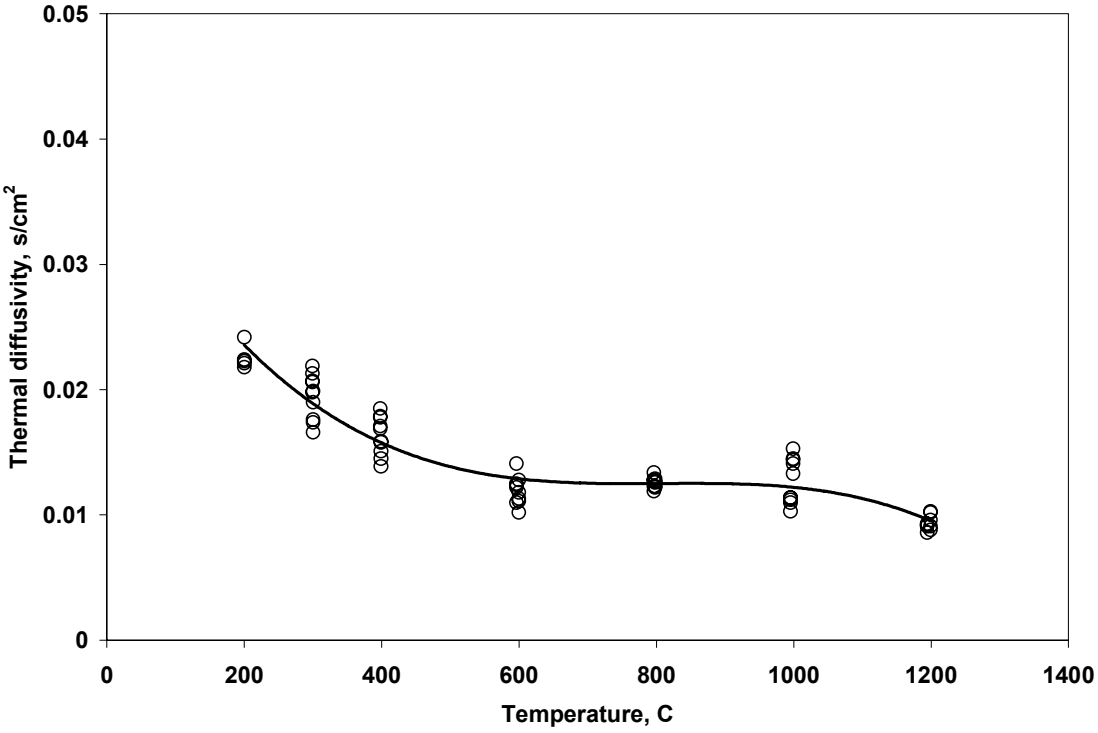

Figure 4.17. Thermal diffusivity of the 40/60-Er ceramic composite.

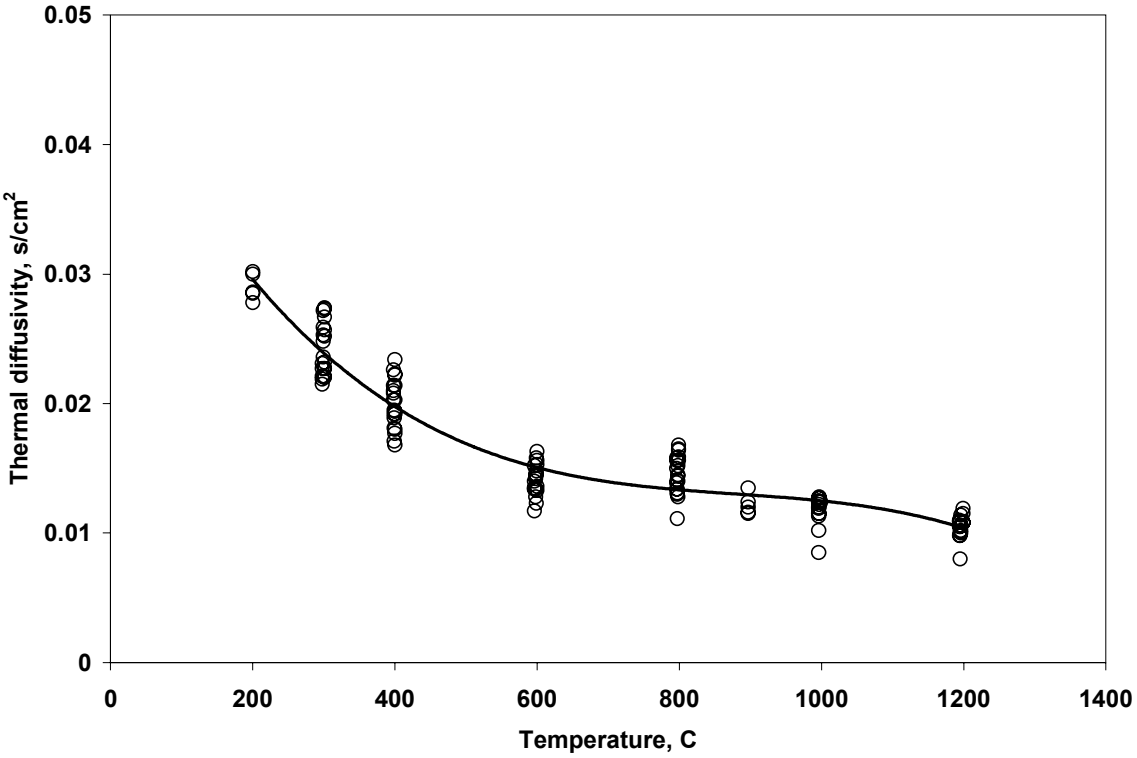

Figure 4.18. Thermal diffusivity of the 50/50-Er ceramic composite.

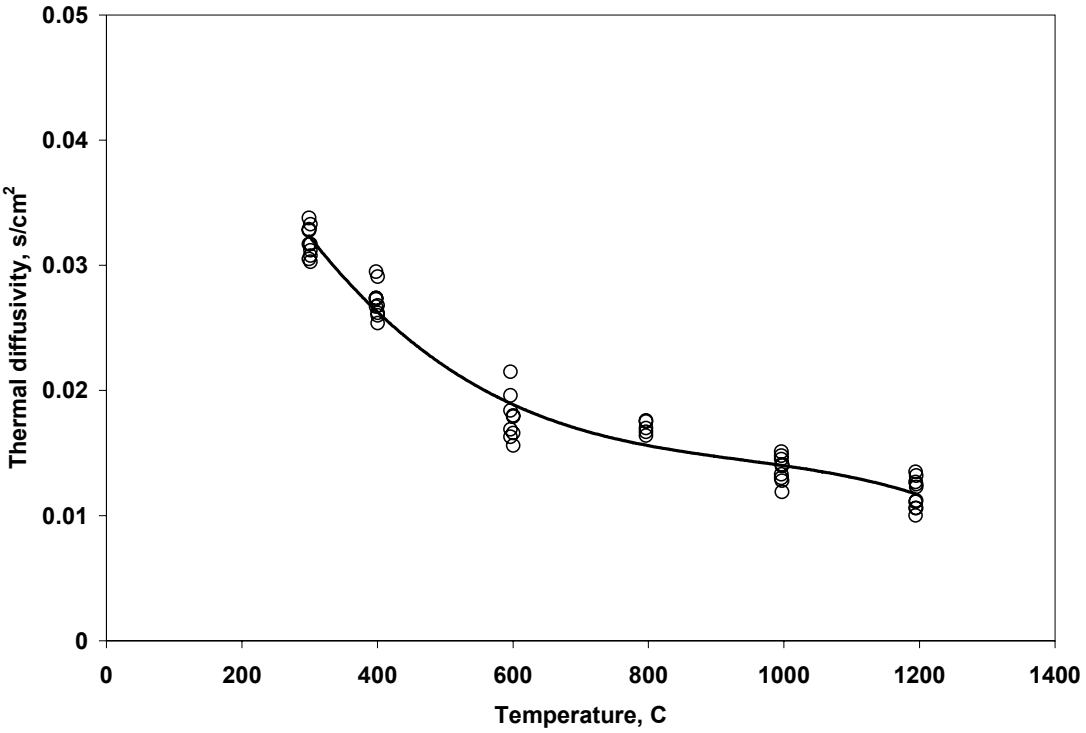

Figure 4.19. Thermal diffusivity of the 60/40-Er ceramic composite.

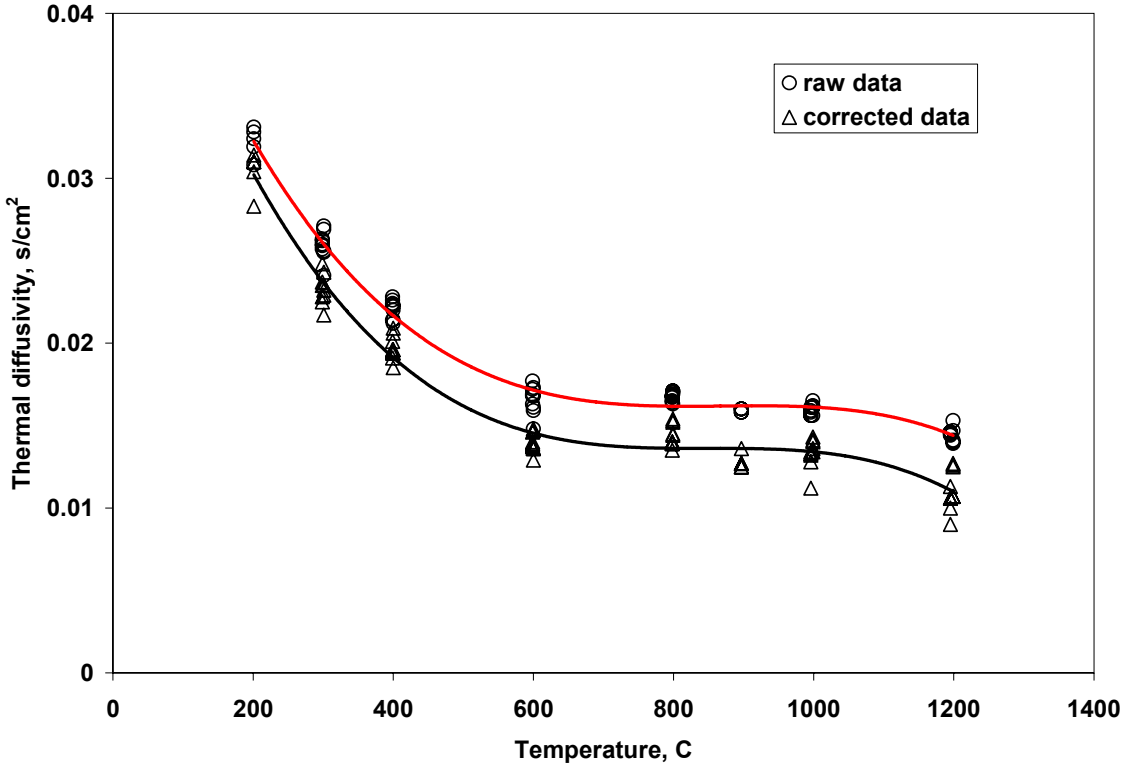

Figure 4.20. Effect of Cowan cooling correction on the thermal diffusivity data. The 50/50 composite data is shown.

Table 4.1. Coefficients of the polynomial fits of the thermal diffusivity data.

Composition	a	b	c	d	R^2
40/60	-2.862515×10^{-11}	7.754661×10^{-8}	-7.348286×10^{-5}	0.03610923	0.8680
50/50	-6.128045×10^{-11}	1.559863×10^{-7}	-1.322989×10^{-4}	0.05099793	0.9700
60/40	-7.883493×10^{-11}	2.057700×10^{-7}	-1.824712×10^{-4}	0.07238260	0.9389
40/60-Er	-5.089583×10^{-11}	1.228926×10^{-7}	-9.856508×10^{-5}	0.03877326	0.8874
50/50-Er	-4.426592×10^{-11}	1.170406×10^{-7}	-1.069412×10^{-4}	0.04664686	0.9169
60/40-Er	-5.055004×10^{-11}	1.423967×10^{-7}	-1.409894×10^{-4}	0.06312453	0.9659

The thermal diffusivity of the binary and ternary systems investigated in this work appears to be driven by the temperature and composition. The decrease of thermal diffusivity with temperature is obvious. However, the degradation of thermal diffusivity with temperature is less pronounced at temperatures above 600^{o}C. To account for this behavior, the preference was given to the third degree polynomial fits of thermal diffusivity versus temperature, rather than the commonly used inverse temperature fits.

Ronchi et al. [109] explained improvement of thermal conductivity in heterogeneous zirconia-actinide ceramics composites by the improvement of the interface conductance between two phases at high temperature. According to Ronchi et al., the latter is due to the difference in the thermal expansion between two phases. This explanation may be valid for the systems examined in this work, since magnesia is known to have significantly higher thermal expansion than zirconia.

To further illustrate the discontinuity in thermal diffusivity behavior, the inverse thermal diffusivity versus temperature is plotted in Figure 4.21. The dependence is clearly linear below 600^{o}C, but the linearity no longer exists above 600^{o}C.

With respect to the compositional dependence of thermal diffusivity, it was found that thermal diffusivity increases with the increase of magnesia content in the ceramics. This trend was observed for both binary and ternary compositions. The superposition of thermal diffusivity plots obtained for different concentrations of magnesia illustrates this trend. The plots for binary compositions are shown in Figure 4.22. The plots for ternary compositions are shown in Figure 4.23. For clarity, only polynomial fits, and not the entire data sets are shown.

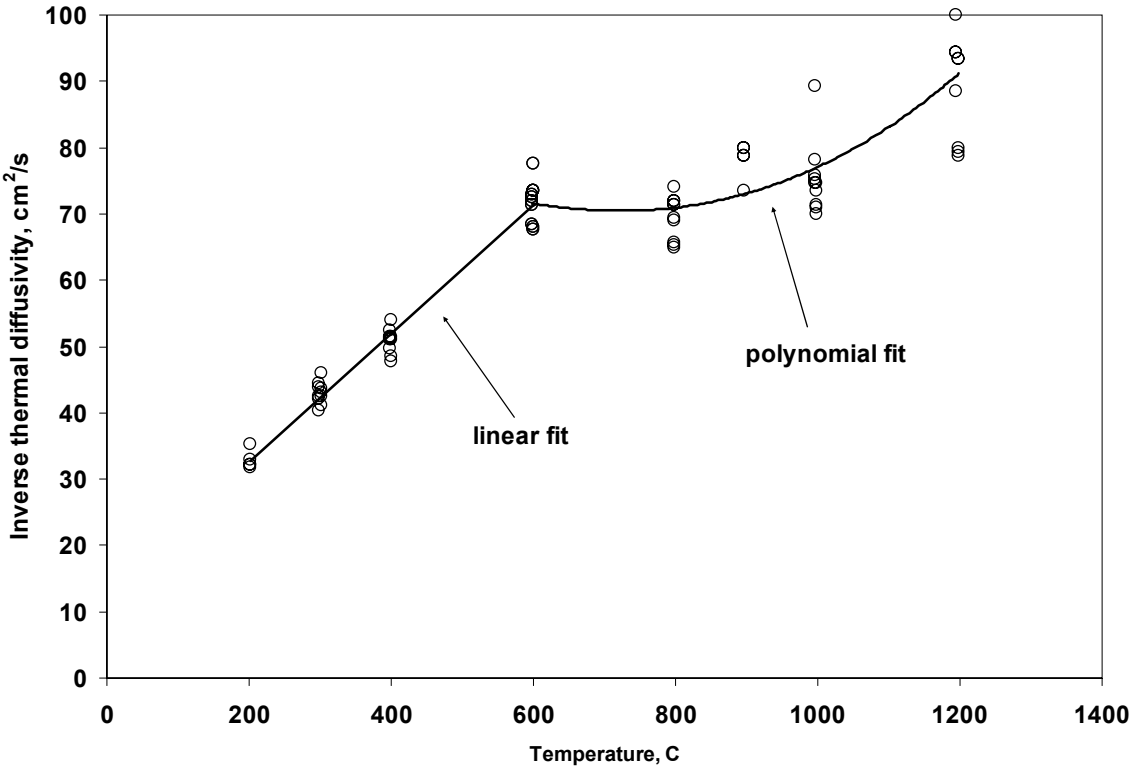

Figure 4.21. Inverse thermal diffusivity versus temperature. The 50/50 composite data is shown.

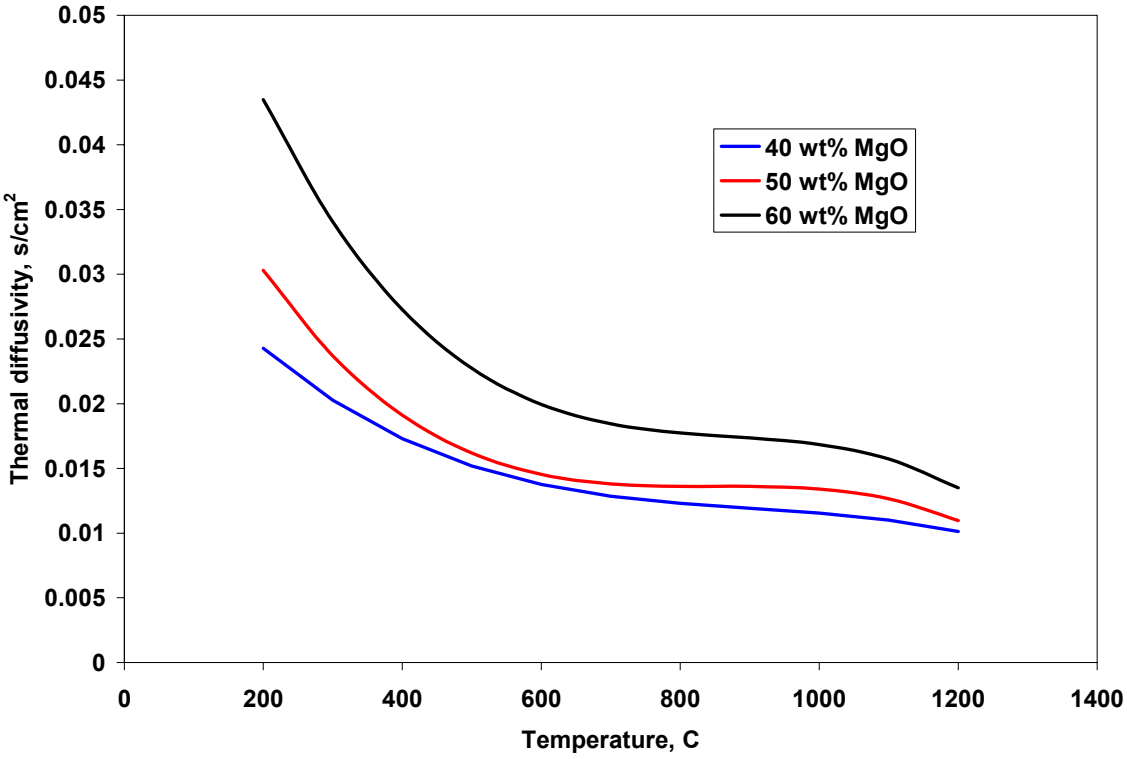

Figure 4.22. Effect of magnesia content on thermal diffusivity of the binary compositions.

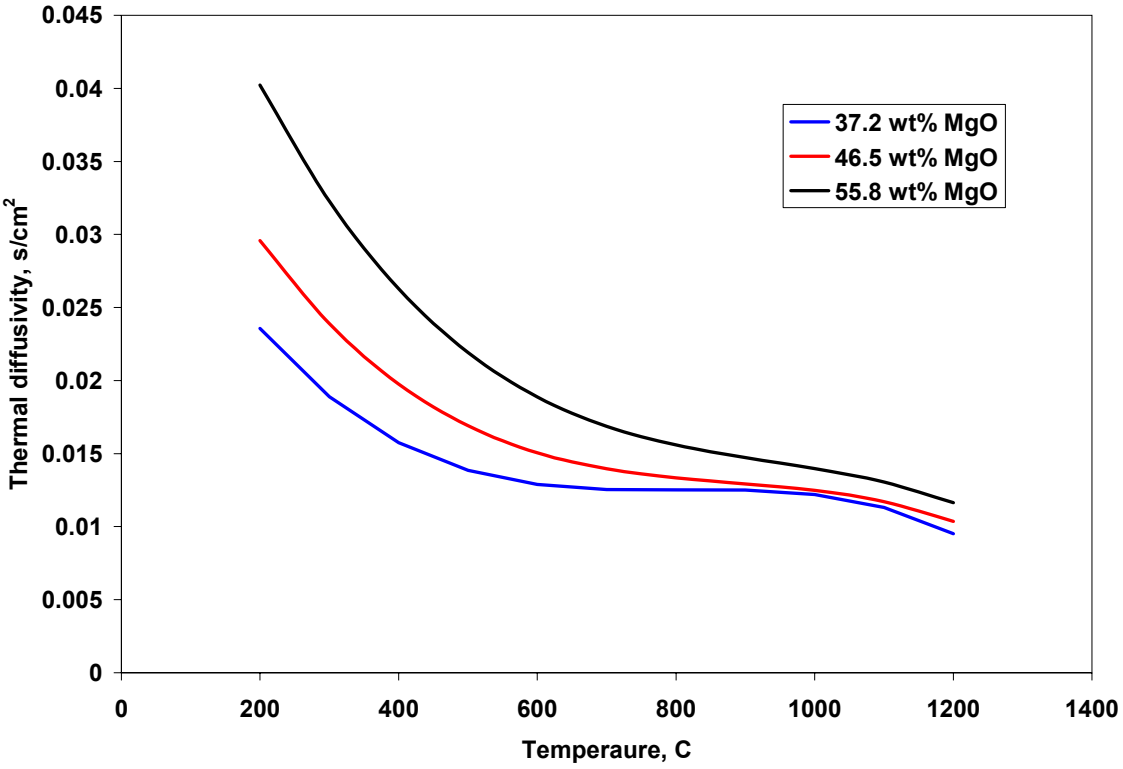

Figure 4.23. Effect of magnesia content on thermal diffusivity of the ternary compositions.

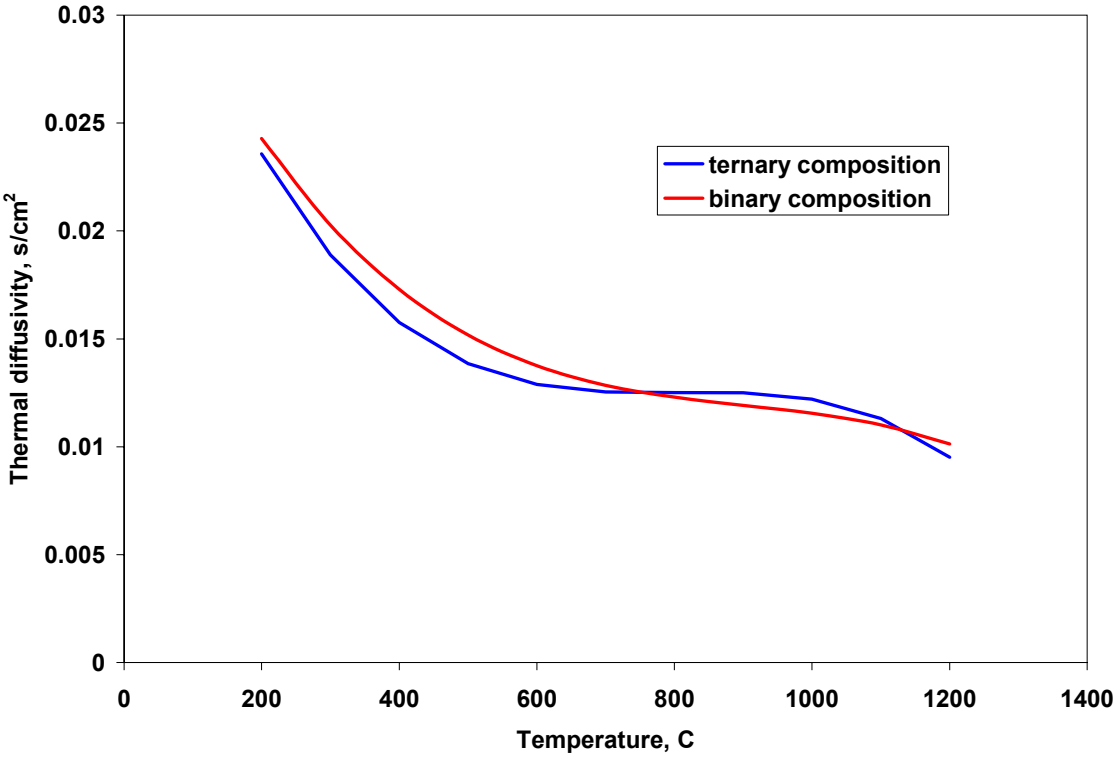

Figure 4.24. Effect of erbia doping on thermal diffusivity. Data for the 40/60 and 40/60-Er composites is shown.

Erbia doping had an insignificant effect on the thermal diffusivity of ceramic composites, which is illustrated in Figure 4.24. It has been noted by Degueldre et al. [7] that doping of zirconia with rare earth and actinide oxides including plutonia results in a large decrease of thermal conductivity of zirconia-based inert matrix fuel. Therefore, the insignificant effect of erbia doping on the thermal diffusivity of magnesia-zirconia composites is a notable advantage over zirconia-based inert matrix fuels. This phenomenon is explained by a favorable phase distribution that takes place when magnesia-zirconia composite is doped with erbia. As it was established by SEM and XRD, erbia dissolves completely in the zirconia phase, leaving the magnesia phase uncontaminated. The latter implies that the thermal transport properties of magnesia are unaffected by erbia doping. It is understood that erbia doping is likely to reduce the thermal diffusivity of the zirconia phase; however, as evident from Figure 4.24, the net effect of doping on the thermal diffusivity of the composite is not significant.

4.2.2 Heat capacity determination

Heat capacity was determined using the rule of mixtures from the published heat capacity data of magnesia, zirconia, and erbia. Based on this rule, the heat capacity of a ceramic composite can be determined as follows:

$$C_{composite} = aC_{MgO} + bC_{ZrO_2} + cC_{Er_2O_3} \quad (4.8)$$

Where a, b, and c are the weight fractions of the components in the ceramic, and C, J/(kg C) is the heat capacity of the individual components.

The following equations defining the temperature dependence of the heat capacity of individual components were used.

For magnesia:

$$C_{MgO}=47.25995+5.681621\times10^{-3}T-8.72665\times10^{-7}T^{2}+ \\ +1.043\times10^{-10}T^{3}-1.053955\times10^{6}T^{-2} \quad (4.9)$$

where T is temperature in Kelvin, and C_p is heat capacity in Joule/K-mole.

For zirconia:

$$C_{ZrO_2}=69.20001+8.54829\times10^{-3}T-8.62921\times10^{-7}T^{2}+ \\ +2.46374\times10^{-10}T^{3}-1.382767\times10^{6}T^{-2} \quad (4.10)$$

where T is temperature in Kelvin, and C_p is heat capacity in Joule/K-mole.

For erbia:

$$C_{Er_2O_3}=30.93+7.8\times10^{-4}T-4.65\times10^{5}T^{-2} \quad (4.11)$$

where T is temperature in Kelvin, and C_p is heat capacity in calorie/mole-deg.

The equations for magnesia and zirconia were recommended by Ottaviani [110] based on the published data. The equation for erbia was developed by Tsagareishvili and Gvelesiani [111] based on the experimental measurements.

Based on these equations the temperature dependence of the heat capacity for the ceramic compositions under investigation was calculated. Necessary unit conversions were made to insure consistency of the units between Equation 4.8 and Equations 4.9-4.11. The results of this calculation are shown in Figure 4.25. The values of heat capacity were used later for thermal conductivity determination.

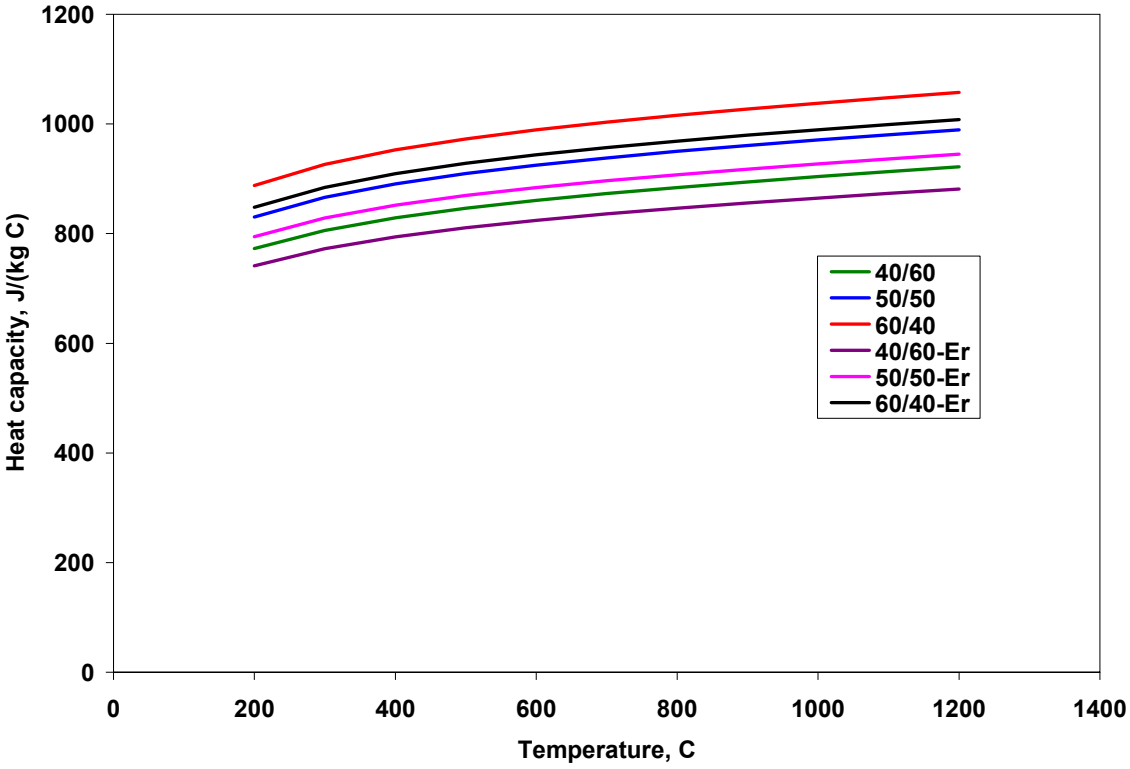

Figure 4.25. Heat capacity of the ceramic compositions under investigation.

4.2.2.1 Thermal conductivity determination

Thermal conductivity was determined from thermal diffusivity, heat capacity, and density of the ceramics according to the following equation:

$$k = \alpha\rho C \tag{4.12}$$

Where α is thermal diffusivity in s/m^2, ρ is density in kg/m^3, and C is specific heat in Joule/kg C. The values of the thermal conductivity calculated from the measured thermal diffusivity, measured density and estimated heat capacity are plotted in Figure 4.26 and Figure 4.27. The literature values [31] for fully dense UO_2 are included for comparison.

The plots in Figure 4.26 and Figure 4.27 represent the third order polynomial fits of the calculated data. The polynomial fits were generated by conducting a least squares linear regression analysis. The resulting equation is as follows:

$$k = aT^3 + bT^2 + cT + d \tag{4.13}$$

where k is thermal conductivity in W/m C; T is temperature in degrees C; and a, b, c, and d are coefficients. The coefficients for specific compositions are listed in Table 4.2.

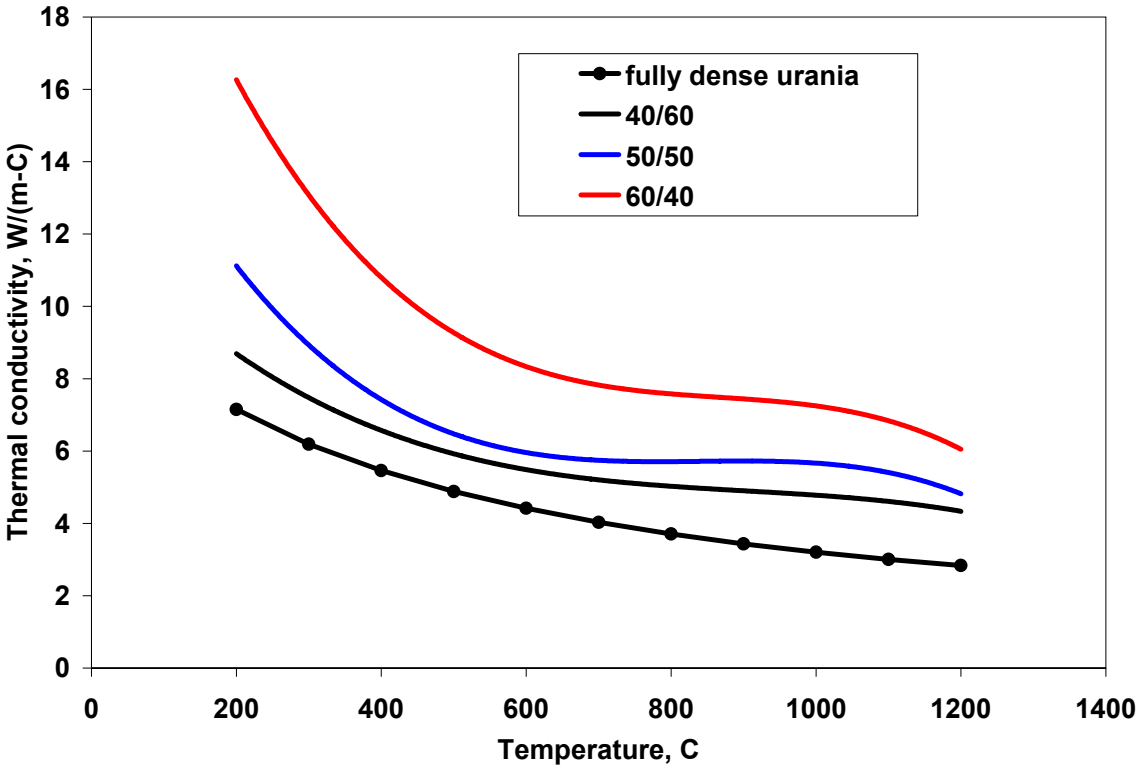

Figure 4.26. Thermal conductivity of binary magnesia-zirconia ceramics.

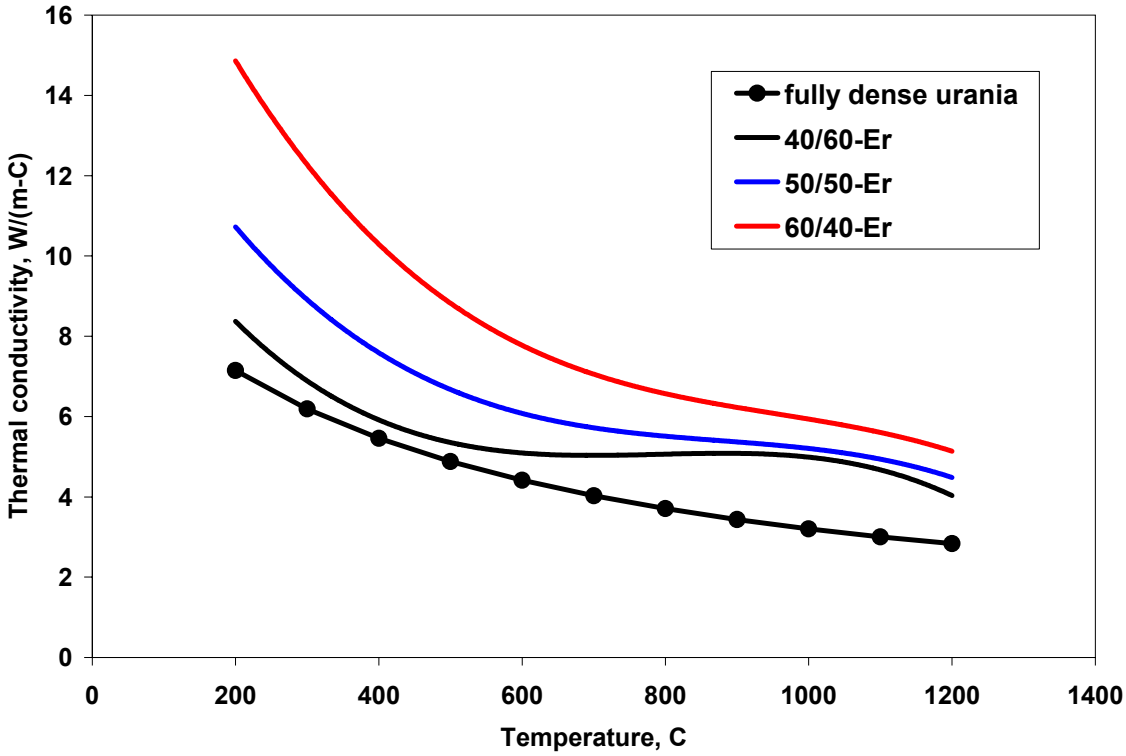

Figure 4.27. Thermal conductivity of ternary magnesia-zirconia-erbia ceramics.

Table 4.2. Coefficients of the polynomial fits of the thermal conductivity versus temperature.

Composition	a	b	c	d
40/60	-0.8575×10^{-8}	2.3248×10^{-5}	-2.2157×10^{-2}	12.26175
50/50	-2.1058×10^{-8}	5.3122×10^{-5}	-4.4452×10^{-2}	18.05258
60/40	-2.6855×10^{-8}	6.9733×10^{-5}	-6.1654×10^{-2}	26.02313
40/60-Er	-1.7461×10^{-8}	4.1348×10^{-5}	-3.2196×10^{-2}	13.29746
50/50-Er	-1.4169×10^{-8}	3.7292×10^{-5}	-3.4078×10^{-2}	16.16135
60/40-Er	-1.5390×10^{-8}	4.4094×10^{-5}	-4.4982×10^{-2}	22.21508

4.2.3 Calculation of the fuel centerline temperature

The fuel centerline temperature was calculated for a hypothetical case of an LWR reactor fueled with the IMF based on the ceramic compositions developed in this work. It was assumed, that the fuel was a solid-solution type, with the fissile phase dissolved in zirconia phase. It was also assumed, that dissolution of the fissile phase did not affect the thermal conductivity of the ceramic. This assumption was loosely based on the findings of this work relative to the effect of erbia doping on thermal transport properties of the magnesia zirconia ceramics. These findings show that addition of small amounts of dopants have minor effect on thermal transport properties. The loading of the fissile phase is not expected to exceed 5 wt%. The calculation described here is for the beginning of the reactor core life, thus, no burnup effects on thermal conductivity were included in the calculation. It is also assumed that the heat source is uniformly distributed in the fuel pellet.

With these assumptions, the following equation [112] provides a valid description of the heat conduction in the fuel rod with uniformly distributed heat sources and temperature dependant thermal conductivity:

$$\int_{Ts}^{Tcl} k(T)dT = \frac{q' r^2}{4} \tag{4.14}$$

where, $k(T)$ is thermal conductivity as a function of temperature, T_{cl} is the fuel pellet centerline temperature, T_s is the fuel pellet surface temperature, q' is heat generation per unit volume, r is the fuel pellet radius.

To proceed with the calculation, the fuel pellet radius of 4.095 mm and fuel pellet height of 10 mm were assumed. This is typical pellet geometry for pressurized water reactors. A linear power density of 426 W/cm was chosen, which is a maximum value characteristic for a Westinghouse PWR [65] during normal operation. Use of the maximum value for the linear power density in these calculations will yield an estimate of the maximum fuel centerline temperature. Linear power density of 426 W/cm is equivalent to the volumetric density of $8.0866 \cdot 10^8$ W/m^3 for the specified pellet geometry.

Results of the fuel centerline temperature calculation performed for six ceramic compositions under investigation are shown in Figure 4.28 The calculation was performed for the range of the pellet surface temperatures from 300^{o}C to 600^{o}C, typical for normal reactor operation. As evident from Figure 4.28, the fuel centerline temperature stays far below the expected ceramic melting temperature of 2100^{o}C and is significantly lower then Westinghouse PWR maximum fuel temperature of 1788^{o}C [65]. Therefore, these results prove that all of the ceramic compositions investigated in this study have the thermal conductivity high enough to ensure operation of the IMF fuel at the temperature well below melting and well below maximum fuel operating temperatures currently authorized in LWRs.

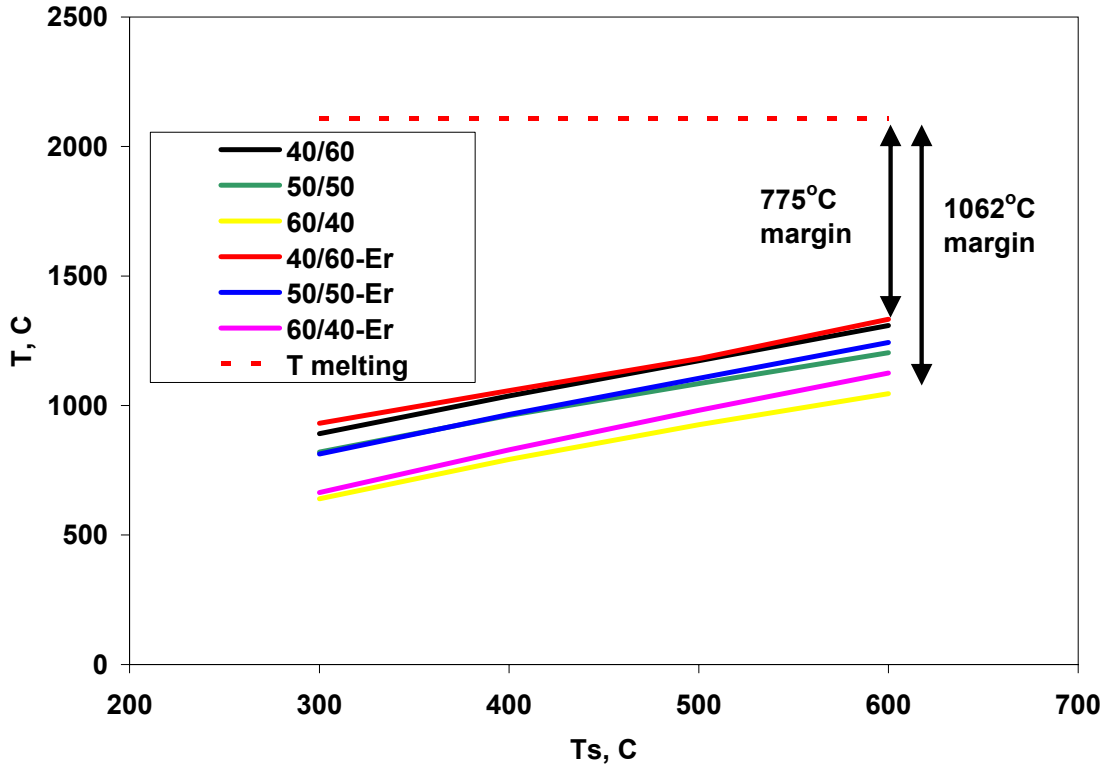

Figure 4.28. Fuel centerline temperature as a function of the fuel surface temperature calculated for six inert matrix compositions.

4.3 SUMMARY

The feasibility study presented in this chapter addressed two key issues associated with the use of magnesia-zirconia ceramics in LWR fuels. The first issue is stability in the reactor coolant. The study has shown experimentally that dual phase magnesia-zirconia ceramics have a meaningful engineering lifetime when exposed to the reactor coolant. The engineering lifetime can be controlled by adjusting the composition of the ceramics, and the compositional dependence of the ceramic durability follows the Arrhenius-type equation. The second issue is thermal transport properties and their effect on fuel operating temperature. Thermal analysis, based on both experimental and analytical techniques, established, that the product of all investigated compositions has the thermal conductivity superior to that of UO_2/MOX fuels and zirconia-based fuels. Analysis of heat conduction in a hypothetical magnesia-zirconia fuel rod with uniformly distributed heat sources and temperature dependant thermal conductivity yielded estimates of the fuel centerline temperature that are well below the ceramic melting temperature and well below the maximum fuel temperatures currently authorized in LWRs.

CHAPTER V

CONCLUSIONS

The main outcome of this work is the development of a principally new inert matrix for LWR fuel: dual phase magnesia zirconia ceramics. The concept for use of this composite material in LWR capitalizes on the known advantages of the composite's ingredients: magnesia and zirconia. Magnesia brings high thermal conductivity. Zirconia brings exceptional stability in LWR coolant. As a result of this combination, the product posts significant performance improvements over its precursors.

When it comes to chemical interaction with reactor coolant, the product features exponential decrease of the mass loss due to hydration with an increase of zirconia content. The normalized mass loss rates measured in static 300^{o}C de-ionized water for the magnesia-zirconia ceramics containing 40, 50, 60, and 70 weight percent of zirconia are, 0.00688, 0.00256, 0.000595, 0.000131 g/cm^2/hr respectively. The presence of boron in the water had a dramatic positive effect on the hydration resistance. At 300^{o}C the normalized mass loss rates for the composition containing 50 weight percent of zirconia was 0.00005667 g/cm^2/hr in the 13000 ppm aqueous solution of the boric acid.

When it comes to thermal conductivity, the product exhibits the thermal conductivity 2-3 times greater than that of zirconia, depending on the product composition. This claim is based on the assessment of thermal conductivity derived from thermal diffusivity measured by laser flash method in the temperature range from 200 to 1200^{o}C, measured density, and calculated heat capacity. Analytical estimates of the anticipated maximum temperature (normal reactor operation) in a hypothetical IMF

rod based on the magnesia-zirconia ceramics yielded the values well below the melting temperature and well below current maximum temperatures authorized in LWRs. This claim is based on the set of calculations conducted for six different ceramic compositions, for the LHGR of 426 W/cm and the fuel pellet surface temperatures in the range of 300-600 ^{o}C.

The product is fabricated by conventional pressing and sintering techniques of the oxide mixture. Product characterization performed using SEM, EDS, and XRD established presence of two major phases: cubic magnesia-zirconia solid solution and cubic magnesia. Erbia doping intended to simulate addition of the burnable poison, resulted in a complete dissolution of erbia in the zirconia-based solid solution without significant rejection of magnesia from the said solid solution. No erbia was detected in the magnesia phase. The dopant behavior in magnesia-zirconia system is exceptionally favorable, because by preferentially dissolving in zirconia phase, the dopant does not contaminate the highly conductive magnesia phase. The latter means that doping has a less pronounced effect on the thermal transport properties of the product.

Finally, a closer look on the microstructure and composition of the product previously exposed to the de-ionized water, helped to understand the mechanism behind the improved hydration resistance and to establish the contrast between pure magnesia ceramics and magnesia-zirconia ceramics. SEM and XRD analyses suggested, that as in the case of pure magnesia, the mass loss of magnesia-zirconia ceramics occurs due to hydration of the magnesia phase. However, presence of zirconia in the system tends to eliminate the hydration-induced cracking typical for pure magnesia ceramics and

responsible for its catastrophic degradation in hydrothermal conditions. With the elimination of cracking, the hydration occurs on the surface of the ceramics, and proceeds in a layer-by layer mode.

REFERENCES

[1] K.E. Sickafus, R.J. Hanrahan, K.J. McClellan, J.N. Mitchell, C.J. Wetteland, D.P. Butt, P. Chodak, K.B. Ramsey, T.H. Blair, K. Chidester, H. Matzke, K. Yasuda, R.A. Verrall, N. Yu, Burn and bury option for plutonium, American Ceramic Society Bulletin 78 (1) (1999) 69-74.

[2] M.D. Freshley, Irradiation behavior of plutonium fuels, in O.J. Wick (Ed.), Plutonium Handbook: A Guide to the Technology, Gordon and Breach, New York, 1967, pp. 643-706.

[3] National Academy of Sciences, Management and Disposition of Excess Weapons Plutonium, National Academy Press, Washington, DC, 1994.

[4] Ch. Hellwig and U. Kasemeyer, Inert matrix fuel performance during the first two irradiation cycles in a test reactor: comparison with modeling results, Journal of Nuclear Materials 319 (2003) 87-94

[5] T. Nakamura, H. Sasajima, T. Yamashita and H. Uetsuka, Morphology change of rock-like oxide fuels in reactivity-initiated-accident simulation tests, Journal of Nuclear Materials 319 (2003) 95-101.

[6] C. Degueldre, J. Paratte, Basic properties of a zirconia-based fuel material for light water reactors, Nuclear Technology 123 (1) (1998) 21-29.

[7] C. Degueldre, T. Arima, Y. W. Lee, Thermal conductivity of zirconia based inert matrix fuel: use and abuse of the formal models for testing new experimental data, Journal of Nuclear Materials 319 (2003) 6-14.

[8] K. Yasuda, C. Kinoshita, S. Matsumura and A. I. Ryazanov, Radiation-induced defect clusters in fully stabilized zirconia irradiated with ions and/or electrons, Journal of Nuclear Materials 319 (2003) 74-80.

[9] U. Kasemeyer, Ch. Hellwig, J. Lebenhaft and R. Chawla, Comparison of various partial light water reactor core loadings with inert matrix and mixed-oxide fuel, Journal of Nuclear Materials 319 (2003) 142-153.

[10] H. Akie, Y. Sugo and R. Okawa, Core burnup calculation and accidents analyses of a pressurized water reactor partially loaded with rock-like oxide fuel, Journal of Nuclear Materials 319 (2003) 166-172.

[11] F.C. Klaassen, K. Bakker, R.P.C. Schram, R. Klein Meulekamp, R. Conrad, J. Somers and R. J.M. Konings, Post irradiation examination of irradiated americium oxide and uranium dioxide in magnesium aluminate spinel, Journal of Nuclear Materials 319 (2003) 108-117.

[12] R.P.C. Schram, R.R. van der Laan, F.C. Klaassen, K. Bakker, T. Yamashita and F. Ingold, The fabrication and irradiation of plutonium-containing inert matrix fuels for the `Once Though Then Out' experiment, Journal of Nuclear Materials 319 (2003) 118-125.

[13] N. Nitani, K. Kuramoto, T. Yamashita, Y. Nihei and Y. Kimura, In-pile irradiation of rock-like oxide fuels, Journal of Nuclear Materials, 319 (2003) 102-107.

[14] E.A.C. Neeft, K. Bakker, R. P. C. Schram, R. Conrad and R. J. M. Konings, The EFTTRA-T3 irradiation experiment on inert matrix fuels, Journal of Nuclear Materials 320 (1-2) (2003) 106-116.

[15] T. Wiss, R. J. M. Konings, C. T. Walker and H. Thiele, Microstructure characterization of irradiated Am-containing MgAl2O4 (EFTTRA-T4), Journal of Nuclear Materials 320 (1-2) (2003) 85-95.

[16] J. Noirot, L. Desgranges, N. Chauvin and V. Georgenthum, Post-irradiation examinations of THERMHET composite fuels for transmutation, Journal of Nuclear Materials 320 (1-2) (2003) 117-125.

[17] Y. Croixmarie, E. Abonneau, A. Fernández, R. J. M. Konings, F. Desmoulière and L. Donnet, Fabrication of transmutation fuels and targets: the ECRIX and CAMIX-COCHIX experience, Journal of Nuclear Materials 320 (1-2) (2003) 11-17.

[18] N. Chauvin, T. Albiol, R. Mazoyer, J. Noirot, D. Lespiaux, J. C. Dumas, C. Weinberg, J. C. Ménard and J. P. Ottaviani, In-pile studies of inert matrices with emphasis on magnesia and magnesium aluminate spinel, Journal of Nuclear Materials 274 (1-2) (1999) 91-97.

[19] S.L. Hayes, M.K. Meyer, D.C. Crawford, G.S. Chang, F.W. Ingram, Irradiation testing of actinide transmutation fuels in the advanced test reactor, Proceedings of the ANS Topical Meeting on Accelerator Applications/Accelerator Driven Transmutation Technology Applications '01, November 11-15, 2001, Reno, NV.

[20] T.G. Langdon and J.A. Pask, Mechanical behavior of single-crystal and polycristalline MgO, in A.M. Alper, (Ed.), High Temperature Oxides Part III, Academic Press, New York, 1970.

[21] R.E. Kirk, D.F. Othmer, J.I. Kroschwitz, M. Howe-Grant, Encyclopedia of Chemical Technology, Wiley, New York, 1997.

[22] S.J. Boles, Uses and Properties of Magnesia as a Superrefractory for Temperatures above 1500 ^{o}C.: A Bibliography, U.S. Dept of the Interior, Bureau of Mines, Washington, DC, 1962.

[23] A.C. Victor and T.B. Douglas, Thermodynamic properties of magnesium oxide and beryllium oxide from 298 to 1200 K, Journal of Research of the National Bureau of Standards 67A (4) (1963) 325-329.

[24] M. Miyayama, K., Koumoto and H.Yanagida, Engineering properties of single oxides, in: S.J. Schneider, Jr (Ed.), Engineered Materials Handbook 4, ASM International, 1991, pp. 748-757.

[25] M.E. Schlesinger, Melting points, crystallographic transformation, and thermodynamic values, in S.J. Schneider, Jr (Ed.), Engineered Materials Handbook 4, ASM International, 1991, pp. 883-891

[26] S.G. Popov, J.J. Carbajo, V.K. Ivanov, G.L. Yoder, Thermophysical Properties of MOX and UO_2 Fuels Including the Effects of Irradiation, Oak Ridge National Laboratory report ORNL/TM-2000/351, Oak Ridge, TN, 2000.

[27] M. McQuarrie, Thermal conductivity: V. high temperature method and results for alumina, magnesia, and beryllia from 1000 to 1800 C, Journal of the American Ceramic Society 37 (1954) 84-88.

[28] F.R. Charvat, W.D. Kingery, Thermal conductivity XIII: Effect of microstructure on conductivity of single-phase ceramics, Journal of the American Ceramic Society 40 (1957) 306-315.

[29] M. Neuberger, D.B. Carter, Magnesium oxide; Hughes Aircraft Co., Electronic Properties Information Center, Culver City, CA, 1969.

[30] A.J. Slifka, B.J. Filla, and J.M. Phelps, Thermal conductivity of magnesium oxide from absolute, steady-state measurements, Journal of Research of the National Institute of Standards and Technology 103 (4) (1998) 357-363.

[31] C.E. Beyer, D.D. Lanning, C.L. Painter, FRAPCON-3: Modifications to Fuel Rod Material Properties and Performance Models for High-Burnup Application, Nuclear Regulatory Commission, Washington, DC, 1997, p. 3.8.

[32] G. K. White and O.L. Anderson, Gruneisen parameter of magnesium oxide, Journal of Applied Physics 37 (1) (1966) 430-432.

[33] I. Suzuki, Thermal expansion of periclase and olivine, and their anharmonic properties, Journal of Physics of the Earth 23 (1975) 145-159.

[34] M. Miyayama, K. Koumoto, H. Yanagida, Engineering properties of single oxides, in: S.J. Schneider, Jr (Ed.), Engineered Materials Handbook 4, ASM International, 1991, pp. 748-757.

[35] R.R. Reeber, K. Goessel, K. Wang, Thermal expansion and molar volume of MgO, periclase, from 5 K to 2900 K, European Journal of Mineralogy 7 (1995) 1039-1047.

[36] J.B. Wachtman Jr., D.G. Lam Jr., Young's modulus of various refractory materials as a function of temperature, Journal of the American Ceramic Society 42 (5) (1959) 254-260.

[37] N. Soga and O.L. Anderson, High-temperature elastic properties of polycrystalline MgO and Al_2O_3, Journal of the American Ceramic Society 49 (7) (1996) 355-359.

[38] O. L. Anderson, D.L. Isaak, H. Oda, Thermoelastic parameters for six minerals at high temperature, Journal of geophysical research 96 (B11) (1991) 18.037-18.046.

[39] A. Nishida, T. Shimamura, Y. Kohtoku, Effect of grain size on mechanical properties of high-purity polycrystalline magnesia, Journal of the Ceramic Society of Japan 98 (4) (1990) 412-415.

[40] J.H. Rust, Nuclear Power Plant Engineering, Haralson, Buchanan, GA, 1979.

[41] W.D Kingery, Effect of low temperature neutron irradiation and 20 to 400^{o}C annealing on the density and lattice parameters of aluminum oxide and magnesium oxide, Journal of Nuclear Materials 24 (1967) 21-33.

[42] B.Wilshire, Creep mechanisms in single and polycrystalline MgO, British Ceramic Transactions 94 (2) (1995) 57-63.

[43] R.W. Evans, P.J. Scharning, B. Wilshire, Creep of basic refractory oxides, in: Wilshire, B.; Evans, R. W., (Eds.), Creep Behavior of Crystalline Solids, Pineridge Press Limited, Swansea, UK, 1985.

[44] A.G. Evans, D. Gilling, R.W. Davidge, Temperature-dependence of the strength of polycrystalline MgO, Journal of Materials Science 5 (3) (1970) 187-197.

[45] A.G. Evans, R.W. Davidge, The strength and fracture of stoichiometric polycrystalline UO2, Journal of Nuclear Materials 33 (1969) 249-60.

[46] W. D. Callister, Materials Science and Engineering: an Introduction, Wiley, New York, 1991.

[47] M.D. Freshley, D.F. Carroll, The irradiation performance of MgO/PuO_2 fuel material, Transactions of the American Nuclear Society 6 (1963) 396-397.

[48] D.T. Livey, P.Murray, The stability of berillia and magnesia in different atmospheres at high temperatures, Journal of Nuclear Energy 2 (1956) 202-212.

[49] G.W. Groves, A. Kelly, Neutron Damage in MgO, Philosophical Magazine 8 (1963) 1437-1454.

[50] R.A.J. Sambell, R. Bradley, The strength of irradiated magnesium oxide, Philosophical Magazine 8 (1964) 161-166.

[51] D.H. Bowen, F.J.P. Clarke, The growth of neutron irradiated magnesium oxide; Philosophical Magazine 8 (1) (1964) 413-421.

[52] J.A. Desport, J.A.G. Smith, Irradiation-induced growth in oxides of beryllium, magnesium and aluminum, Journal of Nuclear Materials 14 (1964) 135-140.

[53] D.G. Walker, B.S. Hickman, X-ray line broadening in neutron irradiated magnesium oxide, Philosophical Magazine 8 (12) (1965) 445-451.

[54] B.S. Hickman, D.G. Walker, Growth of magnesium oxide during neutron irradiation; Philosophical Magazine 8 (11) (1965) 1101-1108.

[55] M. Stevanovic, J. Elston, Effect of fast neutron irradiation in sintered alumina and magnesia, Proceedings of the British Ceramic Society 7 (1967) 423-437.

[56] W.D. Kingery, Effect of low temperature neutron irradiation and 20 to 400°C annealing on the density and lattice parameters of aluminum oxide and magnesium oxide, Journal of Nuclear Materials 24 (1967) 21-33.

[57] C.S. Morgan, D.H. Bowen, Inert gas bubbles in neutron irradiated magnesium oxide; Philosophical Magazine 16 (1967) 165-180.

[58] R.W. Davidge, Irradiation damage and irradiation hardening in single crystal MgO after Low Neutron Doses < 1018 NVT (> 1 MeV), Journal of Nuclear Materials 25 (1968) 75-86.

[59] B. Henderson, D.H. Bowen, Radiation damage in magnesium oxide. I. Dose dependence of reactor damage, Journal of Physics C: Solid State Physics 4 (12) (1971) 1487-1495.

[60] C.J. Howard, T.M. Sabine, X-ray diffraction profiles from neutron-irradiated magnesium oxide, Journal of Physics C: Solid State Physics 7 (19) (1974) 3453-3466.

[61] F.W. Clinard Jr., G. F. Hurley, L.W. Hobbs, Neutron irradiation damage in MgO, Al_2O_3 and $MgAlO_4$ Ceramics, Journal of Nuclear Materials 108-109 (1981) 655-670.

[62] R.P.C. Schram, R.J.M. Bakker, J.G. Boshoven, G. Dassel, H. Hein, R.R. van der Laan, E.A.C. Neeft, R. Konings, K.Conrad, Irradiation experiments and fabrication technology of inert matrix fuels for the transmutation of actinides, Proceedings of the International Conference on Future Nuclear Systems, Global 99, August 29 - September 3, 1999.

[63] D. Caceres, I. Vergara, R. Gonzalez, Y. Chen, Nanoindentation on neutron irradiated MgO crystals, Nuclear Instruments and Methods in Physics Research, Section B: Beam Interactions with Materials and Atoms 191 (2002) 178-180.

[64] R.S. Wilks, Gas formation by transmutation of MgO and Al_2O_3, Journal of Nuclear Materials 19 (1966) 351-353.

[65] J.J. Duderstadt, L.J. Hamilton, Nuclear Reactor Analysis, Wiley, New York, 1976.

[66] R.S. Wilks, Neutron-induced damage in BeO, Al_2O_3, and MgO: a review, Journal of Nuclear Materials 26 (1968) 137-73.

[67] T.S. Elleman, R.B. Price, D.N. Sunderman, Fission fragment induced expansion in ceramic materials, Journal of Nuclear Materials 15 (1965) 164-178.

[68] M. Beauvy, T. Duverneix, C. Berlanga, R. Mazoyer, C. Duriez, Actinide transmutation: new investigation on some actinide compounds, Journal of Alloys and Compounds 271 (1998) 557-562.

[69] A. Perez, M. Treilleux, L. Fritsch, G. Marest, Spinel ferrite formation in iron implanted MgO, Nuclear Instruments and Methods 182/183 (1981) 747-751.

[70] P.J. Burnett, T.F. Page, Changing of the implantation behavior of MgO by ion implantation, Materials Research Society Symposia Proceedings 27 (1984), Ion Implantation and Ion Beam Processing of Materials, Symposium., Boston, MA, p. 401-406.

[71] P.J. Burnett, T.F. Page, Chemomechanical effect in ion-implanted magnesium oxide, Journal of Materials Science Letters 4 (11) (1985) 1364-1370.

[72] L.L. Horton, J. Bentley, M.B. Lewis, Radiation damage in ion-irradiated MgO, Nuclear Instruments & Methods in Physics Research, Section B: Beam Interactions with Materials and Atoms B16 (2-3) (1986) 221-229.

[73] Y. Aoki, D.M. Ruck, D. Vogt, K. Leible, I. Khubeis, and O. Meyer, Vickers hardness measurement of ion implanted MgO, Nuclear Instruments and Methods in Physics Research B 91 (1994) 247-251.

[74] S.J. Zinkle, Microstructure of ion irradiated ceramic insulators, Nuclear Instruments and Methods in Physics Research B 91 (1994) 234-246.

[75] S.J. Zinkle, L.L. Snead, Influence of irradiation spectrum and implanted ions on the amorphization of ceramics, Nuclear Instruments & Methods in Physics Research, Section B: Beam Interactions with Materials and Atoms 116 (1-4) (1996) 92-101.

[76] T. Sonoda, H. Abe, C. Kinoshita, H. Naramoto, Formation and growth process of defect clusters in magnesia under ion irradiation, Nuclear Instruments and Methods in Physics Research, Section B: Beam Interactions with Materials and Atoms 127 (1997) 176-180.

[77] C. Noguera, Physics and Chemistry at Oxide Surfaces, Cambridge University Press, Cambridge, 1996.

[78] D. Abriou, J. Jupille, Self-inhibition of water dissociation on magnesium oxide surfaces, Surface Science 430 (1) (1999) L527-L532.

[79] D.N. Sah, K.C. Sahoo, S. Chatterjee, S. Majumdar, H.S. Kamath, R. Ramachandran, J.K. Bahl, D.S.C. Purushottam, M.S. Ramakumar, K.S., Sivaramakrishnan, Fabrication and Post-Irradiation Examination of a Zircaloy-2 Clad UO2-1.5 wt% PuO_2 fuel pin Irradiated in PWL, CIRUS, Report Number: BARC-918, Bhabha Atomic Research Centre, Bombay (India), 1977.

[80] I.S. Kurina, A.M. Dvoryashin, L.S. Gudkov, Production and investigation of thorium-containing fuel compositions, Atomic Energy 88 (5) (2000) 362-367.

[81] V. Monastra, D.E. Grandstaff, Kinetics of MgO dissolution and buffering of fluids in the Waste Isolation Pilot Plant (WIPP) repository; Materials Research Society Symposium – Proceedings 556 (1999), Proceedings of the 1998 MRS Fall Meeting - Symposium 'Scientific Basis for Nuclear Waste Management XXII, Nov 30-Dec 4 1998, Boston, MA, 625-632.

[82] G. Economos, Behavior of refractory oxides in contact with metals at high temperatures, Industrial and Engineering Chemistry 45 (1953) 458-459.

[83] E.Tolksdorf, Corrosion behavior of new Zr alloys; Journal of Nuclear Materials 51 (3) (1974) 330-336.

[84] H. Zhang, R.J.M. Konings, M.E. Huntelaar, E.H.P Cordfunke, Melting behaviour of oxide systems for heterogeneous transmutation of actinides. III. The system Am-Mg-O; Journal of Nuclear Materials 250 (2-3) (1997) 88-95.

[85] H. Zhang, M.E. Huntelaar, R.J.M. Konings, E.H.P. Cordfunke, Melting behaviour of oxide systems for heterogeneous transmutation of actinides. I. The systems Pu-Al-O and Pu-Mg-O; Journal of Nuclear Materials 249 (2-3) (1997) 223-230.

[86] A. Hough, J.A.C. Marples, The pseudo binary phase diagrams of PuO_2 with alumina, berillia and magnesia and the pseudo ternary PuO_2-BeO-O; Journal of Nuclear Materials 15 (1965) 298-309.

[87] J.S. Anderson, K.D.B. Johnson, The oxides of uranium. Part III. The system UO_2-MgO-O, Journal of the Chemical Society (1953) 1731-1737

[88] W.A. Lambertson, M.H. Mueller, Uranium oxide phase equilibrium systems: II. UO_2-MgO, Journal of the American Ceramic Society 36 (1953) 329-331.

[89] S.M. Lang, F.P. Knudsen, C.L. Fillmore, R.S. Roth, High-Temperature Reactions of Uranium Dioxide with Various Metal Oxides, National Bureau of Standards circular 568, U.S. Government Printing Office, Washington, DC, 1956.

[90] P.P. Budnikov, S.G. Tresvyatsky, V.I. Kushakovsky, Binary phase diagrams UO2-Al_2O_3, UO_2-BeO and UO_2-MgO, Proceedings of the International Conference on the Peaceful Uses of Atomic Energy, Geneva (Switzerland) 1958.

[91] D.F. Carroll, The system PuO_2-MgO, Journal of the American Ceramic Society, 47 (1964) 650.

[92] S. Casalta, K. Ritcher, C. Prunier, A study of AmO_2-MgO system for americium target transmutation in fast reactors; Proceedings of the ANS International Conference on Evaluation of Emerging Nuclear Fuel Cycle Systems, 11-14 Sep 1995, Versailles (France) 1995.

[93] I.S. Kurina, L.I. Moseev, Fabrication and study of the properties of PuO_2-MgO fuel pellets, Atomic Energy 82 (5) (1997) 347-350.

[94] A. N. Holden, Dispersion Fuel Elements, U.S. Atomic Energy Commission, American Society for Metals, Gordon and Breach, New York, 1968.

[95] R.A Verrall, M.D. Vlajic, V.D. Krstic, Silicon carbide as an inert-matrix for a thermal reactor fuel, Journal of Nuclear Materials, 274 (1-2) (1999) 54-60.

[96] D.D. Lanning, C.E. Beyer, G.A. Berna, FRAPCON-3: Integral Assessment, U.S. Nuclear Regulatory Commission, Washington, DC, 1997, p. A3.15.

[97] A. Kitamura, K. Onizuka, K. Tanaka, Hydration characteristics of magnesia, Taikabutsu Overseas 16 (3) (1996) 3-11.

[98] J.W. Nelson, I.B. Cutler, Effect of oxide additives on sintering of magnesia, Journal of American Ceramic Society 41 (10) (1958) 406-409.

[99] T.C. Yuan, G.V. Srinivasan, J.F. Jue, A.V. Virkar, Dual-phase magnesia-zirconia ceramics with strength retention at elevated temperatures, Journal of Materials Science 24 (11) (1989) 3855-3864.

[100] D.J. Kim, Lattice parameters, ionic conductivities, and solubility limits in fluorite-structure MO2 oxide (M = Hf4+,Zr4+,Ce4+,Th4+,U4+) solid solutions, Journal of the American Ceramic Society 72 (8) (1989) 1415-1421.

[101] R. D. Shannon, Revised effective ionic radii and systematic studies of interatomic distances in halides and chalcogenides; Acta Crystallographica Section A: Foundations of Crystallography A32 (1976) 751-767.

[102] S. Soo Man, V. Stubican, Phase relations and ordering in the system ZrO2-MgO, Journal of the American Ceramic Society 70 (7) (1987) 521-526.

[103] J. Saiki, K. Hirota, O. Yamaguchi, S. Inamura, H. Miyamoto, N. Shiokawa, K. Tsuji, Formation, transformation and sintering of ZrO2-MgO compositions prepared from alkoxides, British Ceramic Transactions 92 (4) (1993) 161-164.

[104] Y. Yin, B.B. Argent, Phase diagrams and thermodynamics of the systems ZrO2-CaO and ZrO2-MgO, Journal of Phase Equilibria 14 (4) (1993) 439-450.

[105] Powder diffraction file, JCPDS--International Centre for Diffraction Data, CD-ROM, Newtown Square, PA, 1993-present.

[106] R.K. Stewart, O. Hunter Jr., Stabilization of Zirconia by Erbia; Journal of the American Ceramic Society 53 7 (1970) 421-422.

[107] C.C. Lin, Radiochemistry in Nuclear Power Reactors, National Academy Press, Washington, DC, 1996.

[108] Standard Test Method for Thermal Diffusivity of Solids by the Flash Method, ASTM, E1461-01, West Conshohocken, PA, 2003.

[109] C. Ronchi, J. P. Ottaviani, C. Degueldre, R. Calabrese, Thermophysical properties of inert matrix fuels for actinide transmutation, Journal of Nuclear Materials 320 (1-2) (2003) 54-65.

[110] J. P. Ottaviani, Plutonium and Minor Actinides-Based Oxide Fuels Handbook, Note Technique LMPC n 2004-047, CEA, Cadarache (France), 2004.

[111] D.Sh. Tsagareishvili, G.G. Gvelesiani, High-temperature enthalpy and specific heat of erbium sesquioxide, High Temperature 9 (3) 1971 588-559.

[112] S. Kakaç, Y. Yener, Heat Conduction, Hemisphere, Washington, DC, 1985, p.78.

VITA

Mr. Pavel Medvedev received a Master of Science degree in nuclear science and engineering from Idaho State University in 1997, and a Doctor of Philosophy degree in nuclear engineering from Texas A&M University in 2004. His research interests include development of advanced nuclear fuels and nuclear fuel performance modeling. He can be reached at Argonne National Laboratory, Nuclear Technology Division, Idaho Falls, ID 83403-2528.